Title

A Tandem Active Site Model for the Ribosomal Helicase

Author

Amiri, Mohammad Hossein

Publication Date

2017

UNIVERSITY OF CALIFORNIA
SANTA CRUZ

A TANDEM ACTIVE SITE MODEL FOR THE RIBOSOMAL HELICASE

A dissertation submitted in partial satisfaction
of the requirements for the degree of

DOCTOR OF PHILOSOPHY

in

MOLECULAR, CELL AND DEVELOPMENTAL BIOLOGY

by

Mohammad Hossein Amiri

September 2017

The Dissertation of Mohammad Hossein Amiri is approved:

Professor Harry F. Noller, Chair

Professor Manuel Ares

Professor William G. Scott

Tyrus Miller
Vice Provost and Dean of Graduate Studies

Table of Contents

List of Figures

List of Tables

Abstract

A Tandem Active Site Model for the Ribosomal Helicase

Mohammad Hossein Amiri

The ribosome is an mRNA helicase, actively unwinding encountered structures in the mRNA during translation, so that codons can be read in single-stranded form. Our understanding of the ribosomal helicase has advanced in recent years thanks to a combination of structural and functional approaches. However, the molecular mechanisms of mRNA unwinding by this helicase are still poorly understood. Here, I present the crystal structure of the *Escherichia coli* 70S ribosome in complex with a hairpin-containing mRNA and A- and P-site tRNAs at 3.9Å resolution. Although the hairpin is disordered in the structure, its presence in the mRNA induces large-scale crystal packing rearrangements. Crystal contacts made by ribosomal protein S3 located near the mRNA tunnel entrance are eliminated, and those made by ribosomal protein L9 are significantly changed. The mRNA itself is relocated from its expected position to allow three nucleotides upstream of the hairpin to interact with protein S3 just outside of the tunnel entrance. In vitro assays on reconstituted ribosomes show that the mutation of S3 residues near the tunnel entrance significantly affect mRNA-dependent tRNA binding, consistent with mRNA binding to protein S3. Based on these observations, a tandem active site model for the ribosomal helicase is proposed, in which the proximal active site is at the tunnel entrance, and the distal active site is three nucleotides further downstream. The single-stranded mRNA between the two active sites binds to protein S3 outside of the tunnel. Translocation over mRNA structures at the distal active site occurs during reverse 30S head rotation, and proceeds via two routes in a stick-slip manner: (1) mRNA unwinding and sliding along the S3 binding interface, or (2) disruption of the S3-mRNA binding without unwinding, allowing bypass to the proximal active site. Unwinding of structures that reach the proximal active site is favored by equilibrium binding of the single-stranded product to protein S3. The kinetic scheme for the tandem active site model accounts for a number of previously unexplained experimental observations, and makes testable quantitative predictions to further study unwinding by the ribosome and other helicases.

Acknowledgments

I am grateful to my graduate advisor, Harry Noller, for his guidance and support, and for always leading by example.

I thank current and past members of the Noller laboratory, particularly Laura Lancaster for her patient and thorough mentorship, John Paul Donohue for his expert computer support, Jianyu Zhu for getting me started in the lab, and Shervin Takyar for providing critical feedback.

I also thank my thesis committee members Manuel Ares and William Scott for advice and encouragement, Teel Lopez for unmatched administrative support, David States for help in writing my thesis proposal, and Doug Kellogg, Grant Hartzog, Susan Carpenter, Carrie Partch, Melissa Jurica, Benjamin Abrams, and Clive Bagshaw for expert technical advice.

Preface: Unzipping RNA by Stick-Slip

In this dissertation, I focus on how a translating ribosome encounters new parts of mRNA during protein synthesis, and how it deals with potential roadblocks. As the mRNA chain is threaded into a small tunnel through the ribosome, one can imagine the possibility of a "jamming" mishap at the tunnel entrance because mRNA can fold by itself or tangle in complex with other molecules. mRNA is particularly prone to folding because it is only composed of four types of building blocks –abbreviated A, U, G, and C– where A tends to pair with U, and G with C, which, along with other less-defined pairing rules, allow the formation of folded structures such as hairpins and pseudoknots.

It can be safely assumed that billions of years of evolution by natural selection has perfected the ability of the cell to overcome unwanted mRNA roadblocks in a most frugal way. The task has been given, apparently in no small part, to the ribosome itself, which couples its intricate mechanical gear to an ancillary "helicase" function localized at the entrance of the mRNA tunnel. Part of the job of the helicase is simply guarding the gates by only allowing unfolded mRNA into the tunnel; but evidently, this has not been sufficient. The helicase also ensures that the speed of translation does not greatly suffer from the arrival of folded mRNA segments at the tunnel entrance, actively working to reduce the chance of these roadblocks even reaching the entrance in the first place. The structure of the tunnel entrance is known, as is the approximate location along the mRNA where the helicase operates. However, the detailed mechanism of unwinding is still a mystery.

To better understand the unwinding mechanism, I attempted to determine, using X-ray crystallography, the structure of a translating ribosome encountering a hairpin at the tunnel entrance, with the hope that the way the ribosome interacts with the hairpin would give us clues on how it proceeds to unwind the hairpin. I found that the ribosome does not bind the hairpin in the vicinity of the tunnel entrance, but rather interacts with the single-stranded mRNA that precedes the hairpin. This may appear to be a trivial observation, but it immediately suggests that the ribosome has not one, but at least two helicase active sites. An mRNA roadblock meets the “distal” active site first, reaching the tunnel entrance (the “proximal” active site) only if the distal site fails at unwinding it.

This realization allowed for the quantitative modeling of the unwinding activity of the ribosomal helicase in terms of thermodynamic and kinetic constants, and gave further insight into how the helicase may operate. It showed that nothing more than the spontaneous thermal “breathing” of the mRNA roadblock at either of the two active sites is needed to account for its unwinding. It also showed that the ribosome has apparently taken advantage of its slow overall stepping rate to maximize helicase efficiency. Finally, the study of the ribosomal helicase may have uncovered a widespread strategy of nucleic acid unwinding by stick-slip, the universal friction phenomenon of non-uniform relative motion between two interacting surfaces (in this case between the helicase and its bound nucleic acid), in which the surfaces frequently stick together and then slip, rather than sliding smoothly.

In Chapter 1, I review ribosome structure and function with emphasis on aspects that are relevant to its helicase activity. In Chapter 2, the results of my structural and functional analyses on the ribosomal helicase are presented. Chapter 3 describes the quantitative tandem active site model for the ribosomal helicase.

Chapter 1. The Ribosome as an mRNA Helicase

1.1. Overview

The ribosome is a large molecular machine that carries out protein synthesis in all cells. In the elongation phase of this translation process, the ribosome moves along an mRNA in the 5'-to-3' direction. Consecutive codons on the mRNA enter the mRNA tunnel inside the ribosome through an entrance in the small subunit that is lined by ribosomal proteins S3, S4, and S5, and follow a curved path around the neck of the subunit. Following each cycle of tRNA selection and peptide bond formation, translocation of tRNA and mRNA occurs by the coordinated movement of these molecules through intermediate stages including the classical, hybrid, and chimeric hybrid states. This is accompanied by ribosomal intersubunit rotation, as well as intra-subunit conformational changes including a rotation of the head domain of the small subunit. Encountered mRNA structures in the ribosome are unwound by an intrinsic mRNA helicase activity that is coupled to translocation and is localized to the vicinity of the tunnel entrance. The helicase unwinds secondary structures actively, and its unique kinetic behavior cannot be explained by a single unwinding mechanism, setting the ribosome apart from all other known helicases.

1.2. mRNA Translation

1.2.1. Translation connects the genotype to the phenotype

The central dogma of molecular biology (Crick, 1970) describes the flow of genetic information in all cells. Information can be "transcribed" from DNA to RNA, and “translated” from RNA to protein. Translation is a fitting name, as this process entails a change in language, from a string of nucleotides to that of amino acids (Gamow, 1954). Unsurprisingly, translation is a much more complex process than transcription. Whereas transcription can be performed by a single-subunit enzyme of less than 100 kDa in mass, translation in all organisms is carried out by the ribosome which is at least ~ 2 MDa, is assembled from tens of individual molecules, and is assisted by a crew of factors and adaptors.

A single bacterial cell may contain tens of thousands of ribosomes, while an animal cell may contain millions, synthesizing proteins which in turn go on to carry out multitudes of functions in the cell. Ribosomes can take up a significant fraction of a growing cell’s dry mass, up to more than one third, and consume a sizable portion of the cell’s energy budget (Duncan and Hershey, 1983; Kafri et al., 2016; Milo and Phillips, 2016; Warner, 1999). Attacking this crucial apparatus and protecting it from attacks have been common tactics in the natural warfare between species, giving us the gift of antibiotics against deadly infections (and the curse of antibiotic resistance) (Wilson, 2014).

1.2.2. mRNA binds the small ribosomal subunit to initiate translation

Protein synthesis on the ribosome involves initiation, elongation, termination, and recycling stages. Protein synthesis begins with the recruitment of mRNA and initiator tRNA (fMet-tRNA$^{\mathrm{fMet}}$) to the small ribosomal subunit, followed by the formation of the initiation complex once the large subunit joins them (Laursen et al., 2005). Most bacterial mRNAs are polycistronic (Kozak, 1983), and translation initiation for each open reading frame occurs by base-pairing of an upstream Shine-Dalgarno (SD) motif in the mRNA to the 3' terminal segment of 16S ribosomal RNA (Shine and Dalgarno, 1974), although translation can start *in vitro* on mRNAs lacking an SD sequence or even a start codon (Nirenberg and Matthaei, 1961). Efficient initiation inside the cell is further enhanced by the binding of initiation factors IF1, IF2, and IF3, and by GTP hydrolysis by IF2 (Gualerzi et al., 2001; Laursen et al., 2005). Translation initiation in eukaryotes is typically much more complex, and involves the recognition of the 5' mRNA cap and the subsequent 5'-3' scanning of the mRNA by the pre-initiation complex, during which the helicase activity of the eukaryotic initiation factor eIF4A, a model DEAD-box-family helicase, helps unwind mRNA secondary structures in the 5' untranslated region preceding the start codon (Andreou and Klostermeier, 2013; Jackson et al., 2010).

1.2.3. mRNA codon choice affects the rate of translation elongation

Following translation initiation, which positions the initiator tRNA and the start codon in the P site of the ribosome, elongation can commence. It proceeds in cycles, at a rate of ~20 cycles (codons) per second in bacteria or ~6 in eukaryotes (Milo and Phillips, 2016). An elongation cycle includes tRNA selection and accommodation, peptide bond formation, and tRNA/mRNA translocation. A new aminoacyl-tRNA enters the A site, attacks the C-terminal end of the growing peptide, and moves into the P site, while the old now-deacylated P-site tRNA exits the ribosome through the E site. Bacterial elongation factors EF-Tu and EF-G catalyze distinct steps within the cycle, hydrolyzing their bound GTP in the process (Maracci and Rodnina, 2016). EF-Tu, a highly abundant protein, forms a ternary complex with an aminoacyl-tRNA and a molecule of GTP, and is responsible for delivering tRNAs to the ribosome to select the A-site codon. While its acceptor end is bound to EF-Tu outside of the A site, the anticodon end of the tRNA reaches the mRNA codon in the decoding center of the small ribosomal subunit. In the case of a cognate tRNA, correct codon-anticodon base-pairing is sensed via formation of A-minor interactions involving the highly conserved G530, A1492, and A1493 bases in helix h44 of 16S rRNA (Moazed and Noller, 1989a, 1990; Ogle et al., 2002). This is communicated to EF-Tu through the GTPase-associated center of the large ribosomal subunit (Fagan et al., 2013; Schuette et al., 2009). GTP hydrolysis then releases EF-Tu from the ribosome, and tRNA is accommodated in the A site after an additional fidelity check by kinetic proofreading (Hopfield, 1974). The tRNA now adopts a relaxed conformation that fits in the A site in both subunits. Its CCA end interacts with the "A-loop" in helix H92 of the 23S rRNA, placing the terminal aminoacyl moiety in the highly conserved peptidyl transfer center of the large subunit, made entirely of elements from the 23S rRNA. Peptide bond formation follows rapidly at this point simply due to the optimal placement of the aminoacyl moiety relative to the 3'-end ester of the neighboring P-site tRNA (Sievers et al., 2004), which is held in place by interaction of its CCA end with the "P-loop" in helix H80 of 23S rRNA. Accommodation of the (correct) A-site tRNA during elongation poses a challenge to translational fidelity and speed, which appear to be in a fine balance (Wohlgemuth et al., 2011). The rate of translation elongation can be significantly reduced by rare tRNAs, and so the codon choice in the mRNA sequence has a major impact on translation rates (Gorochowski et al., 2015; Sørensen et al., 1989; Wohlgemuth et al., 2013).

1.2.4. The ribosome steps along the mRNA during translation elongation

Peptide bond formation is followed by the spontaneous formation of tRNA hybrid states. A hybrid-state tRNA occupies the A (or P) site on the 30S subunit, but the P (or E) site on the 50S subunit (Moazed and Noller, 1989b) as a result of intersubunit rotation (Frank and Agrawal, 2000). After hybrid states formation, translocation of tRNAs with respect to the small subunit takes place, concomitant with mRNA translocation (Ermolenko and Noller, 2011). This is catalyzed by EF-G, which binds to the ribosome with high affinity when GTP-bound and stabilizes the hybrid state (Chen et al., 2013; Spiegel et al., 2007). EF-G binding also induces the rotation of the head domain of the small subunit and the formation of chimeric hybrid tRNA states (Guo and Noller, 2012; Ramrath et al., 2013; Ratje et al., 2010; Zhou et al., 2014). In this state, the tRNA is in the A (or P) site of the head domain, but the P (or E) site of the body domain, and the mRNA has moved along with the head. The head rotation also widens the path of the tRNA between the P and E sites on the small subunit (Schuwirth et al., 2005). GTP hydrolysis by EF-G is stimulated by binding to the GTPase-associated center in the large subunit and precedes tRNA translocation

(Savelsbergh et al., 2003), suggesting that it may provide the free energy for the subsequent events in translocation. However, EF-G can catalyze at least one cycle of translocation in the presence of a nonhydrolyzable GTP analog or fusidic acid (Ermolenko and Noller, 2011; Inoue-Yokosawa et al., 1974), suggesting that neither GTP hydrolysis nor EF-G release from the ribosome is absolutely required for translocation. Domain IV of EF-G is seen in chimeric hybrid and post-translocation complexes to approach and dock in the A site of the small subunit (Valle et al., 2003; Zhou et al., 2014), and can therefore sterically block reverse tRNA movement. Furthermore, it has been suggested that this domain may facilitate translocation earlier by disrupting ribosome interactions with the A-site tRNA at the decoding center (Liu et al., 2014a; Savelsbergh et al., 2003).

mRNA translocation with respect to the small subunit is correlated with reverse head movement, which occurs at roughly the same rate as intersubunit rotation back to the classical state (Guo and Noller, 2012). The mRNA may be following tRNA movement mostly passively during translocation, because mRNA cannot translocate without P-site and (at least the anticodon stem-loop of) the A-site tRNA, whereas tRNAs with no mRNA can translocate (Belitsina et al., 1981; Joseph and Noller, 1998). Further supporting this notion, tRNAs that form four base pairs with mRNA can shift the reading frame by translocating the mRNA by four nucleotides (Phelps et al., 2006; Riddle and Carbon, 1973).

1.2.5. mRNA is not immediately released after translation termination

When a stop codon in the mRNA reaches the A site, it is bound by a class I release factor (RF1 or RF2), which recognizes the codon bases via a conserved amino acid sequence motif. The factor then reaches into the peptidyl transfer center and catalyses the hydrolysis of the peptidyl-tRNA by another conserved motif, thus releasing the polypeptide chain (Laurberg et al., 2008). Finally, binding of the class II release factor RF3 to the ribosome and its GTP hydrolysis releases RF1 or RF2 from the terminated ribosome (Freistroffer et al., 1997).

The post-termination ribosome, however, still remains bound to mRNA and tRNA, and must be recycled in order to carry out a new round of protein synthesis. The ribosome recycling factor (RRF) binds to the A site of this ribosome (Agrawal et al., 2004; Hirokawa et al., 2002). The subsequent dissociation of the ribosomal subunits is induced by GTP hydrolysis by EF-G, and is stabilized by binding of IF3 to the small subunit (Peske et al., 2005).

1.3. Ribosome Structure

1.3.1. The ribosome has an RNA core

The ribosome, as the name implies (Roberts, 1958), is a ribonucleoprotein complex, made of RNA and protein in comparable amounts. It is a relic from the RNA World (Gilbert, 1986; Noller, 2012; Woese, 1967), and its core functions in protein synthesis are still performed by its RNA components and not its proteins (Cech, 2000; Noller, 2017). The sequence and secondary structure signature of ribosomal RNA is so conserved that one can classify *all* known cellular genomes based on it (Woese et al., 1990). Ribosomal proteins are also highly conserved, despite their secondary role to ribosomal RNA, and many moonlight in other biological processes (Wool, 1996; Wool et al., 1995).

The secondary structures of the ribosomal RNAs were accurately determined with little available direct structural data (Fox and Woese, 1975; Noller and Woese, 1981; Noller et al., 1981), long before they were confirmed by crystallographic studies (Ban et al., 2000; Wimberly et al., 2000). This was accomplished using a clever phylogenetic approach that identified tens of individual conserved stem-loop and even tertiary arrangements in each RNA. The 16S, 23S, and 5S rRNAs from *E. coli*, for example, are organized into 45, 101, and 3 helices, respectively. The 23S rRNA has six major tightly-packed domains, while the 16S rRNA has four, one of which forms the head domain of the small subunit.

1.3.2. The ribosome is composed of multiple components

From tiny dark granules in electron micrographs (Claude, 1943) to near-atomic-resolution crystallographic models (Noeske et al., 2015), our view of ribosome structure has become sharper over time. As of June 2017, there are 467 experimentally-determined structures of the ribosome or its subunits deposited in the protein data bank (PDB), up from only one structure at the turn of the century. These represent ribosomes from all three domains of life, trapped in different states and in complex with a variety of ligands including a large library of medically important antibiotics. Two-thirds of ribosome structures have been determined by X-ray crystallography. Cryo-electron microscopy (cryo-EM) accounts for the other third and can now reach near-atomic resolution thanks to recent advances in instrumentation and data analysis (Binshtein and Ohi, 2015).

A typical bacterial ribosome is composed of a large (50S) and a small (30S) subunit, together sedimenting at 70S. Ribosomes from *Escherichia coli* contain a 23S and a 5S rRNA plus 34 ribosomal proteins in the large subunit, and a 16S rRNA plus 21 proteins in the small subunit, with a combined mass of ~2.3 MDa. The ribosome contains three sites for binding of tRNA molecules, named the acceptor (A), peptidyl (P), and exit (E) sites, for binding to aminoacyl, peptidyl, and deacylated tRNAs, respectively. Eukaryotic cytoplasmic ribosomes have the same architecture, but are larger, in part reflecting the higher regulatory burden in these organisms. For instance, the human ribosome contains 4 rRNAs and 80 r-proteins (Wilson and Doudna Cate, 2012).

The large and small subunits associate via a number of contact points, called intersubunit bridges, and association depends on ionic conditions and the presence of tRNA and protein ligands (Frank et al., 1995; Liu and Fredrick, 2016; Tissières et al., 1959). The intersubunit bridges are not rigid, but rather undergo rearrangements during translation, allowing the two subunits to rotate relative to one another. The intersubunit rotation can create movements of up to 20 Å in the periphery of the ribosome (Frank and Agrawal, 2000; Valle et al., 2003). Necessary during translation elongation (Horan and Noller, 2007), this rotation corresponds to tRNA movement with respect to the 50S, i.e., the formation of tRNA hybrid states (Moazed and Noller, 1989a, 1989b).

1.3.3. The ribosome has a dynamic structure

Mirroring the dynamic nature of protein synthesis, ribosome structure is far from rigid (Korostelev et al., 2008). In addition to intersubunit rotation, each subunit can undergo a number of coordinated movements. For instance, despite an apparently rigid core, the 50S subunit has at least two major areas of large-scale structural dynamism. One is called the L1 stalk, composed of the L1 protein and helices H76-78 of 23S rRNA. It interacts with the elbow of the E-site tRNA and moves in coordination with E-site occupancy (Cornish et al., 2009; Trabuco et al., 2010). Located on the opposite side of the subunit are the L11 stalk (composed of protein L11 plus helices H42-44 of 23S rRNA) and its associated L7/L12 stalk (composed of L10 and two L7/L12 dimers). They make up the bulk of the GTPase-associated center of the ribosome, with which translation factors such as IF2, EF-Tu, EF-G, and RF3 associate in their GTP-bound form. Movement of the L7/L12 stalk is correlated with GTPase binding (Diaconu et al., 2005).

The 30S subunit appears to be more flexible than 50S, based on deformations commonly seen in crystal structures, most notably in the “spur” and “beak” regions of the subunit which correspond to helices h6 and h33 of 16S rRNA, respectively. Also flexible is the 3’ tail of 16S rRNA, which includes the anti-Shine-Dalgarno sequence, and can pair with the mRNA at the initiation stage of bacterial translation. However, the most prominent movement in 30S is that between the head domain (helices h28-43 of 16S rRNA plus ribosomal proteins S1, S2, S3, S7, S9, S10, S13, S14, and S19) and the body domain (remainder) of the subunit, which are separated by a “neck” region (helix h28) (Fischer et al., 2010; Guo and Noller, 2012; Ratje et al., 2010; Schuwirth et al., 2005). Two coupled hinge motions, one within the neck helix and one in the h35-h36 linker in the head domain, produces a rotational movement of the head with respect to the body (Mohan et al., 2014). This movement, described as swiveling, is facilitated by EF-G during translation elongation, and accompanies tRNA/mRNA translocation into chimeric hybrid states. Head rotation (without chimeric hybrid state formation) is also induced by release factor 3 in translation termination (Jin et al., 2011; Zhou et al., 2012).

1.3.4. The mRNA is threaded around the neck of the small subunit

In crystal structures of the bacterial ribosome, the mRNA is seen to wrap around the neck of the small subunit (Yusupova et al., 2001). The 5’ end of the mRNA is near the back of the platform (composed of helices h23 and h24 of 16S rRNA) and can base-pair with the 3’ end of the 16S to form the SD helix. Near the center of the neck, the mRNA is exposed and can interact with the P- and the A-site tRNAs. Downstream from the tRNA binding sites, it passes through a tunnel walled by residues of the 16S rRNA (helix h34 from the head domain, plus the tips of helices h1 and h18, and the base of h44 from the body domain) and further downstream by ribosomal protein S3 in the head domain of the small subunit, and ribosomal proteins

S4 and S5 in the body domain. This overall path for the mRNA seen in a crystal structure was proposed earlier (Frank et al., 1995; Lim et al., 1992) and was confirmed by later structural studies (Jenner et al., 2010; Yusupova et al., 2006).

1.3.5. Ribosomal proteins line the entrance to the mRNA tunnel

The path of the mRNA described above implicates S3, S4, and S5 as suspects for contributing the most to the helicase activity, as they are at the tunnel entrance (Fig. 1A). At least for S3 and S4, mutational analysis supports such contribution (Takyar et al., 2005). All three proteins are essential in bacteria (Shoji et al., 2011), and each belongs to a universally conserved family of ribosomal proteins found in all domains of life (Ban et al., 2014). The C-terminal domain of protein S3 has an α+β fold and forms part of the mRNA tunnel wall near the entrance. It has several highly conserved residues near the tunnel entrance, including arginines 131 and 164 inside the tunnel, and arginines 132 and 136, and lysine 135 outside of the tunnel. In the N-terminal domain, which is further away from the tunnel entrance, this protein contains a type 2 protein K homology (KH2) domain. KH domains are found in a large number of RNA-binding proteins, and recognize their target RNA through a hydrophobic groove that interacts with the bases of a core tetranucleotide in the RNA, with different degrees of sequence specificity in different KH domains (Grishin, 2001; Valverde et al., 2008). The groove is formed by two α-helices separated by a loop containing an invariant GXXG motif (corresponding to residues 78-81 in *E. coli* S3) on one side, and a β-strand followed by a so-called variable loop on the other (Fig.

1B). Whether the KH domain of S3 is involved in mRNA binding during translation is not known.

Protein S4 contributes to the tunnel entrance by projecting a loop (residues 43-50) that invariably contains at least two (often three or four) positively-charged residues in all bacteria. The loop is well positioned to act as a corral to confine the mRNA in the enclosure between the head and shoulder of the small subunit. In eukaryotes, where protein S4 is located further away from the tunnel entrance, the C-terminal segment of ribosomal protein eS30 is projected to the same position (Rabl et al., 2011), and also invariably contains at least two positively-charged residues (Fig. 1C). When the 30S head (containing S3) moves away from the body (containing S4) in a swiveling motion during translocation (Ratje et al., 2010; Zhou et al., 2014), the shape of the tunnel entrance changes, and this S4 loop may then sterically block the accommodation of bulky structures in the immediate vicinity of the tunnel entrance.

Protein S5 is notable for containing a *double-stranded* RNA-binding motif (DRBM) in its N-terminal half. The motif interacts on one side with helices h28 and h34 of 16S rRNA in the neck region of the small subunit. On the distal side of the motif, which is solvent-exposed and positioned in front of the tunnel entrance, the protein contains a short N-terminal segment (residues 1-8) that has not been resolved in crystal structures of bacterial ribosomes and may be disordered. At this position in canonical DRBMs, there is a short α-helix that is involved in minor groove interactions with double-stranded RNAs (Fierro-Monti and Mathews, 2000) (Fig. 1D). It is not known if S5 possesses a bona fide dsRNA binding activity.

1.4. The Ribosomal Helicase

1.4.1. mRNA helicase activity is intrinsic to the ribosome

As a consequence of simple base-pairing, roughly half of an RNA of a random sequence is base-paired in solution (Doty et al., 1959), and mRNAs are no exception to this general rule (Holder and Lingrel, 1975; McMullen et al., 1967; Min Jou et al., 1972; Watts et al., 2009). Secondary structures in coding regions of mRNA can slow down translation elongation (Chen et al., 2013; Gorochowski et al., 2015; Wen et al., 2008), but even extensively structured mRNA can be translated (Lingelbach and Dobberstein, 1988). Despite the natural base pairing propensity of coding mRNA *in vitro* (Kertesz et al., 2010), the extent of secondary structures is more limited *in vivo* due to ATP-dependent helicase activities, although many mRNA structures do persist (Rouskin et al., 2014). Furthermore, the persisting structures fold similarly *in vitro* and *in vivo* (Spitale et al., 2015), and show an overall more dynamic behavior *in vivo* (Mahen et al., 2010), indicating a higher turnover for folding inside the cell.

Importantly, although translation initiation requires the assistance of RNA helicases (Parsyan et al., 2011), the ability to unfold the coding regions in mRNAs during translation elongation is intrinsic to the ribosome (Qu et al., 2011; Takyar et al., 2005; Wen et al., 2008) and is tightly coupled to translocation, which is catalyzed by EF-G. However, the antibiotic sparsomycin, which catalyzes translocation in the absence of EF-G (Fredrick and Noller, 2003), also catalyzes mRNA unwinding (Takyar et al., 2005). Thus, although mRNA unwinding is coupled to translocation, it does not require GTP hydrolysis by elongation factors, at least in a single-turnover assay.

The helicase activity should therefore be driven by the mechanical forces inherent in the conformational changes during translocation. Translation in the absence of factors or GTP has been observed *in vitro* (Gavrilova et al., 1976; Pestka, 1969), where the only free energy input to translation comes from the peptidyl transfer reaction between aminoacyl- and peptidyl-tRNAs (Spirin, 2009). Whether this input is significant in ribosomal translocation has been questioned in favor of an EF-G-*driven* powerstroke paradigm (Agrawal et al., 1999; Chen et al., 2016; Rodnina et al., 1997), but a Brownian ratchet mechanism, in which EF-G simply acts as a rectifier to prevent the reverse motions during translocation, is also likely (Liu et al., 2014b), and these two models are not mutually exclusive. In the presence of stable mRNA structures, translocation may require coupling to GTP hydrolysis by EF-G in order to become thermodynamically favorable at all, because mRNA stability for three nucleotides (one codon) of a long hairpin is predicted, based on nearest neighbor rules (Andronescu et al., 2014; Tinoco et al., 1973; Xia et al., 1998), to easily exceed the energy released in peptide bond formation (Liu et al., 2014b) by a wide margin. Notwithstanding, the translocation mechanism can in principle be the same with or without EF-G (Chen et al., 2016), and so can the mRNA unwinding pathway. Of course, translocation and mRNA unwinding *kinetics* are clearly dependent on EF-G, since translocation along mRNA is accelerated by this factor (Katunin et al., 2002; Rodnina et al., 1997).

1.4.2. The ribosomal helicase shows a unique kinetic behavior

Nucleic acid helicases are involved in a plethora of cellular processes, including DNA replication, recombination, and repair. Helicases are grouped into six superfamilies based on sequence homology, and can be processive or non-processive (Singleton et al., 2007). All RNA-specific helicases belong to the SF1 and SF2 superfamilies, and are heavily involved in various stages of gene expression (Bourgeois et al., 2016; Jankowsky, 2011; Martin et al., 2013; Rocak and Linder, 2004). The largest group of RNA helicases is comprised of members of the DEAD-box family within SF2 (Cordin et al., 2006; Jarmoskaite and Russell, 2011), named after the amino acid sequence DEAD in a Walker B motif in their ATP-binding pocket (Linder et al., 1989).

Processive helicases translocate along a single-stranded nucleic acid track and displace the complementary strand as they do so. To what extent the rate of translocation by a helicase is reduced once it encounters a base-paired region, relative to that of unhindered translocation, has been used to classify helicases as active or passive (Betterton and Jülicher, 2005; Lohman and Bjornson, 1996; Manosas et al., 2010). Whereas a fully active helicase has the same translocation rate through base-paired and non-base-paired regions, the rate for a fully passive helicase is limited by the spontaneous thermal opening of the junction in a base-paired region. For example, a nucleic acid region that is on average open only 1% of the time would reduce the rate of translocation for such a helicase by 100-fold. A fully passive helicase therefore operates by product stabilization, i.e. binding to the spontaneously unwound strand.

Such a helicase can still bias the unwinding of nucleic acids in an ATP-dependent manner, but its kinetics is slower than that of active helicases. Active helicases interact with the RNA beyond their active site to destabilize the junction, such that the chance of encountering a closed junction is reduced. Different helicases can be active to different degrees, and a clear distinction may prove to be elusive (Manosas et al., 2010).

Adopting this classification, the ribosome is an active helicase (Qu et al., 2011). Furthermore, unlike other helicases studied by force spectroscopy, the kinetics of the ribosomal helicase cannot be accounted for by only a single active mechanism as formulated in current models (Betterton and Jülicher, 2005; Manosas et al., 2010). It maintains a minimal translation rate, almost half of its maximal rate, and a robust 1-codon step size even over highly stable mRNA hairpins. It was proposed, based on quantitative analysis, that the ribosome must use two active mechanisms to unwind mRNA structures (Qu et al., 2011). One is a classical active mechanism described above, and as expected, this mechanism is enhanced by applying external pulling forces on the ends of mRNA, which favors spontaneous unwinding. However, the second inferred mechanism is force-independent, and has to involve translocation directly over a closed junction. A sound physical explanation for the second mechanism is not immediately evident. Even a fully active classical helicase cannot proceed over a closed junction; it merely reduces the probability that the junction is closed. Furthermore, even the structural basis for the first active mechanism by the ribosome is still not understood.

1.4.3. Where is the helicase active site?

One would expect the helicase active site to be near the point where an incoming mRNA segment is encountered by the ribosome. Therefore, the region on the mRNA over which it interacts with the 70S ribosome would give a first clue as to where the helicase active site may be located. This has been studied by a variety of techniques, including footprinting analyses (Beyer et al., 1994; Hüttenhofer and Noller, 1994; Steitz, 1969). Defining the first nucleotide of the P-site codon as +1, an overall consensus from these early studies seems to be protection of the mRNA up to position +15, consistent with the range of sizes observed for ribosome-protected fragments in ribosome profiling methods in *E. coli* (Mohammad et al., 2016). A similar number is obtained from toeprinting analyses (Hartz et al., 1988), although toeprinting results are compounded by the interactions between the ribosome and the reverse transcriptase enzyme used for the readout.

Structural studies have resulted in different estimates for the length of mRNA within the tunnel, likely due to difficulty in resolving individual nucleotides at low resolution. Whereas early studies placed the tunnel entrance at position +15 (Yusupova et al., 2001), in agreement with the estimates above, it later became clear that the tunnel holds fewer nucleotides, only up to position +12 (Jenner et al., 2010; Yusupova et al., 2006).

The position of the helicase active site in the 70S ribosome was also directly addressed by a carefully designed oligonucleotide displacement assay (Takyar et al., 2005). When controlled stepwise translocation took place, the equilibrium position in the binding of labeled oligonucleotides to mRNA, as measured by gel retardation, was seen to shift toward unbinding. The active site was localized to position +11 by fitting the observed patterns of the shift to predicted values. With available structural data at the time, this placed the helicase active site near the middle of the downstream tunnel. With the more recent structural estimates, however, the biochemical localization matches the position of the tunnel entrance.

Another elegant direct estimate for the position of the active site was based on force unfolding of part of an mRNA hairpin by optical tweezers in the presence of a ribosome bound at a certain codon on the mRNA (Qu et al., 2011). The position of the active site was deduced from the length of the unfolded segment, which should represent the distance between the active site and the known distal end of the unfolded segment. A good fit to the data was found to place the active site at position +13±2, in general agreement with other estimates.

An indirect approach that informs of the position of the active site was based on the quenching of a pyrene dye attached to the end of a short mRNA (Studer et al., 2003). A change in quenching was observed upon moving the position of the dye on the mRNA from +15 to +12, placing the point of first contact somewhere in between these two positions. Interestingly, a slight decrease in quenching was observed upon moving from position +12 to +9, consistent with a less confined environment after passage through the tunnel entrance.

Together, these estimates point to the neighborhood of the mRNA tunnel entrance as the site where mRNA unwinding occurs.

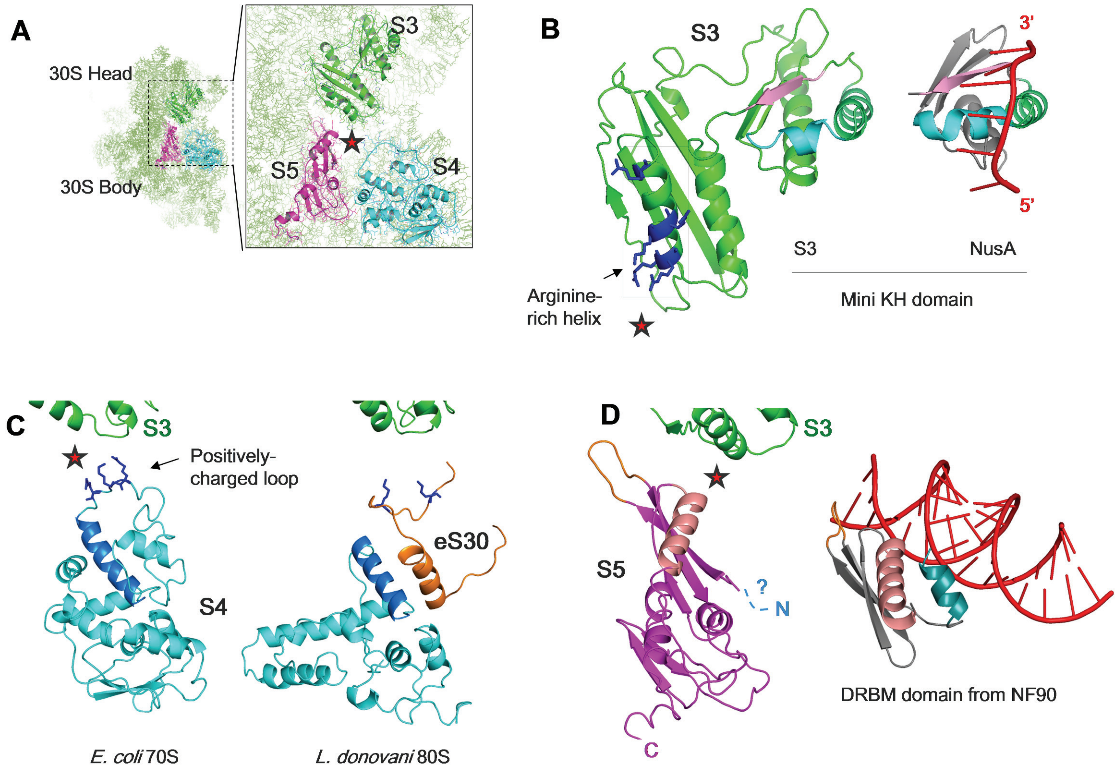

Figure 1.1. Proteins surrounding the mRNA tunnel entrance. *A.* An overview of the proteins surrounding the downstream tunnel entrance, which is indicated by a red star. *B.* In addition to an arginine-rich α-helix near the entrance, protein S3 has a type II KH domain in its N-terminal lobe. For comparison, the C-terminal KH-domain of the transcriptional regulator protein NusA from *M. tuberculosis* (PDB ID 2asb) (Beuth et al., 2005) is shown. The bound RNA is in red, and the structural elements important in NusA RNA binding are color-coded. The NusA-RNA interaction is sequence-specific and forces the RNA into an extended conformation. *C.* Protein S4 projects a conserved positively-charged loop toward the entrance. In eukaryotes, as represented by *L. donovani* (PDB ID 5t2a) (Zhang et al., 2016), uS4 is further away from the tunnel entrance (color-coded), and the loop is replaced by a C-terminal positively charged segment from eS30. *D.* Protein S5 has a DRBM motif in its N-terminal lobe. For comparison, the DRBM domain of the post-transcriptional

regulator NF90 from *M*. *musculus* bound to an RNA duplex (PDB ID 5dv7) (Jayachandran et al., 2016) is shown. Structural elements important in NF90 binding are color coded. The N-terminal segment of S5 corresponding to the first α-helix in the motif has not been structurally resolved.

Chapter 2. Structural Clues to the Nature of the Ribosomal Helicase

2.1. Abstract

Protein synthesis in all organisms proceeds by stepwise translocation of the ribosome along messenger RNAs (mRNAs), during which the helicase activity of the ribosome unwinds encountered structures in the mRNA. Despite its significant role in translation, a detailed understanding of the ribosomal helicase is lacking. Here, we present the crystal structure of the *Escherichia coli* ribosome in complex with a hairpin-containing mRNA. The presence of the hairpin induces a large-scale rearrangement in the crystal lattice, although the hairpin itself is disordered and does not interact with the ribosome. Instead, the mRNA is relocated relative to the ribosome, and three nucleotides preceding the hairpin are seen in an extended conformation on the solvent side of ribosomal protein S3, interacting with residues Arg132 and Arg136 of S3 just outside of the mRNA tunnel entrance. This suggests a preference for binding of single-stranded, rather than double-stranded, mRNA to S3 immediately outside of the tunnel entrance. Such a preference implies the existence of two helicase active sites where mRNA unwinding can occur; a proximal active site located at the tunnel entrance, and a distal active site located three nucleotides downstream.

2.2. Introduction

The ribosome carries out templated protein synthesis in all cells by reading the genetic information in messenger RNAs (decoding), catalyzing the addition of amino acids to nascent polypeptide chains (peptidyl transfer), and moving mRNA and tRNA molecules in concert through its internal binding sites (translocation). Concomitant with these major activities are a host of coordinated ribosome functions at different stages of translation. Key among them is the intrinsic ability of the ribosome to unwind structured mRNAs prior to the decoding step (Qu et al., 2011; Takyar et al., 2005). This is to ensure unhindered translation on mRNA, a molecule with the possibility to form secondary and tertiary structures. Challenging the helicase, highly stable structures in mRNAs can stall the ribosome, and given the right sequence context, shift the reading frame (Baranov et al., 2002; Giedroc and Cornish, 2009; Tholstrup et al., 2012). This frameshifting can occur endogenously, or it can be induced by viruses, some of which are potent human and animal pathogens (Brierley, 1995; Namy et al., 2004).

The ribosome appears to be a helicase of its own kind (Takyar et al., 2005). It has no homology to previously-known superfamilies of nucleic acid helicases, all of which consist of ATP-binding domains and use the energy of ATP hydrolysis to change conformation and catalyze the separation of nucleic acid strands (Caruthers and McKay, 2002; Pyle, 2008). Of note are the large DEAD-box family of RNA helicases that do not require ATP hydrolysis for the strand-separation step of the catalysis cycle, but rather hydrolyze ATP to release their bound single-stranded RNA product afterwards (Linder and Jankowsky, 2011). In other words, such single-stranded RNA binding proteins are helicases simply because they have a mechanism for multiple turnovers. Other RNA helicases processively translocate along single-stranded RNA in either 5'-to-3' direction (e.g. the Rho helicase involved in transcription termination in bacteria (Brennan et al., 1987)) or 3'-to-5' direction (e.g. the NS3 helicase involved in replication of the Hepatitis C virus (Beran et al., 2006)) and displace the complementary strand in the process. Of course, the ribosome is a processive 5'-to-3' mRNA translocator. Additionally, its components may passively unwind mRNAs by equilibrium binding, as exemplified by its S1 component (Qu et al., 2012).

The path of the mRNA around the neck of the small ribosomal subunit has been observed by crystallography (Yusupova et al., 2001). The mRNA enters the ribosome through a tunnel between the head and shoulder of the subunit, the entrance of which is lined by ribosomal proteins S3, S4, and S5. The electron density for the segment of mRNA that lies in the tunnel is characteristically weak in crystal structures of the ribosome (Jenner et al., 2010; Yusupova et al., 2006), although the structure of the chimeric hybrid-state ribosome shows density for the translocated mRNA by up to position +21 (equivalent to position +18 without translocation), where the 3’ tail of the mRNA interacts with the base of the KH domain in protein S3 (Zhou et al., 2014).

It is not clear how the ribosome interacts with an encountered mRNA structure such as a hairpin. One possibility (Yusupova et al., 2001) is that the head domain of the small subunit interacts with one strand of the hairpin, while the body domain interacts with the other, to physically pry apart the two strands during translocation, when the head moves relative to the body (Guo and Noller, 2012; Ratje et al., 2010). In this picture, some structures (e.g. pseudoknots) evade unwinding due to their poorly matched structural geometry with respect to that of the tunnel entrance. However, for a helicase that encounters base-paired segments only sporadically, such a mechanism might be counterproductive because binding to a closed junction can indeed favor its formation. For example, although some DEAD-box helicases can bind to either single-stranded or double-stranded RNA, they always bind the former with higher affinity (Jarmoskaite and Russell, 2011; Linder and Jankowsky, 2011). If a similar product stabilization strategy is used by the ribosomal helicase, it is conceivable that some structures may evade unwinding precisely because of a close match to the geometry of the tunnel entrance.

To shed light on the mode of interaction between the ribosome and secondary structures in the mRNA, we used X-ray crystallography to determine the structure of the ribosome in complex with a hairpin-containing mRNA. In the structure, single-stranded mRNA, rather than the hairpin, is seen to interact with protein S3 immediately outside of the tunnel. The S3-bound mRNA is found in an extended conformation that deviates from standard A-form geometry. mRNA relocation and significant crystal packing rearrangements are observed in the presence of the mRNA hairpin. Furthermore, full-length cognate A- and P-site tRNAs are observed in the structure, and the elbow of the A-site tRNA is seen to induce a conformational change in the A-site finger. Finally, our functional assays show that eliminating S3-mRNA binding interactions near the tunnel entrance can result in mRNA-dependent tRNA binding defects.

2.3. Results

2.3.1. Crystal packing is rearranged in the presence of an mRNA hairpin

We set out to determine the crystal structure of the *E. coli* 70S ribosome in complex with a hairpin-containing mRNA. As shown in Fig. 2.1A, the mRNA contains a relatively weak Shine-Dalgarno (SD) sequence, a start (AUG) codon, three consecutive valine (GUA) codons, a spacer sequence, and a 4-bp-stem hairpin capped by a UUCG tetraloop. We tested a range of spacer lengths, from 4 to 8 nucleotides, by changing the number of adenosines preceding the hairpin. The complex was made using an indirect approach (Fig. 2.1A) in which the ribosome was first bound on the mRNA at the start codon in the presence of charged initiator tRNA; this was followed by in vitro translation in the presence of purified valyl-tRNA$^{\mathrm{Val}}$·EF-Tu·GTP ternary complex, EF-G, and GTP, in order to translocate by three valine codons on the message and "pull" the hairpin into the helicase active site. This approach, rather than direct binding near the hairpin, was taken to prevent the mRNA structure from interfering with initial ribosome binding on the mRNA, as suggested by our previous attempts (J. Zhu, unpublished data). The complexes were then crystallized and cryoprotected, and low-resolution (~7-10 Å) structures were determined by molecular replacement. The density in front of the tunnel entrance was strongest when the mRNA with 5-nt spacing between the last valine codon and the hairpin was used (pH03H9 mRNA, Fig. 2.1A). We solved the structure of this complex at ~3.9 Å resolution (Table 2.1, Supp. File 1 and Supp. File 2).

The complex crystallized in the P 2_1 2_1 2_1 space group, with two ribosomes (A and B) in the asymmetric unit. Both ribosomes are in the classical state, as judged by the degree of rotation of the 30S subunit and its head domain (Mohan et al., 2014). However, the crystal packing in this structure deviates from those in the previously-published structures of this space group (Dunkle et al., 2011; Jenner et al., 2010; Schuwirth et al., 2006; Selmer et al., 2006), due to a large-scale rigid-body rearrangement of the ribosomes that slightly opens up the space near protein S3 outside of the tunnel entrance, presumably to allow room for the mRNA hairpin (Fig. 2.2). Notably, crystal contacts involving protein S3, which are seen in other crystal structures of wild-type 70S ribosomes, are absent in both ribosome molecules in our structure.

Another notable remodeling of crystal contacts is observed between protein L9 in one ribosome (A or B) and 16S rRNA in the neighboring ribosome (B or A, respectively) (Fig. 2.3). In the classical and hybrid-state ribosomes of the same space group, the globular C-terminal domain of L9 is in contact with helix h5 and the base of helix h15 of the neighboring 16S rRNA, in part by a stacking interaction between the bulged A55 adenine in helix h5 and the Phe91 aromatic side chain in L9. In ribosome A in our structure, the C-terminal domain of L9 is repositioned by ~ 30Å toward the spur helix (h6) in the neighboring 16S rRNA, losing the Phe91-A55 stacking interaction. Furthermore, in the classical and hybrid-state structures, Ser93 of L9 is close to the backbone phosphate of U368 in helix h15. In ribosome A in our structure, the L9-16S contacts on one side of Ser93 are lost, and new interactions are observed on the other side, while Ser93 itself maintains contact with the 16S rRNA of the neighboring ribosome B, interacting instead with the backbone phosphate of C370, about 13Å away from U368 (Fig. 2.4, *top*). This mode of interaction between L9 and 16S rRNA has not been observed previously. In ribosome B, compared to the classical and hybrid states, the C-terminal domain of L9 is relocated by ~15Å, in this case toward the center of the neighboring 16S rRNA, such that Ser93 interacts with the phosphate of G360 (Fig. 2.4, *bottom*), similar to what was observed, but not noted, in the structure of the *E. coli* ribosome in the presence of the antibiotic kasugamycin (Schuwirth et al., 2006).

2.3.2. mRNA is relocated in the presence of hairpin

Both ribosomes in the asymmetric unit contain tRNAs bound to the A and P sites. Ribosome A also contains E-site tRNA, whereas ribosome B has a very low occupancy for this tRNA. In each ribosome, the A- and P-site tRNAs are involved in cognate base pairing with the first two valine codons in the mRNA. We performed toeprinting experiments using control mRNAs that lack the hairpin, and confirmed efficient P-site tRNA binding at the start codon and the consequent translocation of the ribosome onto the last valine codon (Fig. 2.1C). Accordingly, the presence of a cognate A-site tRNA in the structure was unexpected, since completing the three in vitro translation cycles should result in a vacant A site. This can be explained by an mRNA relocation event (Fig. 2.1B) during the long crystallization period, in part enhanced by the presence of the mRNA hairpin.

2.3.3. Single-stranded mRNA binds protein S3 outside of the tunnel

The electron density for the mRNA is strongest in the A and P sites and diminishes outside of this region. Nevertheless, it is seen to continue upstream to form an imperfect SD helix in an orientation that resembles the previously-observed post-initiation state (Yusupova et al., 2006). This is consistent with the 7-nucleotide spacing between the SD sequence and the first valine codon in the P-site, predicted from the relocated mRNA described earlier.

Downstream of the A site in each ribosome, the mRNA density continues through the tunnel (Fig. 2.5), where mRNA bases at positions +6 and +7 (relative to the first P-site codon nucleotide designated as +1) are stacked, and nucleotide C1397 at the base of helix h44 of 16S rRNA is tucked in away from the +7 base, similar to what was seen in elongation complexes previously (Jenner et al., 2010). The mRNA then appears to flip its orientation after position +9 or +10, in ribosomes A and B respectively (see below), such that its backbone faces S3 when it emerges at the tunnel entrance at position +12. Outside of the tunnel, the mRNA continues as a single strand for three additional nucleotides (up to position +15), running along the arginine-rich α-helix that spans residues 130-142 of protein S3. The mRNA appears to interact with S3 via its backbone phosphates, spaced apart in an extended and straightened conformation that deviates significantly from the curvature of A-form geometry (Fig. 2.6). The amino acid side chains in consecutive turns of the S3 α-helix (including arginine 132, lysine 135, and arginine 136) approach the mRNA backbone.

In particular, in ribosome B, Arg132 is close to the backbone phosphates of +14 and +15 nucleotides, while Arg136 is close to the latter phosphate only. The electron density corresponding to the first nucleotide of the hairpin stem (at +15) is visible. However, the rest of the hairpin is disordered, indicating that it is not interacting stably with any of the nearby ribosomal components.

Examination of the electron density maps and of the refined temperature factors for the mRNA beyond the tunnel entrance reveals an elevated level of background density and disorder in this region (Fig. 2.6), suggesting that mRNA binding along S3 outside of the tunnel is flexible, and that a number of different configurations may be possible. Furthermore, TLS refinement of the anisotropic displacement parameters show a relatively high displacement in the plane of the bases in this region of the mRNA (Fig. 2.7), suggesting that the mRNA has some freedom to move laterally relative to the direction of its backbone.

2.3.4. mRNA binding to S3 varies in different ribosomes

The environment immediately in front of the tunnel entrance on the surface of the ribosome is different in the two ribosomes. It is more crowded in ribosome A, where proteins S6 and S18 from ribosome B (in the adjacent asymmetric unit) are in close proximity, ~ 20 Å, to the entrance (Fig. 2.8). It should be noted that S6 and S18 both project toward the tunnel entrance their unstructured regions (C- and N-terminal tails of 35 and 18 amino acid residues, respectively) that are disordered in this as well as previous crystal structures. Thus, the crowding is even more severe than it appears in the model. In contrast, the space in front of the tunnel entrance in ribosome B is relatively open, and the closest approach from the neighboring ribosome A is made by its protein S11, which interacts with the distal side of protein S4 in ribosome B, about 40Å away from the tunnel entrance. We thus consider ribosome B to represent a more relaxed environment in front of the tunnel entrance that is less perturbed by nearby crystal contacts.

Interestingly, ribosomes A and B show slightly different paths for the mRNA outside the tunnel and even as early as position +8 which is within the tunnel (Fig. 2.9A). With the different crowding conditions in front of the tunnel entrance mentioned above, the 3'-end of mRNA in ribosome A is pushed away from protein S4 and toward protein S5. Despite this, the mRNAs in both ribosomes A and B maintain contact with the same α-helix in protein S3, which does not move (Fig. 2.9B). The upstream mRNA segment (+8 to +11) appears to follow this displacement and change course accordingly (Fig. 2.9A).

In ribosome B, the mRNA base +10 approaches the side chains of the universally conserved arginines 131 and 164 inside the tunnel (Fig. 2.5). In ribosome A, which is subject to more crowding from outside of the tunnel, this interaction is lost and the +10 base is flipped away from S3. However, Arg131 is now in position to interact with the backbone phosphates of nucleotides +11 and +12. Complementing this behavior on the other side of the tunnel wall, Arg19 in S5 interacts with the backbone phosphates of nucleotides +10 and +11 in ribosome A, and with the +10 base in ribosome B (Fig. 2.5). These differences suggest that mRNA interactions within the tunnel are not unique and can vary in different ribosome molecules.

2.3.5. The A-site finger moves in the presence of A-site tRNA

To our knowledge, this is the first reported observation of a full-length A-site tRNA in an *E. coli* ribosome crystal structure. Interestingly, among crystal structures of classical state 70S ribosomes containing full-length cognate A-site tRNA, the conformation of tRNA^{Val} in our *E. coli* structure, with no antibiotics, is closer to that of tRNA^{Gln} in *T. thermophilus* complexes in the presence of viomycin or capreomycin (antibiotics thought to stabilize A-site tRNA binding) (Stanley et al., 2010) than that of tRNA^{Val} (same isoacceptor type), tRNA^{Phe}, or tRNA^{Lys} in the absence of antibiotics (Jenner et al., 2010; Rozov et al., 2016a, 2016b). In this conformation, the acceptor arm is moved by about 5 Å away from the P-site tRNA, widening the gap between the two tRNAs in the ribosome (Fig. 2.10). We observe stacking of the bulged A896 in the A-site finger (helix H38) of 23S rRNA on the G19:C56 tertiary base pair, which is formed between the D and T loops of the A-site tRNA. Forming this interaction, the finger helix has moved toward the tRNA elbow compared to the *E. coli* complexes with a vacant A site (Fig. 2.11). The flipping of the 16S rRNA bases G530, A1492, and A1493 in the decoding center of the small subunit, and a closure of the shoulder of the small subunit in the presence of cognate A-site tRNA are also observed as reported previously (Ogle et al., 2002) (Fig. 2.12).

2.3.6. S3 mutations lower mRNA-dependent tRNA binding *in vitro*

To test if the S3-mRNA interactions observed in the crystal structure are functionally relevant, 70S ribosomes containing either the wild-type or a mutant S3 protein (in which Arg131, Arg132, and Lys135 are mutated to alanine (Takyar et al., 2005)) were reconstituted *in vitro* and compared in their mRNA-dependent tRNA binding activity using the nitrocellulose filter binding assay. We used tRNA binding as a proxy for specific mRNA binding, as direct measurement of mRNA binding can be obscured by nonspecific interactions. Accordingly, tRNA binding was conducted in buffer containing 10 mM Mg^{2+} and was shown to be mRNA-dependent: estimated affinity for the binding of fMet-$tRNA^{fMet}$ to wild-type reconstituted ribosomes in the presence of fMVVV mRNA (at 2-fold molar excess) was about 150-fold higher than that in the absence of mRNA (Table 2.2, rows 1 and 4). Binding in the absence of mRNA suggests a 2:1 stoichiometry (two tRNAs per ribosome) for mRNA-free ribosomes, in contrast to a 1:1 stoichiometry for ribosomes programmed with mRNA (Table 2.2, rows 1 and 4 last column), consistent with nonspecific tRNA binding to either A or P site in the former, but only specific binding to the P site in the latter.

Importantly, tRNA binding affinity in the presence of fMVVV mRNA was lower by about 50-fold in ribosomes reconstituted with the mutant S3 protein compared to those with wild-type S3 (Fig. 2.13A, and Table 2.2 rows 1 and 2). Despite lower affinity, mRNA-dependent tRNA binding in the mutants approached that of wild-type at saturating tRNA concentrations, indicating a competitive effect. For comparison, reconstituted ribosomes lacking protein S3 showed a more severe tRNA binding defect (Fig. 2.13A, and Table 2.2 row 3), and binding with these ribosomes did not reach that of wild-type in these experiments. As a control, tRNA binding affinity in the absence of mRNA was not significantly affected in the mutants (Fig. 2.13A, and Table 2.2 rows 4 and 5). Similarly, tRNA binding in buffer containing 20 mM Mg^{2+}, which is mostly mRNA-independent, shows no significant difference between wild-type and mutant ribosomes (Table 2.2 rows 6-9). Together, these results indicate that the S3 mutations reduce tRNA binding affinity in an mRNA-dependent manner, and suggest that efficient P-site tRNA binding may require S3-mRNA interactions. The tRNA binding deficiency in the mutant was also detected in the toeprinting assay (Fig. 2.13B).

2.3.7. S3 mutations confer cold-sensitivity in yeast

Alanine mutation of Arg131 and Arg132, which was sufficient to significantly reduce P-site binding in the toeprinting assay, was also introduced genomically in *Saccharomyces cerevisiae* (the homologous residues being Arg116 and Arg117) to examine its effect *in vivo*. We chose *S. cerevisiae*, as genomic mutations can be readily introduced in this organism. The mutant yeast cells were viable, indicating that these residues are not essential in yeast despite their universal conservation. At either 30°C or 42°C, growth rates on YPD media were comparable between wild-type and mutant cells. However, the mutants were cold-sensitive, as judged by their significantly slower growth rate at 16°C compared to wild type cells (Fig. 2.13C).

2.4. Discussion

2.4.1. mRNA binds to S3 outside of the tunnel

The crystal structure of the *E. coli* ribosome in complex with a hairpin-containing mRNA has revealed that the hairpin (a helicase substrate) does not stably interact with the ribosome. Instead, single-stranded mRNA (the helicase product) binds protein S3 outside of the tunnel (Fig. 2.6). We do not detect electron density corresponding to the hairpin itself, although we take the observed large-scale crystal lattice rearrangement (Fig. 2.2) as evidence for the presence of the hairpin in the crystal. Relocation of the mRNA as seen in this structure (Fig. 2.1B) would move the hairpin away from tunnel entrance, allowing its preceding single-stranded mRNA to interact with the ribosome near the entrance.

Interestingly, the mRNA path is different in ribosomes A and B, likely caused by difference in crowding in front of the tunnel entrance (Fig. 2.8). The path difference is seen not only outside of the tunnel, but even in several upstream nucleotides within the tunnel, strongly suggesting that the mRNA in the tunnel is not held in place tightly. Even the interactions of mRNA observed within the tunnel, e.g. with Arg19 of S5, and Arg131 and Arg164 of S3, appear to be somewhat flexible, because they are different in the two ribosomes (Fig. 2.5). The observed flexibility, mediated by arginine side chains which can bind nucleic acids in various modes (Morozova et al., 2006), suggests that the ribosome can hold onto the mRNA in the tunnel in more than one way and does not strictly limit mRNA path, consistent with the tendency of this mRNA segment to resolve poorly in crystal structures.

Additionally, such flexibility highlights the ability to transfer force uninterruptedly along the mRNA within the tunnel, which is of great functional significance. The forward and reverse rotations of the 30S head during translocation (Ratje et al., 2010; Zhou et al., 2014) effectively move the body portion (S4 and S5) and the head portion (S3), respectively, of the tunnel entrance away from the tRNA sites that anchor the mRNA codons. This is equivalent to a force along the intervening region of mRNA that pulls the mRNA toward the ribosome interior, providing the free energy to unwind incoming mRNA structures. Accordingly, tight binding interactions between the ribosome and this region of mRNA would interrupt the force transfer and could hamper the helicase activity.

Unfortunately, mRNA binding to S3 outside of the tunnel is also flexible, and an unambiguous all-atom model for nucleotides +12 to +15 cannot be built using our data. However, from the electron-density map, two conclusions can be made confidently. First, it is clear that the mRNA chain runs along S3 and is in position to interact with Arg132 (as well as with Lys135 in ribosome A, and Arg136 in ribosome B). Secondly the mRNA is single-stranded, not only because no electron density for a complementary strand is observed, but also because the straightened path of the mRNA bound to S3 is incompatible with curvature of the backbone in an A-form RNA duplex (Fig 3.1).

Binding of single-stranded mRNA to S3 outside of the tunnel was also observed in the crystal structure of the chimeric hybrid-state *T. thermophilus* ribosome in complex with EF-G (Zhou et al., 2014) (Fig. 2.14). The path of the mRNA outside of the tunnel is similar to what is seen in our classical structure, except that the mRNA in the chimeric-hybrid state ribosome was seen to interact with S3 through its bases rather than its backbone. Regardless of whether this is a genuine difference or simply a modeling artifact (given the resolution of these data), the interaction of single-stranded mRNA with S3 is in agreement with both of these structural results, and it was observed in our structure *despite* the presence of a hairpin. We further note that the mRNA "mimic" in the structure of the eukaryotic ribosome, the Stm1 protein, runs along the same path on S3 (Ben-Shem et al., 2011) (Fig. 2.14). In another example, cryo-EM structure of the *E. coli* ribosome in complex with a hairpin-containing selenocysteine insertion sequence (SECIS) (Fischer et al., 2016) shows that at least with the elongation factor SelB bound to the hairpin, the latter is positioned with its first nucleotide (at position +15) lying against protein S3, close to Arg132 and Arg136. Examination of the cryo-EM density maps shows that although the hairpin model may not be placed with full confidence in the absence of SelB, the base of its stem nevertheless seems to lie at the same location on the surface of S3, and not at the tunnel entrance (Fig. 2.15), meaning that the preceding nucleotides, although not resolved, are in single-strand form and may also interact with S3.

2.4.2. The ribosome has two helicase active sites

In analogy to enzymes, which do not stably interact with their substrates, but rather stabilize transition states or products, stable binding between the ribosomal helicase and a hairpin could disfavor unwinding by this helicase. Preferential interaction with single-stranded mRNA (i.e. product stabilization), as suggested by our structure, would destabilize the hairpin without directly interacting with it, similar to the mode of unwinding in the non-processive DEAD-box helicases (Jarmoskaite and Russell, 2011; Linder and Jankowsky, 2011; Patel and Donmez, 2006).

If one defines a helicase active site as a point where a closed duplex junction is opened, the observed binding of single-stranded mRNA to S3 outside of the tunnel suggests the existence of two helicase active sites. The S3-bound mRNA is already unwound by a distally-located active site outside of the tunnel entrance, before reaching the entrance itself, which constitutes a proximal active site. The proposed mechanism of mRNA unwinding by the tandem arrangement of active sites is described quantitatively in Chapter 3.

Considering previous studies on the ribosome, indications for the existence of two active sites come from the small but nevertheless noticeable discrepancies between the different estimates for the 3’ end of ribosome-mRNA interactions, as described in Chapter 1. For instance, ribosome footprint up to or beyond position +15 (Beyer et al., 1994; Hüttenhofer and Noller, 1994; Mohammad et al., 2016; Steitz, 1969), combined with the length of mRNA within the tunnel (up to position +12) (Jenner et al., 2010; Yusupova et al., 2006), implies mRNA-ribosome interactions outside of the tunnel up to position +15.

Oligonucleotide displacement assays yielded an estimate of +11 for the position of the helicase active site (Takyar et al., 2005). This is precisely the position of the proximal active site (i.e the tunnel entrance) in our model. Why the weaker distal active site was not detected in these experiments can be attributed to the fact that detection was based on gel mobility shift after equilibration in a buffer containing small amounts of the ionic detergent SDS, which may have disfavored the mRNA binding to S3 in competition with binding to the labeled oligonucleotide.

Force-spectroscopy analysis yielded an estimate of +13±2 (Qu et al., 2011). This, considering the experimental uncertainty, agrees with the position of either the proximal or the distal active site. The mRNA used in this experiment had the sequence GGG starting at position +12 (paired with a downstream CCC sequence); according to our estimate for S3 affinity (Chapter 3), this trinucleotide would be partially bound to S3 even without an applied force, resulting in an overestimation of the force-dependent unwinding length. Further complicating the matter, the mechanical force used in such an experiment can affect the S3-mRNA binding equilibrium as well as affecting duplex annealing.

2.4.3. S3-mRNA interaction is functionally important

The 71-nt mRNA used in our biochemical assays (fMVVV mRNA, Table 2.3) lacks any predicted secondary structure or extra AUG codons in any reading frame. This mRNA shows a nanomolar affinity for fMet-tRNA^{fMet} binding to the ribosome, which is significantly compromised when S3 is mutated (Fig. 2.13A,B). Our in vitro results are consistent with the involvement of Arg131 and Arg132 in specific mRNA-dependent tRNA binding, and suggest that in the absence of S3-mRNA binding mediated by these residues, P-site tRNA binding requires a higher concentration of tRNA to compensate for the lack of stable ribosome-mRNA binding, manifested in the competitive effect that was observed in the mutants. We propose that mRNA binding to S3, mediated by these residues in the wild-type ribosome, helps capture the mRNA, allowing for stable ribosome-tRNA-mRNA interactions. When we mutated Arg116 and Arg117 to alanine in yeast S3 (homologous to Arg131 and Arg132 in *E. coli* S3), we observed cold-sensitivity (Fig. 2.13C). This may be due to a ribosomal helicase defect (as cold sensitivity is common in helicase mutants because of stabilization of nucleic acid folding at lower temperatures) or due to defects in ribosome regulation or biosynthesis. When the same residues were mutated to aspartic acid in yeast, translation initiation defects were observed and attributed to compromised ribosome-mRNA binding (Dong et al., 2017), consistent with our in vitro observations.

2.4.4. The ribosome uses a conserved stacking platform for tRNA interaction

We observed relocation of the mRNA relative to the ribosome in the presence of the downstream mRNA hairpin. This positions a valine codon in the A site and allows A-site tRNA^{Val} binding. In the small subunit, the presence of this cognate tRNA induces rearrangements at the decoding site, including the swinging of A1492 and A1493 in helix h44 of 16S rRNA to interact with the minor groove of the first two codon-anticodon base pairs (Moazed and Noller, 1990; Ogle et al., 2002). In the large subunit, the flexible A-site finger (helix H38 of 23S rRNA) twists and closes on the back of the tRNA elbow via stacking of its bulged A896 base on the tertiary

G19:C56 base pair of the tRNA. Stacking on G19:C56 has also been observed in the E site by the G2112:A2169 tertiary base pair of the L1 stalk (helices H77 and H78 of 23S rRNA)(Mohan and Noller, 2017), suggesting that the ribosomal RNA may use the universally conserved G19:C56 base pair as a stacking platform to help position the tRNA at different stages of translation.

2.4.5. mRNA structures may influence polysome structure

Despite being disordered, the hairpin significantly affects the packing of ribosomes in the crystal due to its excluded volume. The rearrangement eliminates S3 crystal contacts, and opens up more space downstream of the S3-mRNA binding interface outside of the tunnel (Fig. 2.2 and Fig. 2.16), corresponding to the expected location of the hairpin (which starts at position +15 of mRNA). With no significant intersubunit or intra-subunit changes, the packing adjustment accommodates the hairpin by the rigid-body movement of individual ribosome molecules. Notably, the globular C-terminal domain of L9 in ribosome A moves by about 30Å to interact with a new interface on 16S rRNA of the neighboring ribosome B (Fig. 2.3 and Fig. 2.4). Dominant mutations in this domain of L9, including the genomic mutation S93F, have been found to enhance stop-hopping in response to bypassing signals in phage-derived mRNA, suggesting a role for Ser93 in mediating mRNA-specific recoding (Herr et al., 2001). One can imagine the transition from the classical-state ribosome to our hairpin complex to resemble a pivot motion of the L9 C-terminal domain (Fig. 2.4) in which Ser93 act as a (moving) pivot point, maintaining the contact between L9 and

16S rRNA during the transition. The structure of the hairpin complex demonstrates how secondary structures in the mRNA can, by modulating ribosome-ribosome interactions in a polysome, communicate indirectly with protein L9 from tens of angstroms away.

The contact between L9 and 16S rRNA of neighboring ribosomes is likely to be a dominant factor dictating the commonly found ribosome crystal packing (Dunkle and Cate, 2011). The packing resembles the top-to-top arrangement observed in bacterial polysomes, and this interaction may also be a key determinant of polysome formation *in vivo* (Brandt et al., 2009). Interestingly, polysomes of different configurations are possible, affected at least in part by the mRNA that is being translated (Christensen and Bourne, 1999). The rearrangement in the hairpin complex structure changes the profile of the polysome array in an asymmetric manner (Fig. 2.16), and provides a structural basis for how local mRNA structures can affect alternative polysome configurations due to the flexibility inherent in the L9-16S rRNA contact. The flexibility, captured in the hairpin complex, may also help explain how elongation factors are able to transiently bind to ribosomes in a polysome, despite the fact that the classical L9 binding interface that is seen in most ribosome crystal structures sterically interferes with factor binding (Gao et al., 2009). The observed movement of L9 eliminates the classical stacking interaction between Phe91 in L9 and A55 in 16S rRNA. This exposes the A55 base, which can then interact with either EF-Tu or EF-G (Sahu et al., 2013).

2.5. Methods

2.5.1. Ribosome preparation

Tight-couple ribosome preparation was performed essentially as described (Moazed and Noller, 1989a). *E. coli* cells (strain MRE600) were grown to mid-log phase at 37°C, and then cooled on ice for 1 h. Clarified French-press lysates were layered on a 38% sucrose cushion in 20 mM Tris-Cl (pH7.0), 500 mM NH_4Cl, 15 mM $MgCl_2$, 6 mM βME and centrifuged in a Beckman Ti60 rotor at 40,000 rpm for 20 h at 4°C to pellet the ribosomes. The ribosomes were salt-washed twice by resuspending in the same buffer containing 500 mM NH_4Cl and centrifuging in a Ti60 rotor at 55,000 rpm for 2 h at 4°C. Resuspended ribosomes were then layered on a 10-35% sucrose gradient in 20 mM Tris.Cl (pH7.0), 100 mM NH_4Cl, 6 mM $MgCl_2$, 6 mM βME and centrifuged in a SW28 rotor at 19,000 rpm for 16 h at 4°C. The collected 70S fractions were pelleted by centrifugation in a Ti45 rotor at 36,000 rpm for 22 h at 4°C, resuspended in the same buffer (no sucrose) containing 10 mM $MgCl_2$ to a final concentration of ~20 mg/mL, and flash frozen. Typical yield was ~15 mg, starting from a 1 L culture. Analytical gradient centrifugations were performed to confirm the purity (>95% by estimation) of the 70S particles in each prep.

2.5.2. mRNA preparation

The mRNAs (Table 2.3) were transcribed *in vitro* using plasmid DNA templates linearized by *Eco*RV (in the case of pH03H9) or amplified by PCR (in the case of fMVVV). About 100 μg of the DNA template was incubated in a 1 mL reaction containing 80 mM K^+-HEPES (pH7.5), 50 mM NaCl, 2 mM spermidine, 30 mM DTT, 20 mM $MgCl_2$, and 12 mM of total NTPs (4.8 mM ATP, 3.6 mM GTP, 2.4 mM UTP, 1.2 mM CTP, adjusted to reflect the biased base composition of the mRNA) in the presence of 3 μL of T7 RNA polymerase and 2.5 units of pyrophosphatase at 37°C for 3 h. The RNA was then gel-purified using 8% PAGE in 8M urea, extracted by phenol-chloroform, precipitated, and resuspended in water.

2.5.3. tRNA preparation

For charging of fMet and Val tRNAs, 10 nmol of each tRNA (Subriden) at 30 μM concentration was incubated in buffer containing 50 mM HEPES (pH7.5), 50 mM KCl, 10 mM $MgCl_2$, 5 mM DTT, 4 mM ATP, plus an 8-fold molar excess of the appropriate amino acid, in the presence of saturating amounts of crude *E. coli* S-100 fraction for 20 min at 37 °C. For fMet, 300 nM of neutral N10-formyltetrahydrofolate was also present in the mix. The tRNAs were phenol-chloroform extracted, ethanol precipitated, and passed through a 1 mL Sephadex G25 spin column in 1mM KOAc (pH5.3). Successful charging was confirmed by acid PAGE analysis.

2.5.4. Elongation factor preparations

For expression and purification of the factors, BL21(DE3) cells expressing 6xHis-tagged EF-G or EF-Tu were induced with IPTG at 1 mM for ~3 h. Lysis and purification was performed at 4°C in buffers containing 50 mM Tris.Cl (pH 7.5), 60 mM NH_4Cl, 7 mM $MgCl_2$, 6mM β-ME, 15% glycerol. All buffers for EF-Tu also contained 10 μM GDP. Affinity purification of French-pressed lysates was performed with Ni-NTA resin using 250 mM Imidazole for elution. Dialyzed fractions were loaded on a Q-FPLC column and eluted by a gradient with peaks at KCl concentration of ~150 mM (EF-G) or 130 mM (EF-Tu). Protein purity was checked with SDS-PAGE analysis.

2.5.5. Complex formation

To form the ribosome complex for crystallization, 400 pmol of *E. coli* 70S ribosome was pre-warmed at 37°C for 10 min. Separately, 800 pmol of the hairpin-containing mRNA pH03H9 (Table 2.3) in water was heated at 90°C for 3 min, snap-cooled in an ice bath for 10 min, brought to 37°C, and added to the ribosome along with 800 pmol of charged fMet tRNA for a total volume of 50 μL in 20 mM Tris.Cl (pH7.0), 100 mM NH_4Cl, 10 mM $MgCl_2$, 6 mM βME, and incubated at 37°C for 20 min for P-site tRNA binding. In parallel, 1800 pmol of the *E. coli* EF-Tu protein was incubated in its storage buffer plus 2 mM GTP and 2 mM $MgCl_2$ at 37°C for 10 min. To this, 1600 pmol of charged Val tRNA was added, and incubation was continued for another 5 min for ternary complex formation in the same buffer as in P-site binding. The ternary complex was then added, plus 1200 pmol of EF-G and final 1 mM GTP, to the P-site binding reaction, and incubated in a total volume of 100 μL at 37°C for 15 min for ribosome translocation. The complex was then brought to room temperature and used for crystallization.

2.5.6. Crystallization and cryoprotection

For sitting-drop crystallization with vapor diffusion, 0.5 µL of the complex was mixed with 0.5 µL of the reservoir mix containing 100 mM Tris acetate (pH7.0), 100 mM KSCN, 4.2% PEG 20,000, and 10-12% pentaerythritol propoxylate (17/8 PO/OH), and equilibrated against 50 µL of the reservoir mix in a 96-well plate at 16°C for up to two weeks. Large rod-shaped crystals (100 µm in the smallest dimension) were then cryoprotected by the stepwise addition of the reservoir mix containing 12, 15, and 20% pentaerythritol propoxylate (17/8 PO/OH) respectively, and equilibration against the same mix for ~24 h at each step. The crystals were then harvested, flash frozen in liquid nitrogen, and screened for X-ray diffraction. The deposited structure was solved using data collected from one ~10-day-old crystal.

2.5.7. Diffraction data collection and structure refinement

Diffraction data were collected at the ALS and the SSRL light sources at the LBL and SLAC national laboratories, respectively, and processed to obtain structure factor amplitudes using the XDS package (Kabsch, 2010). A previously published *E. coli* structural model (Dunkle et al., 2011) was directly used for multiple rounds of rigid-body refinement in PHENIX (Adams et al., 2010) with progressively smaller rigid bodies. After the placement of tRNA models into the difference electron density peaks, further rounds of manual rebuilding with COOT (Emsley et al., 2010) and refinement of atomic coordinates, isotropic B-factors, and TLS and group-occupancy parameters with Refmac (Murshudov et al., 1997; Winn et al., 2011) and PHENIX, as well as multi-start simulated annealing refinement and real-space coordinate refinement in PHENIX improved the electron density map and allowed the placement of the mRNA. For better interpretability of the electron density peaks during visual inspections, a blurring B-factor was often applied in COOT. Structural alignments and image preparations were done using PyMOL.

2.5.8. Mutant ribosome preparation

Mutant versions for the *E. coli* S3 gene were generated using the Kunkel method (Kunkel et al., 1987) by alanine substitution. Mutant proteins were expressed, purified, and used for in vitro 30S reconstitution and 70S preparation as described (Culver and Noller, 2000). S3-deleted ribosomes were made as control by omitting S3 in the reconstitution mix.

2.5.9. Filter binding assay

Nitrocellulose filter binding assays were typically performed by pre-mixing 2 pmol of wild-type or mutant 70S ribosomes and 5 pmol of fMVVV mRNA (Table 2.3) in buffer containing 20 mM Tris.Cl pH7.0, 100 mM NH_4Cl, 10 mM $MgCl_2$, 6 mM βME, and 0.25 mg/ml bovine serum albumin (i.e. 2.5X BSA) on ice, followed by the addition of serial dilutions (0.6-64 pmol) of ^{35}S-labeled fMet-tRNA^{fMet} in a total volume of 20 μL, and incubation at 37°C for 15 min for P-site binding. After chilling on ice for 5 min, 10 μL of each reaction was blotted on a pre-soaked nitrocellulose HA filter (Millipore), which was then washed three times with a total of 15 mL ice-cold buffer without BSA, dried, and quantified using a scintillation counter. Background filter binding in the absence of ribosome or the 30S subunit were measured as controls. tRNA binding affinities (K_d) were estimated in Origin (OriginLab) by least-squares minimization fitting of the measured counts (*count*) at each total tRNA concentration, [*tRNA*], and total ribosome concentration, [70*S*], to the hyperbolic formula for equilibrium binding,

$$Count = C_{\max} \times \left[([70S]+[tRNA]+K_d)/2 - \sqrt{(([70S]+[tRNA]+K_d)/2)^2 - [70S]\times[tRNA]} \right]$$

, where $C_{\max}$ is the estimated maximum count per unit of ribosome concentration (the product of tRNA specific activity, reaction volume, and binding stoichiometry). In the absence of mRNA, $C_{\max}$ was estimated to be approximately twice as that in the presence of mRNA, implying a binding stoichiometry of ~2 (Table 2.2).

2.5.10. Toeprinting assay

Toeprinting assays were performed essentially as described (Takyar et al., 2005). Typically, 10 pmol of *E. coli* 70S ribosome was incubated in a 10 μL reaction containing 20 pmol of the fMVVV mRNA (Table 2.3) and 20 pmol of fMet-tRNA$^{\text{fMet}}$ in 20 mM Tris.Cl pH7.0, 100 mM NH_4Cl, 10 mM $MgCl_2$, and 6 mM βME at 37˚C for 15 min for P-site binding. For each translocation reaction, 40 pmol of Val-tRNA$^{\text{Val}}$ was incubated with 40 pmol of EF-Tu·GTP at 37˚C for 5 min, and the resulting ternary complex was added along with 30 pmol of EF-G and 2 mM of GTP and 2 mM $MgCl_2$ to a P-site binding reaction and incubated at 37˚C for 10 min to perform translocation. Primer extension was carried out by addition of ~40 fmol of ^{32}P-end-labeled toeprinting oligonucleotide (~100 kcpm radioactivity), 70 µM each dNTP, and 0.3 unit of AMV Reverse Transcriptase, and incubation at 37˚C for 3 min. The mix was then ethanol precipitated, resuspended in 1X urea dye and run on an 8% polyacrylamide toeprinting gel containing 8 M urea. The gel was dried and exposed to a phosphorimager screen overnight for quantification. For mutant reconstituted ribosomes, P-site binding efficiency was measured as the background-corrected intensity of the P-site binding toeprint (which correlated with the translocation toeprint) normalized to that in wild-type reconstituted ribosomes.

2.5.11. Yeast genomic mutagenesis

Double-mutation R116A,R117A in the RPS3 gene in *S. cerevisiae* was introduced via the CRISPR-Cas9 system (DiCarlo et al., 2013) using the gRNA cassette sequence in Table 2.3 and a synthetic 90-nucleotide HR template in which the two AGA codons were replaced by GCT. Mutants were confirmed by colony PCR and sequencing, and the cells were cured of the transformation plasmid by counterselection on 5-FOA plates. A mock mutant with a synonymous codon change for A118 from GCT to GCC was used as a control for off-target effects. Temperature sensitivity tests were performed by comparing colony size, relative to wild-type cells, on YPD plates after growth at 16°C, 30°C, and 40°C for 1-2 days. Cold-sensitivity was also tested by measuring the change in turbidity (OD_{600}) in liquid YPD.

Table 2.1. Crystallographic statistics for the *E. coli* 70S-hairpin complex

Data collection	
Space group	P 2_1 2_1 2_1
Cell dimensions (Å)	211.7 433.9 623.5
Resolution (Å)	60-3.9 (4.0-3.9)
Completeness (%)	99.9% (99.9%)
<I/σI>	3.3 (0.9)
CC1/2	99.6 (26.1)
Redundancy	8.3 (6.2)
Number of unique reflections	499,193 (36,230)
Wilson B factor (Å^2)	119
Refinement	
Resolution (Å)	60 – 3.2*
Number of reflections	898,004
Number of atoms (ASU)	297,898
R_{work}/R_{free} (%)	28.1 / 29.3
R.M.S.D. bond lengths (Å)	0.011
R.M.S.D. bond angles (°)	1.21
Average B-factor (Å^2)	145

*Inclusion of data to 3.2Å resolution in refinements improved the quality of the electron density maps.

Table 2.2. Binding of fMet-tRNA^{fMet} to reconstituted 70S ribosomes

	[Mg^{2+}]	mRNA	Reconstituted Ribosome	Estimated K_d for tRNA binding [a]	Est. tRNA binding stoichiometry [b]
1	10 mM	fMVVV	Wild-type S3	6.7 ± 3.5 nM (*n*=44)	1.0
2			Mutant S3 [c]	360 ± 70 nM (*n*=37)	0.9
3			No S3	680 ± 250 nM (*n*=10)	0.4
4		No mRNA	Wild-type	1000 ± 140 nM (*n*=11)	1.8
5			Mutant S3	1700 nM ± 340 nM (*n*=6)	2.1
6	20 mM	fMVVV	Wild-type	14 ± 7.6 nM (*n*=5)	1.7
7			Mutant S3	85 ± 50 nM (*n*=5)	1.9
8		No mRNA	Wild-type	39 ± 21 nM (*n*=5)	1.8
9			Mutant S3	90 ± 27 nM (*n*=5)	1.8

[a] The standard error of the estimates are indicated. *n* denotes the number of data points.

[b] Stoichiometry is estimated as saturating bound ribosome fraction relative to that in row 1.

[c] Mutant S3 refers to the triple mutant (R130A,R131A,K134A).

Table 2.3. Nucleic acid sequences used in this study

Name (type)	Use	Sequence[a]
pH03H9 (mRNA)	Crystallization (Harpin complex)	GAAAGGAAAUAAAAAUGGUAGUAGUAGAUAACCGCUUCGGCGGAU
fMVVV (mRNA)	Toeprinting assay, filter binding assay	GAAAGGAAAUAAAAAUGGUAGUAGUAGAUAGAAAAUAAUAGAAGAAUCGGAUAAGAGAACACAGGAUCCAG
TP2 (DNA oligonucleotide)	Toeprinting assay	CTGGATCCTGTGTTCTC
gRNA cassette (dsDNA block)	Yeast CRISPR mutagenesis	GCTATCAGAAGAGCTGCTTA

[a] Important features in each sequence are underlined.

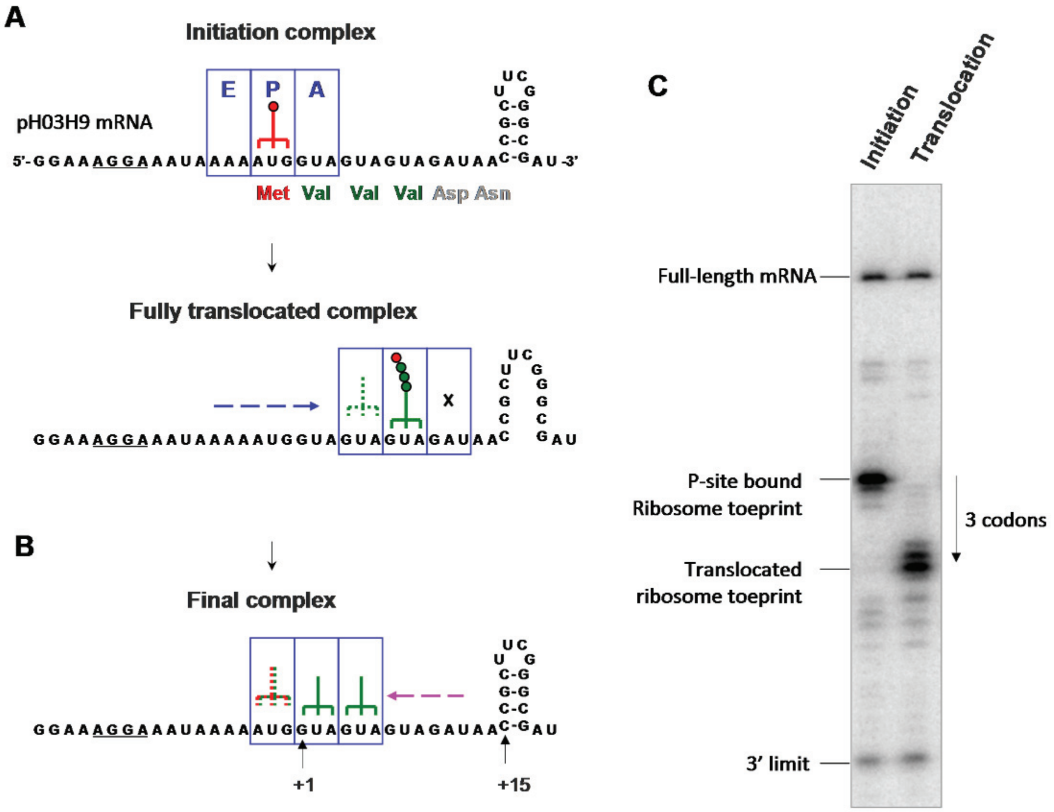

Figure 2.1 Indirect approach for hairpin complex formation. *A*. Binding of the ribosome (blue box) and initiator tRNA (red) on the mRNA at the AUG codon, followed by three catalyzed translocation steps to reach the last valine codon. *B*. Relocation of the ribosome back to the first valine codon, as suggested by the crystal structure. *C*. Confirmation of successful translocation with a control mRNA (fMVVV, Table 2.3) by toeprinting.

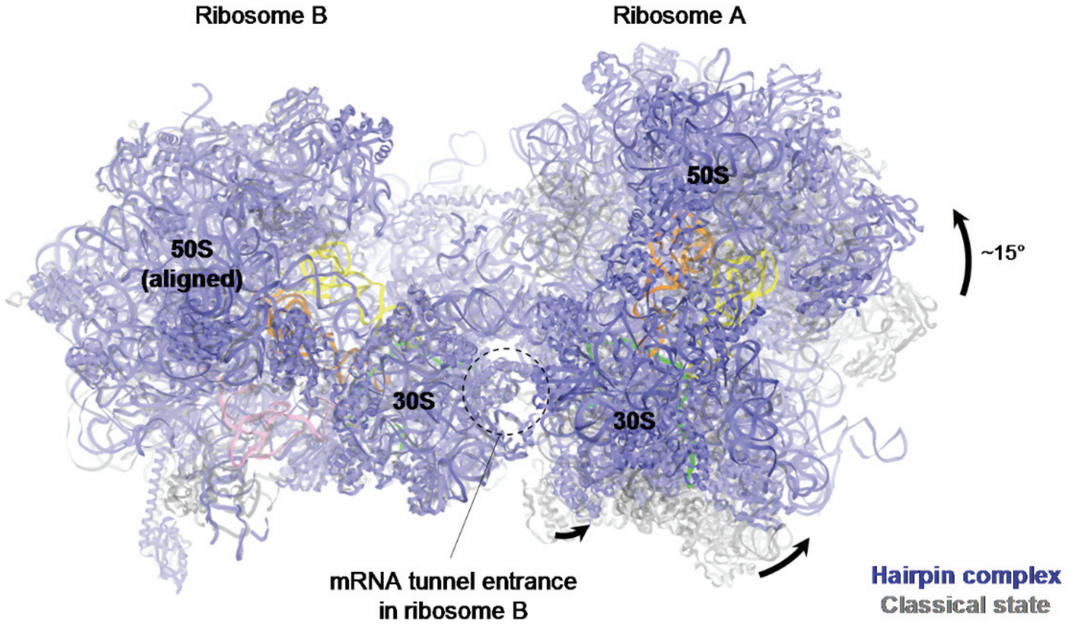

Figure 2.2. Crystal packing rearragement in the presence of mRNA hairpin. The large-scale rigid-body movement of the 70S ribosomes in the crystal lattice of the hairpin complex (blue), relative to a *T. thermophilus* classical-state complex (gray, PDB 4v51) (Selmer et al., 2006). The movement significantly opens up the space in front of the tunnel entrance for ribosome B (dashed circle).

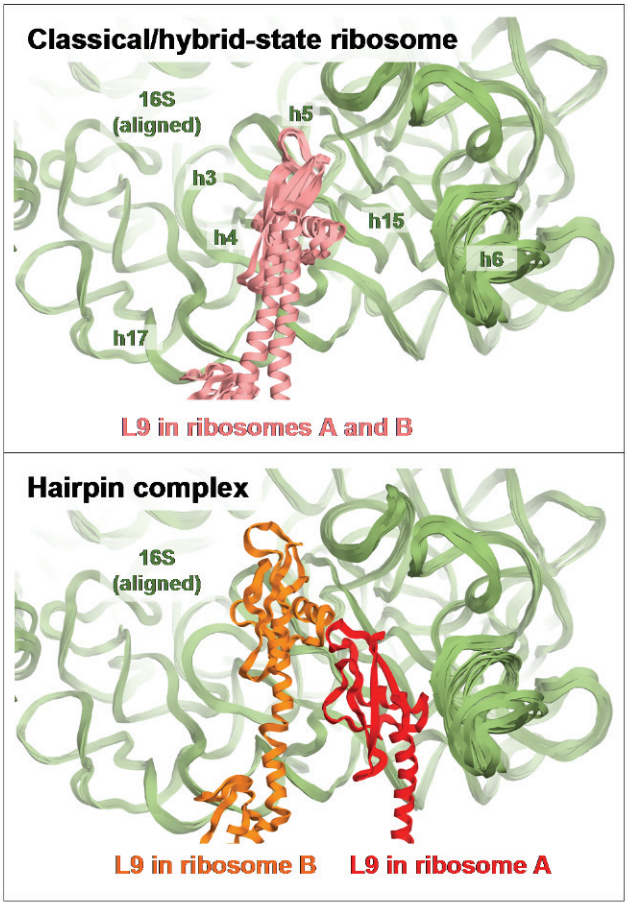

Figure 2.3. Crystal contacts mediated by ribosomal protein L9. In the classical arrangement (*top*, PDB 4v9d) (Dunkle et al., 2011), the contacts between protein L9 (pink) of one ribosome and 16S rRNA (green) in the neighboring ribosome is the same for ribosomes A and B, as seen in the overlay after alignment of the 16S rRNA from the two ribosomes. In the hairpin complex (*bottom*), both L9 contacts are significantly rearranged, and are different in the two ribosomes (red and orange).

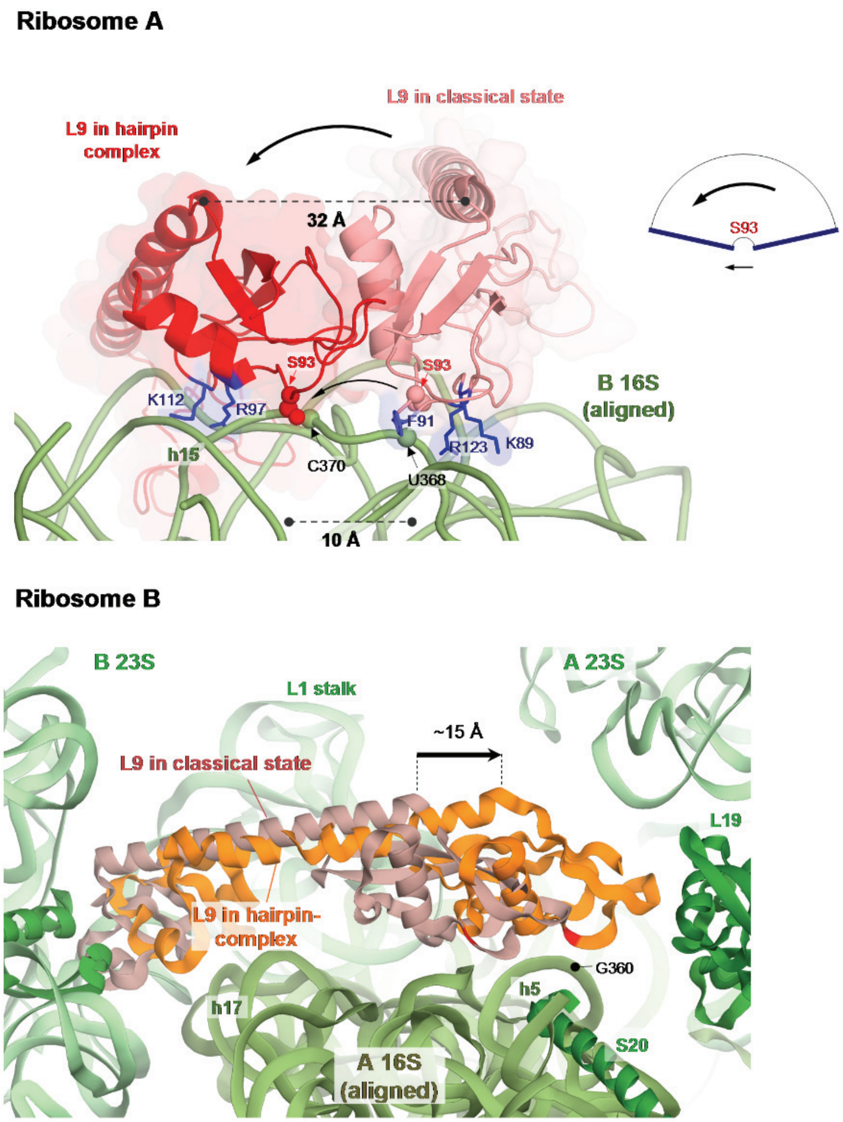

Figure 2.4. Repositioning of ribosomal protein L9 in the presence of mRNA hairpin. *Top*. The L9 protein in ribosome A (red) is shifted from its classical position (pink, PDB 4v9d (Dunkle et al., 2011), and in all crystal structures of the same space group) by about 30 Å at its α-helical joint, forming a new binding interface on the opposite side of serine 93 on helix h15 of 16S rRNA, involving Arg97 and Lys112. In turn, most of the classical interface which involved Lys89 and Arg123 is now lost. The two L9 conformations are related by a sliding pivot motion, as indicated. *Bottom*. The L9 protein in ribosome B (orange) is moved further toward the body of the neighboring 16S rRNA compared to the classical position (salmon).

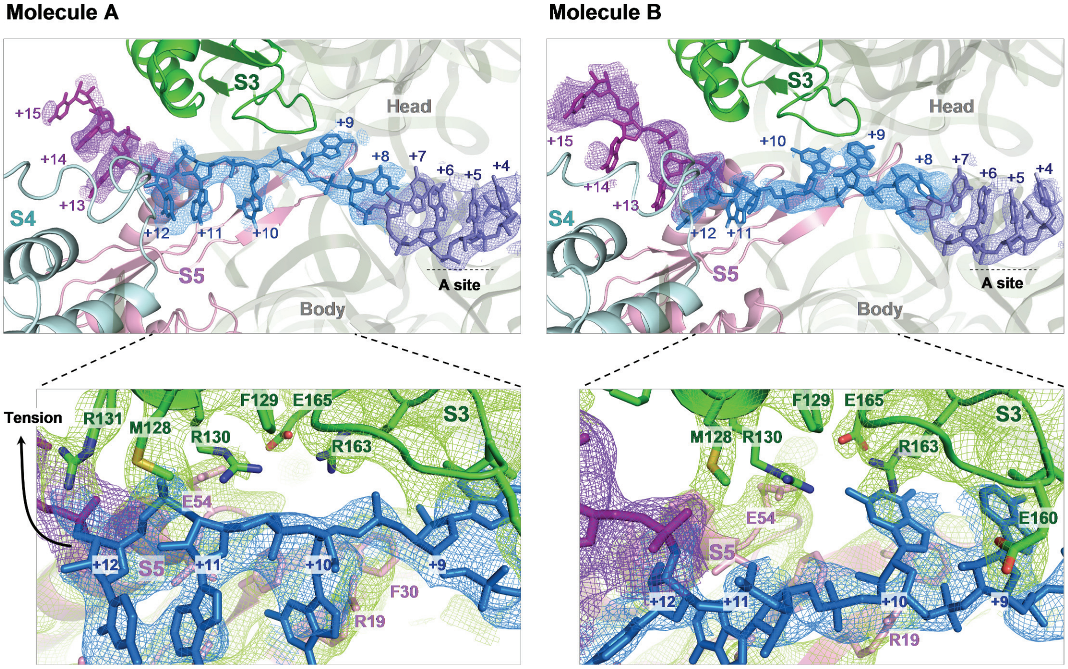

Figure 2.5. Path of the mRNA in the downstream tunnel for ribosomes A and B. The electron density for the mRNA is shown at contour levels +1.5σ (for region +4 to +7), 0.8 σ (for region +8 to +12), and 0.5σ (for region +13 to +15) as indicated with different colors. Arginine 131 and 164 in S3 (green) can interact with the mRNA backbone in ribosome A, and with the nitrogenous base (a guanine) in ribosome B. Conversely, arginine 19 in S5 (pink) is in position to stack on the guanine in ribosome A, but approaches the backbone in ribosome B.

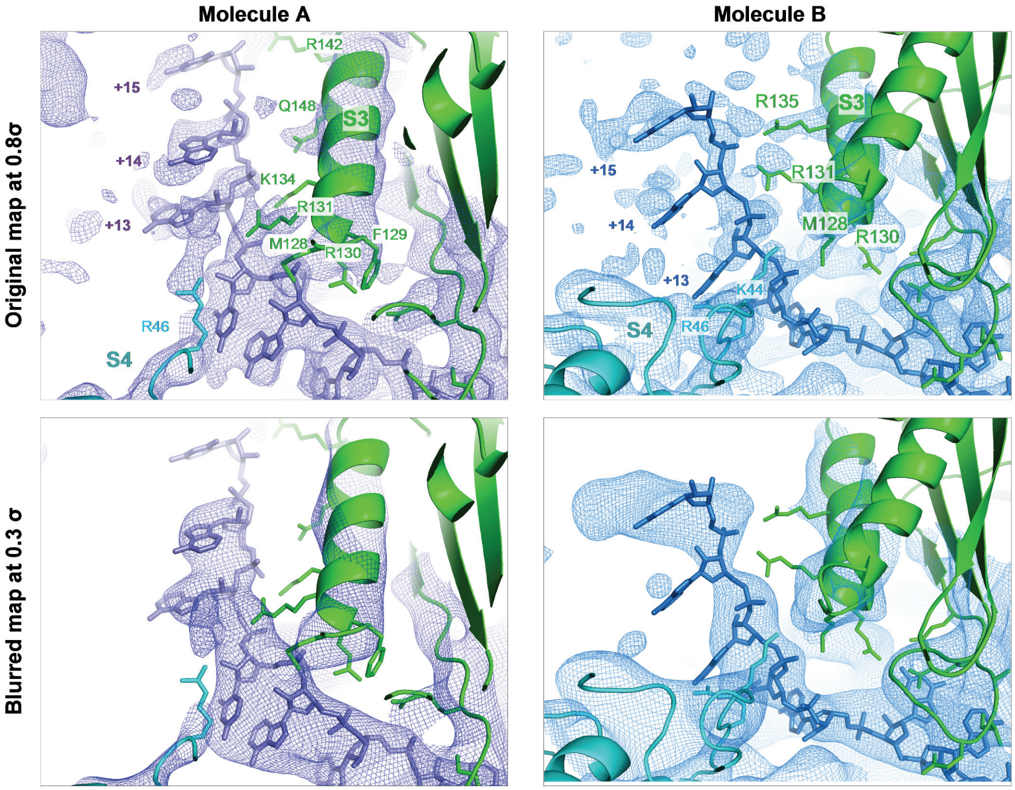

Figure 2.6. The flexible interaction between mRNA and ribosomal protein S3 outside of the downstream tunnel entrance. As shown in the top two snapshots, the electron density outside of the tunnel is weak compared to the background noise for the mRNA but not the protein. In the bottom images, blurred maps (by 200 Å^2) are used to identify the overall orientation of the mRNA chain. The combination of the two maps allows for the identification of protein residues in S3 that are in position to contact the mRNA backbone, as indicated in the top images.

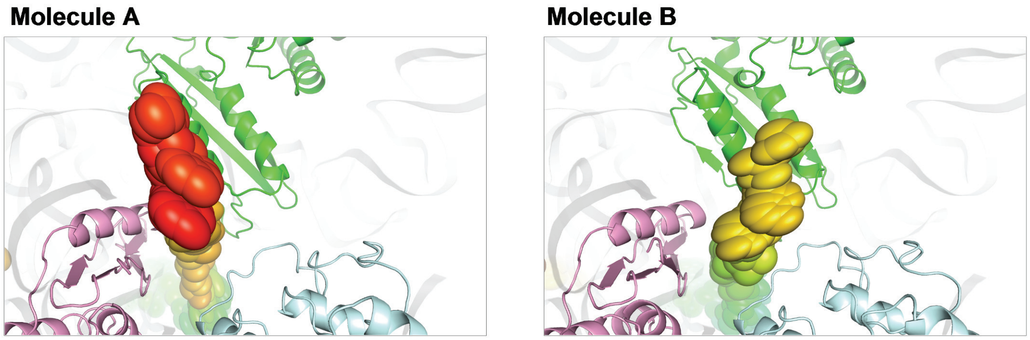

Figure 2.7. Anisotropic displacement of S3-bound mRNA. The anisotropic displacement ellipsoids for the mRNA outside of the tunnel (solvent view) in the two ribosome molecules is shown. Red color indicates a higher overall B-factor. Proteins S3, S4, and S5 are in green, light blue, and pink, respectively.

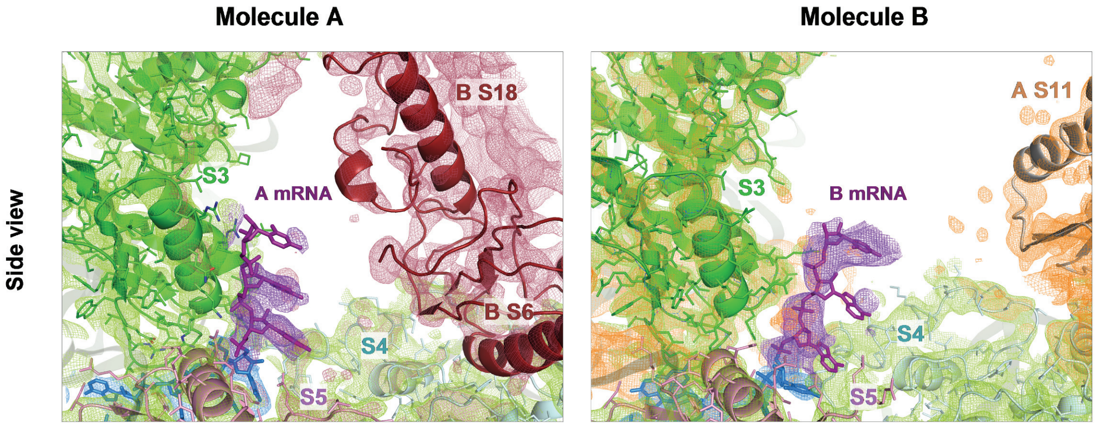

Figure 2.8. Crowding outside of the tunnel in ribosomes A and B. Proteins S6 and S18 (red) from the symmetry mate approach the tunnel entrance in ribosome A, whereas the space in front of the entrance in ribosome B is less crowded. Also see Fig. 2.9 for a top view.

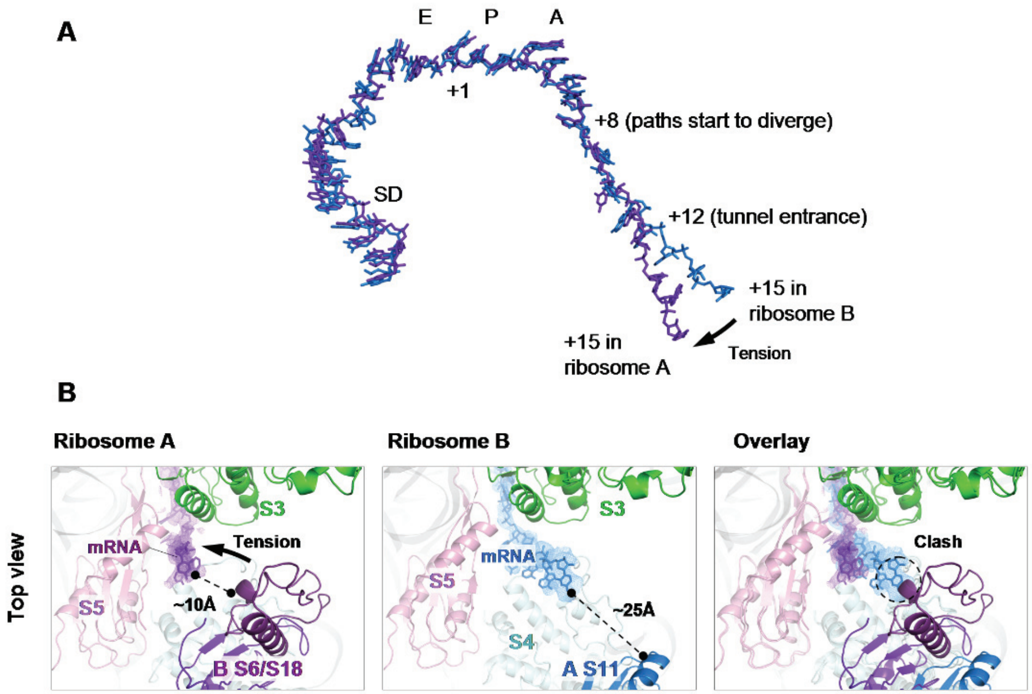

Figure 2.9. The path of the mRNA in ribosomes A and B. *A*. Despite overall similarity, the path of the mRNA in ribosome A starts to diverge from that in B as early as position +8. Inferred tension due to crowding at the tunnel entrance is indicated by an arrow. *B*. Top view of the mRNA outside of the tunnel showing the comparison between the crystal contacts near the tunnel entrance in ribosomes A and B. The overlay on the right shows the steric clash with S6/S18 in the neighboring ribosome if the mRNA in ribosome A was at the same location as that in ribosome B.

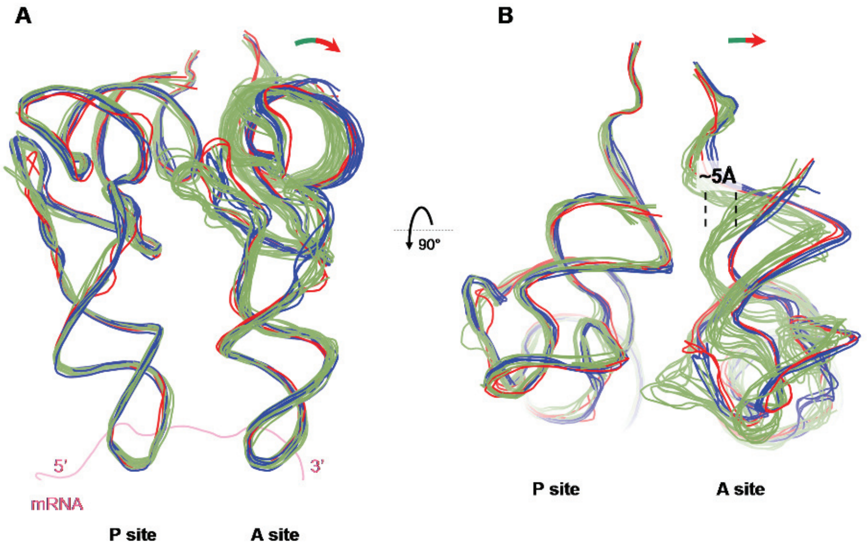

Figure 2.10. Conformation of A-site tRNA in the *E. coli* hairpin complex. Backbone traces of A- and P-site tRNAs in the *E. coli* hairpin complex (this work, red), *T. thermophilus* complexes with peptide antibiotics viomycin or capreomycin (blue, PDB 4v7l and 4v7m) (Stanley et al., 2010), and *T. thermophilus* complexes with paromomycin or no antibiotic (green, PDB 4v5c, 4v5d, 4v6f, 4wt1, 5ibb, 5e7k, and 5ib7) (Jenner et al., 2010; Rozov et al., 2015, 2016a, 2016b; Voorhees et al., 2009), after alignment of all structures with respect to the 23S rRNA. Two ribosome molecules (A and B) are represented for each complex. *A*. View from the subunit interface (large subunit is at the top) shows that the A-site tRNA in the first two categories (red and blue) is bent such that its acceptor and T arms are further away from the those of the P-site tRNA. Note that the P-site tRNA is superimposable in all of the complexes. *B*. Top view (from the large subunit) shows that the A-site tRNA backbone in the first two categories (red and blue) follows a distinct path that widens the gap between the A- and P-site tRNAs by ~5Å in the acceptor arm region.

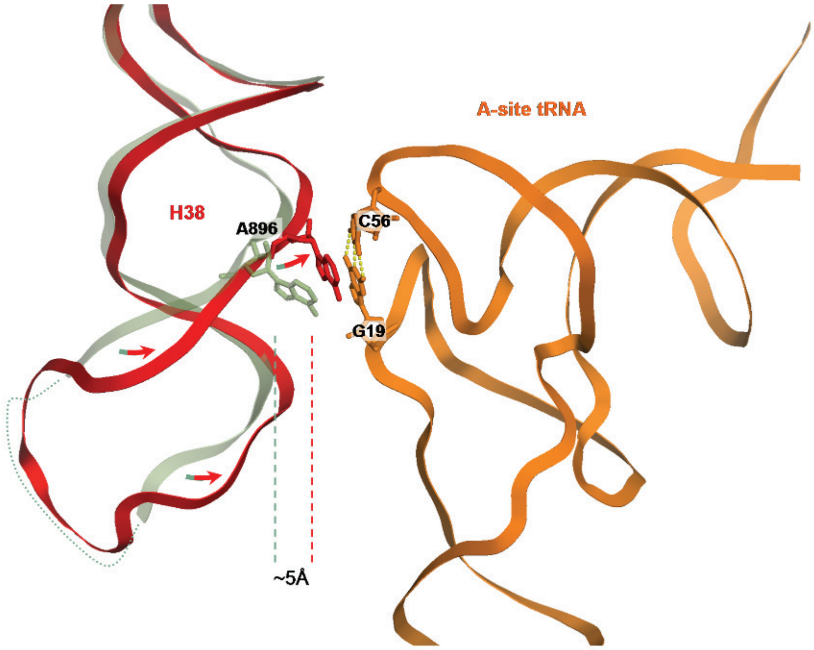

Figure 2.11. A-site finger movement in the presence of cognate tRNA. In the presence of A-site tRNA (orange), the tip of helix H38 of 23S rRNA (red) interacts with the tRNA elbow, moving by up to 5 Å toward it compared to when the A site is vacant (faint green, from PDB 4ybb) (Noeske et al., 2015). The A896 base of 23S rRNA stacks on the conserved tertiary base pair in the A-site tRNA formed between C56 and G19 from the T- and D-loops, respectively. Note that the H38 terminal loop is not resolved in the vacant complex.

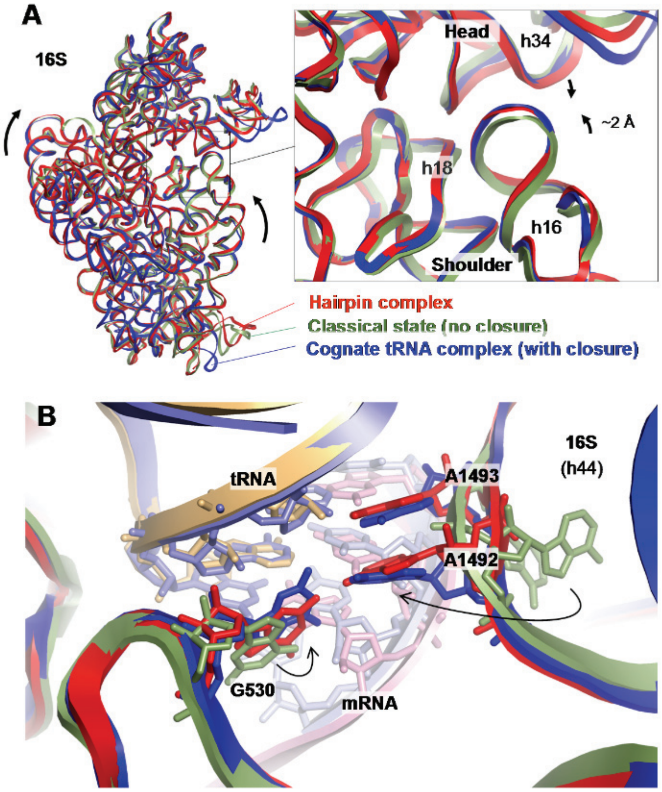

Figure 2.12. Closure of the small subunit in the presence cognate A-site tRNA. *A*. The slight approach of the shoulder toward the head in the *E. coli* 70S hairpin complex structure (red) and the *T. thermophilus* 30S subunit bound to ASL (PDB 1ibl) (Ogle et al., 2001), compared to an *E. coli* 70S complex with no tRNA (PDB 4v9d) (Dunkle et al., 2011) which was used as our original molecular replacement search model. *B*. Interactions at the decoding site in the 16S rRNA (colored as in part A) showing the flipping of the 16S nucleotides A1492 and A1493 toward the tRNA-mRNA base pairs, and flipping of the G530 base into the *anti* conformation.

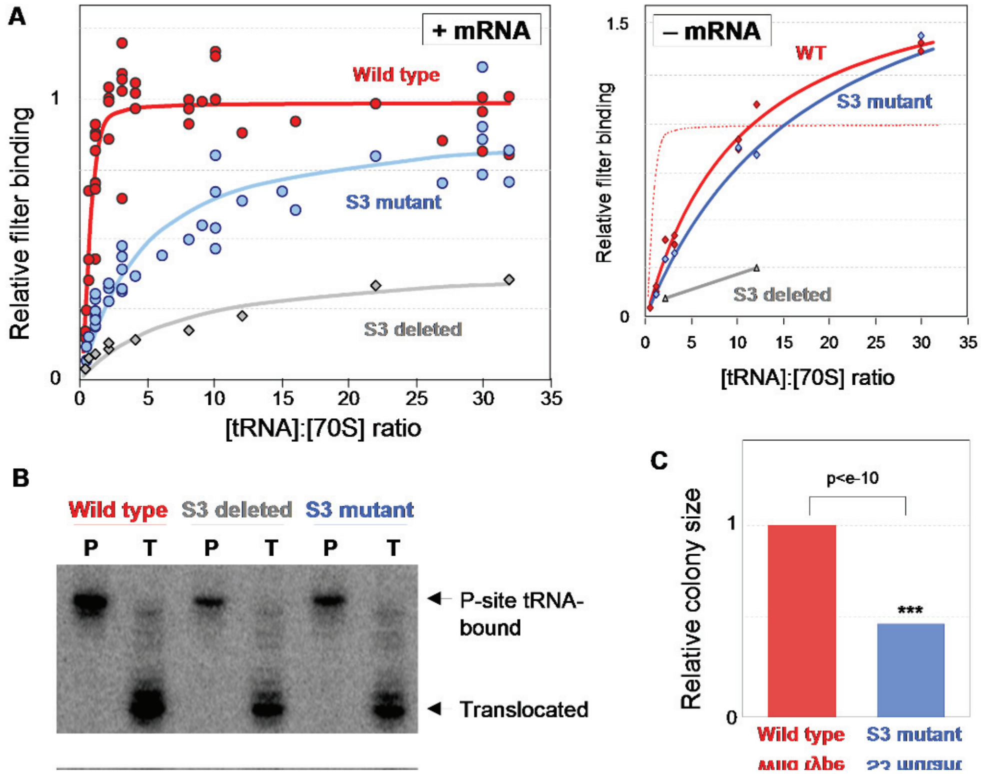

Figure 2.13. Mutational analysis of S3 residues near the mRNA tunnel entrance. *A*. Binding of ^{35}S-labeled fMet-tRNA$^{\text{fMet}}$ to reconstituted *E. coli* ribosomes containing wild-type S3 (red), mutant S3 (blue), or no S3 (gray), in the presence of fMVVV mRNA (left graph), or without mRNA (right graph), measured by filter binding. The red curve in the left graph is redrawn as the dotted curve in the right graph for comparison. *B*. P-site binding (P) and translocation (T) toeprints of reconstituted ribosomes containing wild-type S3, no S3, or mutant S3, programmed with the fMVVV mRNA. *C*. Relative colony size of *S. cerevisiae* strains with wild-type or mutant S3 after growth at 16°C.

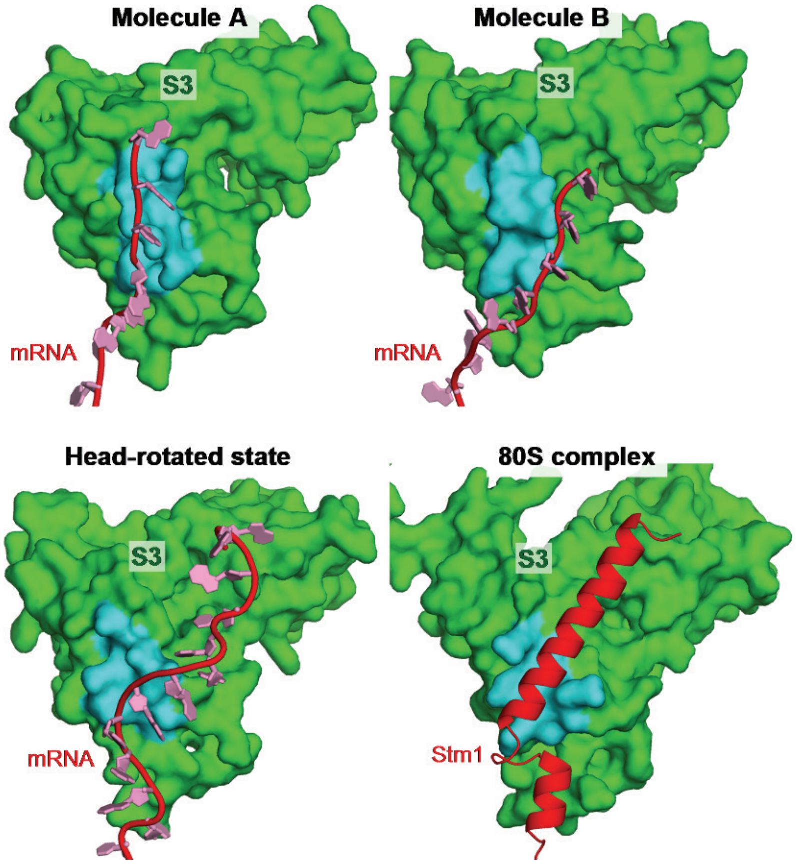

Figure 2.14. The S3 interface for mRNA binding. Solvent view of the interaction of the ribosomal protein S3 (green) outside of the tunnel entrance. The arginine-rich α-helix in S3 forms a binding interface (cyan) for RNA binding. *Top*. The path of the mRNA observed in molecules A and B in this study. *Bottom*. The path of the mRNA observed in a chimeric-hybrid translocation intermediate (PDB 4w29, *left*) (Zhou et al., 2014) and the binding of Stm1 in the yeast 80S complex (PDB 4v88, *right*) (Ben-Shem et al., 2011).

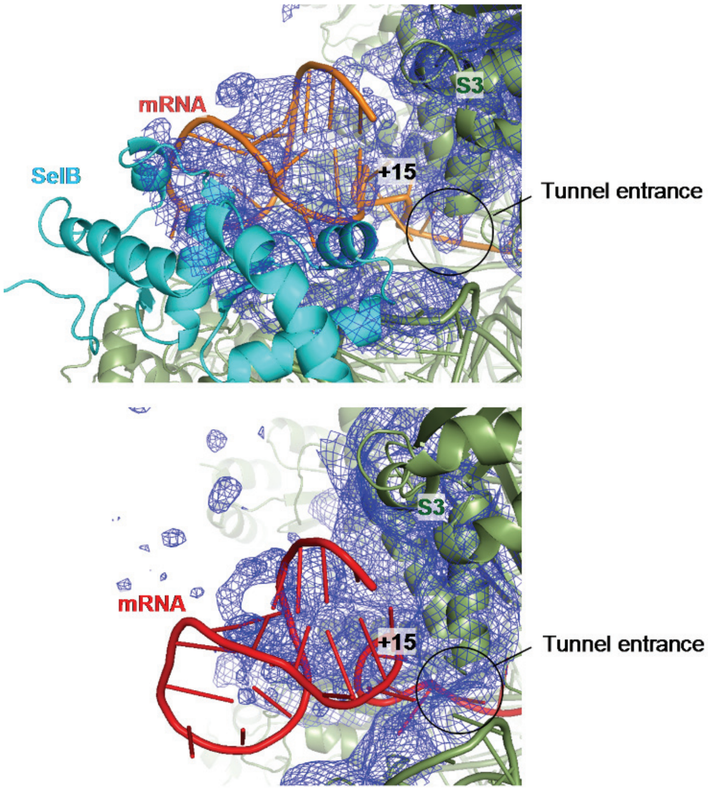

Figure 2.15. Binding of a SECIS hairpin to ribosomal protein S3. Interaction of the ribosomal protein S3 with a SECIS hairpin is seen in cryo-EM maps (Fischer et al., 2016) that have been blurred for better interpretability. *Top*. In the presence of SelB, the hairpin density is well resolved and the hairpin interacts at its base with protein S3 beyond the tunnel entrance. *Bottom*. In the absence of SelB, the density for the base of the hairpin is similarly localized, although the rest of the hairpin is less ordered, indicating an anchorage on S3 at the base of the hairpin but an otherwise freedom of movement.

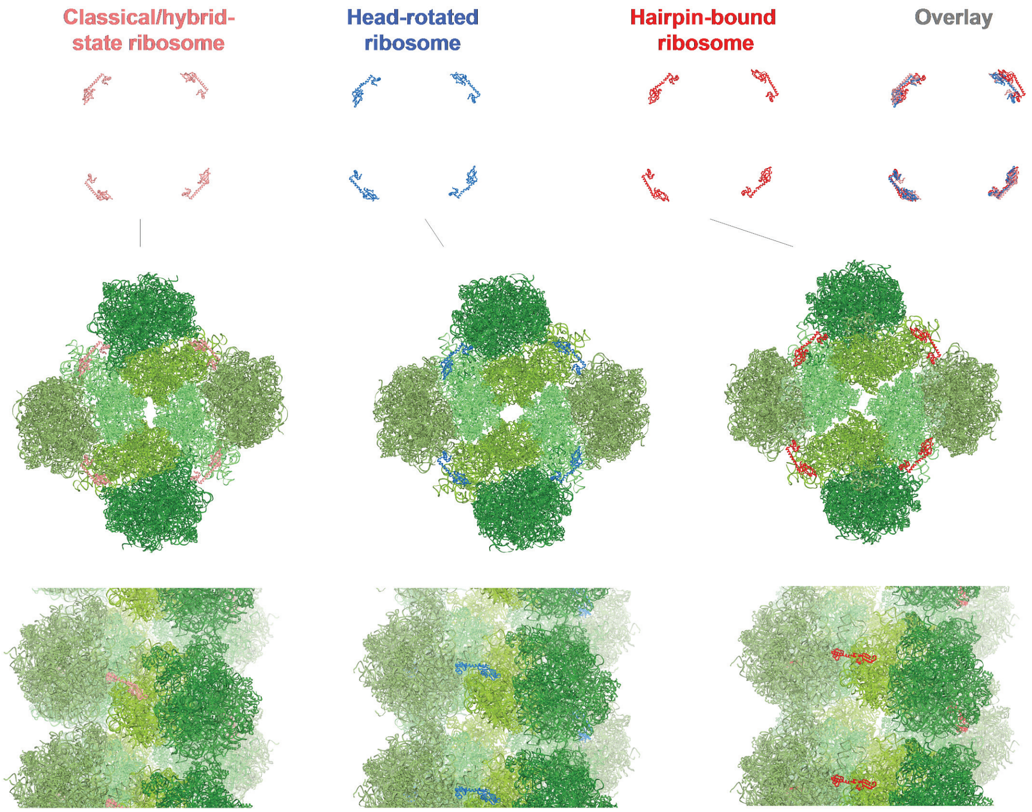

Figure 2.16. The polysome profile in the presence of mRNA hairpin. Comparison between the polysome profiles predicted from the crystal structures of the classical/hybrid-states ribosome (PDB 4v9d) (Dunkle et al., 2011), head-rotated ribosome with kasugamycin (PDB 4v4h) (Schuwirth et al., 2006), and our hairpin complex. *Top*. The position of the L9 protein in the polysome helical arrays as viewed from the top, showing a skewed arrangement in the hairpin complex. *Bottom*. The top and side views of the polysome spirals for each of the structures, showing changes in the relative orientation of the neighboring ribosomes, including an opening of space in front of the helicase actives sites in the hairpin structure (seen as an X-shaped "crack" in the top view). The small and large subunits of the A and B molecules are in different shades of green.

Chapter 3. A Tandem Active Site Model for the Ribosomal Helicase

3.1. Abstract

During protein synthesis, the mRNA helicase activity of the ribosome ensures that codons are made single-stranded before decoding. Force spectroscopy analysis has revealed that unlike all other examined nucleic acid helicases, the ribosome uses two distinct active unwinding mechanisms. What these mechanisms are and how they are coupled to conformational changes in the ribosome during translocation are not fully understood. Based on recent structural data, a quantitative model is presented for the ribosomal helicase that involves a distal and a proximal active site acting in tandem on the mRNA three nucleotides apart from each other. At the distal active site, spontaneous duplex unwinding is followed by sliding of single-stranded mRNA over ribosomal protein S3 during translocation. Stable mRNA structures can bypass this active site in a stick-slip manner and reach the proximal active site. At the proximal active site, spontaneous unwinding is favored by coupling to binding of single-stranded mRNA to S3 and occurs before or during translocation. The proximal active site cannot be bypassed. Our model explains both active mechanisms proposed for the ribosomal helicase, and provides a testable framework to further study mRNA unwinding by this helicase.

3.2. Introduction

The ribosome is an mRNA helicase (Takyar et al., 2005) with no homology to previously known nucleic acid helicase superfamilies (Caruthers and McKay, 2002).

Its helicase active site has been localized to the vicinity of the entrance to the downstream mRNA tunnel between the head and body domains of the small (30S) ribosomal subunit (Qu et al., 2011; Takyar et al., 2005; Yusupova et al., 2001). The entrance is lined by ribosomal protein S3 from the head domain and ribosomal proteins S4 and S5 from the body domain (Fig. 3.1A). Mutation of S3 and S4 residues surrounding the tunnel entrance diminish the activity of the helicase (Takyar et al., 2005), implicating these proteins in its mechanism of action. Rotation of the 30S head domain, which is coupled to mRNA translocation (Guo and Noller, 2012; Ratje et al., 2010; Zhou et al., 2013), changes the shape of the entrance and may contribute to mRNA unwinding (Yusupova et al., 2001).

The ribosomal helicase shows a unique behavior in response to applied external forces (Qu et al., 2011). Duplex destabilization outside of the active site is a known mechanism for “active” helicases, but the parameters of the commonly-used model for these helicases (Betterton and Jülicher, 2005), despite a high degree of redundancy (Manosas et al., 2010), cannot fit the data obtained for the ribosomal helicase using optical tweezers (Qu et al., 2011). A parsimonious model was proposed (Qu et al., 2011) to explain those data, invoking a classical active unwinding through duplex destabilization found in other helicases, plus a second active mechanism with a force-independent rate constant that depends on base pair stability at the junction, apparently unique to the ribosome. The structural basis for such a mechanism was not clear.

Our crystallographic results (Chapter 2) show binding of single-stranded mRNA to the arginine-rich α-helix spanning residues 130-142 of ribosomal protein S3 just outside of the tunnel entrance in the *E. coli* ribosome. In the structure (Fig. 3.1), the mRNA bends at the tunnel entrance to allow the binding of its three downstream nucleotides to the S3 α-helix. The backbone of the bound mRNA is extended and straightened along the binding interface, deviating from ideal A-form geometry (Fig. 3.1B). This deviation creates a preference for single-stranded mRNA binding to this site, as it is not possible for double-stranded RNA to adopt this configuration (see section 3.5.1). Binding of single-stranded mRNA to this same site on S3 was also observed recently in *T. thermophilus* ribosomes trapped in a translocation intermediate state (Zhou et al., 2014).

Based on this structural observation, we propose a model for the ribosomal helicase that involves two tandem "active sites" where mRNA unwinding can occur (Fig. 3.2). mRNA structures are first encountered at the "distal" active site, and if not unwound at this site in time, are relegated to the "proximal" active site. If we define the first nucleotide of the P-site codon as position +1 on the mRNA, the proximal and distal active sites are at positions +11 and +14, respectively. The proximal active site corresponds to the tunnel entrance (Chapter 2; Jenner et al., 2010), precisely matching the position of a helicase active site localized by biochemical analysis (Takyar et al., 2005). The distal active site is at the distal end of the bound mRNA outside of the tunnel (Chapter 2). Additionally, we refer to the mRNA segments acted upon by the proximal and distal active sites as the *proximal segment* (positions +12 to +14) and the *distal segment* (+15 to +17), respectively.

Preferential binding of single-stranded mRNA of the proximal segment to ribosomal protein S3, as seen in the structure, would stabilize the single-stranded conformation of mRNA in this segment, and therefore destabilize roadblocks caused by complementary base pairing, tertiary folding, or binding to other proteins. This mode of unwinding resembles that of the DEAD-box family of RNA helicases (Cordin et al., 2006; Jarmoskaite and Russell, 2011; Linder and Jankowsky, 2011; Sengoku et al., 2006), which bind single-stranded RNA with high affinity, and can therefore unwind RNA passively by simply competing with other binding partners (including the complementary strand). Importantly, we propose that the release of the bound strand after unwinding, which in DEAD box helicases is triggered by ATP hydrolysis, occurs in the case of the ribosome by the movement of S3 relative to its bound mRNA during translocation. This would most likely happen during the step of translocation when the head domain of the small subunit, which includes S3, undergoes reverse rotation from the chimeric hybrid state to the classical state (Guo and Noller, 2012; Ratje et al., 2010), pulling S3 away from its bound mRNA segment toward the 3’ end of the mRNA by three nucleotides (one codon).

At the distal active site, this movement can proceed via either “sliding” or “bypass” (Fig. 3.2A). During sliding of S3 along single-stranded mRNA, loss of mRNA binding at one end of its contact surface is simultaneous with the gain of compensatory binding at the other end, resulting in no net gain or loss of binding interactions after sliding. Such isoenergetic sliding transitions can be very fast, best described as a one-dimensional diffusion process, as proposed for DNA binding proteins such as RNA polymerases and sliding clamps (Barsky et al., 2010; von Hippel and Berg, 1989; Jeltsch and Urbanke, 2004). Sliding of S3 over its bound single-stranded mRNA is fast as long as the distal segment of mRNA is also single-stranded and able to form compensatory interactions rapidly. If the distal segment remains double-stranded, sliding will be slowed down by the rate of duplex opening, and movement of S3 relative to the mRNA may instead occur mainly by *uncompensated disruption* of the existing S3-single-stranded-mRNA binding in the proximal segment. This would allow the duplex to "bypass" the distal active site and be pulled to the proximal active site without unwinding. A simplified animation for this model is provided in Supp. File 3, showing what is essentially a "stick-slip" phenomenon, as elaborated further in the Discussion. Bypass is unique to the distal active site. With a duplex at the proximal active site, translocation proceeds only if the duplex spontaneously opens, and no "bypass" is possible for this site (Fig. 3.2B).

Based on this model, we describe a simple kinetic scheme that explains the observed force-dependent rates of ribosomal translocation over mRNA duplexes, and accounts for both of the proposed active unwinding mechanisms for this helicase (Qu et al., 2011).

3.3. The Kinetic Scheme for the Tandem Active Site Model

We start by considering the *proximal* segment of mRNA, just outside of the tunnel, in three distinct microstates in the Gibbs ensemble (Fig. 3.3A):

(1) free single-stranded form (*proximal-open*)
(2) double-stranded form or duplex (*proximal-closed*)
(3) S3-bound single-stranded form (*proximal-bound*)

The first two states are typically considered in helicase models, while the third, *bound*, state is introduced here based on our structural findings. Unwinding at the proximal active site is simply the spontaneous conversion of the *proximal-closed* state to one of the other two states by equilibrium during or between translocation steps. The Boltzmann factors for the partition function describing these states in the presence of force F are chosen as:

proximal-open: $\exp(m[FX_F - \Delta G_{stretch}])$ (3.1.1)

proximal-closed: $\exp(m\Delta G_{bp})$ (3.1.2)

proximal-bound: $\exp(m\Delta G_{binding})$ (3.1.3)

Here, m is the length of the mRNA segment that can bind to S3 (i.e. the proximal segment). In our crystal structure (Chapter 2), three nucleotides are seen to bind to S3 outside of the tunnel; therefore, $m = 3$. We assume that binding to S3 in this segment occurs in an all-or-none fashion, meaning there is only one rate-limiting step for binding of the entire segment (see section 3.5.1). This cooperative binding, combined with the codon size (3 nt) would help explain the observed kinetic step size (δ) of 3 bp in tweezers experiments (Qu et al., 2011).

F is the applied external pulling force (e.g. by optical tweezers), and X_F is the extension of single-stranded RNA at each applied force F according to the worm-like chain (WLC) model (Petrosyan, 2017; Tinoco, 2004; Tinoco and Bustamante, 2002). Additionally, the product FX_F is normalized to units of k_BT, where k_B is the Boltzmann constant and T is temperature. Similarly, $\Delta G_{stretch}$ (stability of non-stretched single-stranded mRNA per opened base pair in the WLC model (Tinoco and Bustamante, 2002)), ΔG_{bp} (average base pair stability at zero force), and $\Delta G_{binding}$ (average mRNA-S3 binding stability per nucleotide at zero force) are all positive and in units of k_BT (see section 3.5.2).

During each translocation step, the three nucleotides of the distal segment replace the proximal segment. Of course, when still outside of the proximal segment, these nucleotides can only be in the *open* or the *closed* state (Fig. 3.3B). Unwinding at the distal active site is simply the spontaneous conversion of the *distal-closed* state to the *distal-open* state, which is reversible until translcation occurs. The Boltzmann factors for the distal segment are:

distal-open: $\exp(s[FX_F - \Delta G_{stretch}])$ (3.2.1)

distal-closed: $\exp(s\Delta G_{bp})$ (3.2.2) where $s = 3$ is the translocation step size for the ribosome dictated by codon size, and the other variables are as described above.

In the following equations, probabilities are calculated using the above partition functions with pre-equilibrium assumption. For simplicity, we describe unwinding of a repetitive mRNA sequence with uniform stability; i.e., every translocation step encounters mRNA of the same stability as all the other steps.

The kinetic scheme has 3 free parameters, one fewer than the model proposed previously (Qu et al., 2011). The parameters are (1) $\Delta G_{binding}$ described above, (2) k_{off}^{S3}, the dissociation rate constant for mRNA-S3 binding at zero force, which is related to $\Delta G_{binding}$, and (3) k_{dwell}, apparent rate constant that combines all stages of an elongation cycle not involved in mRNA unwinding at the helicase sites, e.g. tRNA accommodation, peptide bond formation, and subunit rotation.

The kinetic scheme is shown in Fig. 3.4. Of course, the *proximal-closed* state (i.e., a closed junction at the proximal active site) cannot proceed to translocation without spontaneously unwinding first, and translocation can only take place starting from the *proximal-bound* or the *proximal-open* states in the pre-translocation ribosome. For simplicity, we neglect translocation over the *proximal-open* state, as its inclusion is inconsequential in our examination of the force spectroscopy data (Qu et al., 2011) due to the dominance of the other two states under normal conditions (see section 3.5.3).

Starting from the *proximal-bound* pre-translocation state (Fig. 3.5A), the forward rotation of the head domain of the small subunit (which contains S3) during translocation simply moves both S3 and its bound mRNA together, and no unwinding occurs at the distal active site at this step (Fig. 3.5B). In the reverse rotation, however, the head moves relative to the mRNA. This can result in mRNA translocation by two alternative routes at the distal active site, sliding or bypass, with two distinct outcomes immediately after a translocation event. (Fig. 3.5C,D, also see Supp. File 3)

The “sliding” route involves spontaneous unwinding of the distal segment and its sliding along the S3-mRNA binding interface. Sliding of two interacting surfaces proceeds rapidly if the surfaces interact favorably throughout sliding, such that the transition state is stabilized by almost as much interaction energy as the initial and final states, creating a smooth energy landscape for the transition. In the case of the sliding of S3 along single-stranded mRNA, the net rate of the sliding route (k_{slide}) will be limited by the rate at which the distal segment of mRNA can form new binding interactions at the distal active site (k_{bind}), which in turn depends on whether this segment is in the *open* or *closed* state; once this compensatory binding takes place, the rest of the sliding process, which involves isoenergetic transitions over the bound single-stranded mRNA ($k_{diffuse}$), occurs relatively fast. With k_{bind} as the rate-limiting step, we have:

$$k_{slide}(F) \approx k_{bind}(F) \qquad (3.3)$$

To approximate $k_{bind}(F)$, we consider a relatively rapid equilibrium between the *distal-open* and *distal-closed* states in solution. For structures other than simple duplexes, such as pseudoknots, the individual force-dependent opening rate constants for the first three nucleotides in the structure should be used to account for the kinetic stability of the structure. Taking the equilibrium approximation, the apparent rate constant k_{bind} at each force F is estimated as:

$$k_{bind}(F) = P_{distal\text{-}open}(F)\, k_{on}^{S3} \tag{3.4}$$

where $P_{distal\text{-}open}(F)$ is the probability for the distal segment to be in the *open* state at force F, and k_{on}^{S3} is the association rate constant for S3 binding at zero force:

$$k_{on}^{S3} = k_{off}^{S3} \exp(\Delta G_{binding}) \tag{3.5}$$

The “bypass” route is the uncompensated disruption of single-stranded mRNA binding to S3 by the reverse head rotation. Unlike sliding, it strips S3 of its bound nucleotides and so is not isoenergetic. Disruption occurs along the S3-mRNA interface at a slow constant rate (k_{off}^{S3}) during reverse head rotation regardless of whether the distal segment is in the *open* or *closed* state. However, if the downstream mRNA is mostly in the *distal-open* state, the sliding route described above is much faster in comparison, and the constant slow rate of uncompensated disruption is negligible. In contrast, if the *distal-closed* state is more probable (due to a stable duplex), the sliding route can become so slow that the uncompensated disruption becomes a significant alternative. The disruption allows the distal segment to bypass the distal active site and approach the proximal active site without unwinding. This route exists because such a bypass for a duplex is sterically allowed past the distal active site. As mentioned earlier, the rate of the bypass route (k_{bypass}) is:

$$k_{bypass} = k_{off}^{S3} \tag{3.6}$$

The force-independence of the rate constants k_{on}^{S3} and k_{off}^{S3} used in Eqs. 3.4–3.6 is discussed in section 3.5.4. Briefly stated, the paths for the irreversible "binding" and "disruption" steps, in the sliding and bypass routes, respectively, are not the same as the paths for association and dissociation at equilibrium (which is force-dependent), and proceed via different transition states.

Combining the two routes, the net translocation rate is (Fig. 3.4):

$$k_{translocation} = P_{proximal\text{-}bound}(F)\ (k_{slide}(F) + k_{bypass}) \tag{3.7}$$

where $P_{proximal\text{-}bound}(F)$ is the probability for the proximal segment to be in the *bound* state at force F. The overall translation rate on mRNA, including the non-translocation steps will be:

$$k_{overall} = (k_{dwell}\, k_{translocation}) / (k_{dwell} + k_{translocation}) \tag{3.8}$$

Using the published rates of translation measured under different applied optical tweezers pulling forces (Qu et al., 2011), we estimated the values of the three parameters in the kinetic scheme (Table 3.1). Using these parameter values, the translation rates as a function of the applied force calculated from Eq. 3.8 are in excellent agreement with the experimental measurements made on mRNA hairpin structures (Fig. 3.6). This includes measurements for mRNA hairpins of either 50% or 100% GC content, which only differ in the their value of ΔG_{bp} (estimated using nearest neighbor rules (Xia et al., 1998)) in our kinetic scheme. The existence of a bypass route and a rate-limiting dwell time manifest themselves as plateaus observed in the rate curves at low and high forces, respectively, in Fig. 3.6.

A spreadsheet containing the model parameters, calculations, and graphs, is provided in Supp. File 4. All the formulas used in the kinetic scheme are also summarized in section 3.5.5.

3.4. Discussion

3.4.1. Model predictions agree with experimental data

Based on clues from structural observations (Fig. 3.1), we have described a model for the ribosomal helicase that envisions two active sites operating in tandem to unwind mRNA structures encountered by the ribosome (Fig. 3.2). We have also developed a simple kinetic scheme to quantitatively describe the sliding and bypass routes and to approximate translation rates under this model (Figs. 4). The kinetic scheme can fully account for the rates of ribosome translocation on long mRNA hairpins measured by single-molecule force spectroscopy using optical tweezers (Qu et al., 2011) (Fig. 3.6). Since a commonly used model (Betterton and Jülicher, 2005) for non-ribosomal helicases had been found to be inadequate in explaining the force dependence of the measured rates, it was proposed that the ribosome uses two active mechanisms to unwind mRNA structures: a classical active unwinding mechanism through duplex destabilization, as seen in other active helicases, plus a novel unwinding mechanism with a force-independent rate constant that depends on base pair stability at the junction and operates directly on a closed junction (Qu et al., 2011). This model can be mapped onto ours by assigning the second mechanism not to unwinding *per se*, but to the "bypass" step at the distal active site.

The parameter values obtained from fitting our model to the optical tweezers data are physically reasonable (Table 3.1). The binding energy $\Delta G_{binding}$ (~ 3 kcal/mol per nucleotide, a total of ~9 kcal/mol for the interface) is within the range of expected energies for three electrostatic interactions between negatively-charged phosphates (mRNA) and positively-charged guanidinium groups (arginines in S3) ~3Å apart (Anderson et al., 1990; Finer-Moore et al., 1996) (Fig. 3.1 and section 3.5.1). Such large binding energy is beneficial, since the higher the binding energy, the less likely it is for the ribosome to encounter a closed junction at the proximal active site, making the latter more "active" (Betterton and Jülicher, 2005). However, a higher binding energy comes with a kinetic cost, since the rate of the bypass route (k_{off}^{S3}), which serves as a time-keeper to prevent long delays at the distal active site, generally decreases with increasing $\Delta G_{binding}$. In the case of the ribosome, other steps of the translation cycle, e.g. the tRNA accommodation step, are also slow; therefore, as long as bypass does not become significantly slower than the net rate of those steps, a higher $\Delta G_{binding}$ comes at little extra time cost to the overall process of translation. This may not be the case for a *dedicated* helicase for which RNA unwinding is the only rate-limiting step. We obtained similar estimates for the net rate of the non-translocation steps (k_{dwell}) and the rate of bypass (k_{off}^{S3}), ~1.3 nt/s and ~1.4 nt/s respectively, suggesting that the binding energy has been optimized in accordance with the rest of the translation cycle, such that none of the rates dominate under normal conditions. This ensures that the overall translation rate is maintained close to the same value on both single-stranded and modestly structured regions of mRNA. Indeed a genome-wide correlation has been found between the propensity for base-pairing in a region of mRNA and the optimality of codon usage in that region (Gorochowski et al., 2015), supporting the notion that there is an evolutionary pressure to smooth out variations in translation rates.

The sliding and bypass routes in our model are predicted to result in different changes in the observed end-to-end extension of the mRNA, although both routes allow translocation of mRNA with respect to the ribosome by exactly 3 nucleotides. Starting from a *proximal-bound* state before translocation, the sliding route produces a single translocation step of 6 nt corresponding to the opening of the distal segment and its complement (Fig. 3.7A; for highly stable hairpins, individual 2-nt substeps may be detected within this step depending on the resolution limit of the instrument).

In contrast to sliding, the bypass route does not unwind the distal duplex, but merely disrupts the pre-existing mRNA-S3 interaction in the proximal segment. This is equivalent to the reorientation of this segment from orthogonal to parallel with respect to the pulling force, and produces only a 3-nt step. After this bypass, and most likely during the next dwell time controlled by k_{dwell}, unwinding and subsequent equilibrium binding of the new proximal segment to S3 occurs, allowing its complement to extend in the direction of the force, creating another 3-nt extension step (Fig. 3.7B). Therefore, we predict that sliding produces a single 6-nt step, whereas bypass produces two 3-nt steps, one from the bypass step itself, and one from the following equilibrium unwinding and binding. Indeed, such occasional 3-nt "substeps" of ribosome translocation have recently been observed using improved optical tweezers instrumentation (Bustamante group, UC Berkeley, personal communication). We predict substeps to be more common at low forces and for more stable hairpins, and to preferentially occur after longer waiting times, as expected for bypass events. The presence of substeps is a consequence of orthogonality of the S3 binding interface with respect to the pulling direction (Fig. 3.8, also see section 3.5.3); bypasses would become "invisible" if the binding interface was parallel to the pulling force, as they would have not resulted in a significant change in end-to-end extension. In that case, the subsequent equilibrium unwinding and binding would have produced a full 6-nt step.

Another prediction of our model is that less stable structures are likely to be unwound via the sliding route at the distal active site, while more stable structures are likely to remain intact, proceed via bypass, and unwind at the proximal active site one translocation cycle later. Furthermore, sliding of S3 over mRNA in our model predicts that structured mRNAs can affect translocation rate even when translocation brings them from position +15 to +12, still outside of the ribosome, since these structures resist unwinding at the distal active site. This would be manifested as a decrease in the rate of reverse 30S head rotation, which is when sliding would occur. If completion of reverse head movement is correlated with E-site tRNA release (Belardinelli et al., 2016; Ratje et al., 2010), this means stable hairpins at the distal active site can slow down E-site tRNA release before reaching the tunnel entrance. These predictions are in striking agreement with results of a study (Chen et al., 2013) in which single-molecule Förster resonance energy transfer (smFRET) was used to monitor dwell times during ribosome translocation on mRNAs with stem-loops of either 65% or 100% GC content starting at position +15. It was found that, as the ribosome translocates toward the stem-loop, it is the rate of E-site tRNA release, rather than tRNA translocation, that is affected first. Furthermore, as predicted, the 100% GC stem-loop affects translocation rates one elongation cycle earlier than the 65% GC stem-loop at the same position (Fig. 3.9).

3.4.2. Nucleic acid unwinding by stick-slip may be widespread

The bifurcation in the unwinding process at the distal active site (sliding vs. bypass) is reminiscent of the stick-slip phenomenon (Supp. File 3). Stick-slip is the jerky (non-uniform) movement when two interacting surfaces move relative to each other, characterized by alternating “stick” (slow or no motion) and “slip” (rapid motion) phases, as predicted by the Prandtl-Tomlinson model for friction (Popov and Gray, 2014). First studied in the context of sliding of metal surfaces at the centimeter scale (Bowden and Leben, 1939), and familiar in everyday observations such as the squeak of sneakers on basketball courts and the squeal of car brakes, stick-slip has since been observed in a wide range of scales, from seismic motions in earthquakes (Brace and Byerlee, 1966) to atomic-scale sliding motions studied by friction force microscopy (Krylov and Frenken, 2014). Indeed, force unwinding of nucleic acid duplexes, e.g. by optical tweezers, in force-ramp experiments demonstrates a nano-scale stick-slip phenomenon (Bockelmann et al., 1997), as does the pulling of nucleic acids through nanopores (Nelson et al., 2014), demostrating the applicability of this universal behavior to RNA interactions.

We propose that mRNA unwinding by the ribosome is accompanied by a mix of stick-slip phenomena, whereby encountering a stable duplex at the distal active site causes the system to transition from smooth sliding into the stick-slip regime. In this regime, the duplex remains “stuck” at the distal active site while the pulling force along the mRNA, $F_{ribosome}$, which results from ribosomal conformational changes (i.e. head rotation) during translocation, gradually increases. Opening of the duplex can then allow a return to the sliding regime, accompanied by a minor “slip,” in which $F_{ribosome}$ drops to a lower level. But if the duplex does not open, $F_{ribosome}$ continues to increase to a point where the mRNA-S3 binding itself may be disrupted, leading this time to a major “slip” (which we call bypass) accompanied by a relatively larger sudden drop in $F_{ribosome}$. After multiple translation cycles, this would create a sawtooth $F_{ribosome}$ profile, a hallmark of stick-slip, where the minor and major slips would correspond to the sliding and bypass routes, respectively (Fig. 3.10). In this picture, it is evident that the bypass route acts as a time-keeper to prevent long delays at the distal active site. Without bypass, a stable hairpin would have to remain stuck at the distal site for as long as it is base-paired, which means that the next, proximal, active site would never be utilized for unwinding. With bypass, the helicase would thus have two chances at unwinding: once at the distal active site, and if that takes too long, once more at the proximal active site after bypassing the distal site. Since the proximal active site cannot be bypassed, starting translocation with a highly stable duplex which has remained closed up to this site can result in $F_{ribosome}$ reaching even higher values, until it is relieved by a yet larger slip, which may correspond to either duplex opening, ribosome back-slippage (frameshifting), or structural distortions in the ribosome (e.g. "hyper-rotation" (Qin et al., 2014)). We expect that when such rare large slips occur, they do so one cycle after a major slip (bypass) event, which had allowed the duplex to reach the proximal active site in the first place.

3.4.3. The tandem active site model makes further testable predictions

Our model predicts that compromising the mRNA-S3 binding interaction (either by mutations, or by changing the binding conditions) would change the unwinding kinetics observed in the tweezers experiments (Qu et al., 2011). For instance, simply changing the ionic conditions in the tweezers experiments should have a predictable effect. High ionic strength is expected to weaken the electrostatic interactions between S3 and mRNA, while stabilizing mRNA duplexes. According to this model, a low value of exp($m\Delta G_{binding}$) under such conditions would render the ribosomal helicase less active (by indirectly affecting the proximal active site), and will also tend to eliminate the the low-force plateau that was attributed to a second active mechanism and which we propose to be due to the bypass route. Eliminating the cooperative all-or-none mRNA-S3 binding would also make it easier to observe individual helicase steps of one nucleotide pair in these experiments. Of course, these steps would still be associated in groups of three due to the translocation step size.

The tandem active site model can be employed to describe some aspects of programmed ribosomal frameshifting. After bypassing the distal active site and resisting equilibrium unwinding by S3, a stable pseudoknot or stem-loop structure has to spontaneously open at the proximal active site in order for translocation to proceed. While it remains closed, the high-affinity binding site on S3 for single-stranded mRNA remains vacant. Assuming that the reverse head rotation during translocation creates a tension in the region of mRNA that lies between the tRNA-bound codons and the pseudoknot at the tunnel entrance (see Fig. 3.10), one way to view the frameshifting process is as a kinetic competition between two sets of binding events: (1) binding between S3 and the single-stranded mRNA segment just 5’ to the pseudoknot, and (2) the different possible codon-anticodon binding arrangements in the A and P sites over the slippery sequence. In this picture, a slippery sequence puts S3 at an advantage because some of the binding arrangements in (2) may be compatible with S3 binding in (1). Given a sufficiently long pause caused by the pseudoknot, S3 can potentially bind to the already internalized single-stranded segment 5’ to the pseudoknot. This scenario is consistent with a recent dissection of multiple pathways for -1 ribosomal frameshifting (Yan et al., 2015) which found a significant fraction of -4 frameshifting events (resulting in the incorporation of an extra amino acid in the frameshifted product). It is conceivable that three of the four slipped nucleotides in such an event allow S3 to re-bind to the 3 single-stranded nucleotides upstream of the pseudoknot, thus bringing the pseudoknot back to the distal active site.

Despite the adequacy of this simple kinetic scheme in fitting the tweezers data, and the ability of the tandem active site model to explain experimental observations, the kinetic scheme is merely an approximation. For example, there exists the possibility of single-stranded mRNA binding to the ribosome outside of what we call the proximal segment (from position +12 to +14), as does the possibility that some *double-stranded* mRNA binding to S3 also occurs due to the flexibility of the binding interaction (mediated by the long side chains of arginine and lysine) and its electrostatic nature, albeit with lower affinity. Furthermore, the quantitative effect of the force exerted on the mRNA by the small subunit head rotation ($F_{ribosome}$) on the rate constants has not been incorporated in this scheme. In summary, our model provides a testable kinetic framework to further study the ribosomal helicase and analyze its mechanism of action.

3.5. Supplementary notes

3.5.1. The S3-mRNA binding interface

The structural evidence, summarized in Fig. 3.1, shows that most of the binding interaction between mRNA and S3 is concentrated near the distal active site, where two positively-charged residues, Arg132 and Arg136, make the closest approaches (4Å or closer) to the backbone phosphates of residues +14 and +15 in the mRNA. Although atomic coordinates are not certain given the resolution of our structural data, it is clear that the Arg132 side chain is in position to form salt bridges with both phosphates +14 and +15, while Arg136 side chain can interact with the +15 phosphate only. Assuming that each salt bridge contributes ~3 kcal/mol to the free energy of binding (Anderson et al., 1990; Finer-Moore et al., 1996), these three salt bridges would be sufficient to account for the estimated total mRNA-S3 binding energy of ~9 kcal/mol (Table 3.1). Thus, incidentally, there are three salt bridges between S3 and the proximal segment, the same as the number of bound nucleotides (*m*). The salt bridges cannot form with an intact A-form duplex in the proximal mRNA segment, because the curvature of A-form geometry would place the strand too far from Arg132 and Arg136 given the shape of the tunnel entrance in the classical state. The preference for single-stranded mRNA binding thus appears to be achieved mainly by steric selection: the proximal mRNA segment can either stay double-stranded, or become single-stranded and bend toward the distal active site to form the above salt bridges, with little possibility for intermediate binding states (i.e.

with only one or two nucleotides bound). Such binding cooperativity also implies that the formation or loss of one of the salt bridges would be rate-limiting in the overall binding or unbinding of single-stranded mRNA to S3; once one of them is formed, the other salt bridges follow rapidly.

3.5.2. Placement of the *bound* state

The Boltzmann factor for the *proximal-bound* state in Eq. 3.1.3 may be more accurately described as $\exp(m\Delta G_{binding}) + \exp(0.5m[F \cdot X_F - \Delta G_{stretch}])$, the second term of which describes the stability of the *complement* of the bound strand, which is single-stranded in this state and can be stretched. In other words, the *bound* state is halfway between the *closed* and *open* states along the unfolding coordinate, consistent with the experimental observation of the 3-nt substeps described in the main text. In this case, in addition to stabilizing the *open* state at the expense of the other two states, the pulling force is expected to also stabilize the *bound* state at the expense of the *closed* state, as shown in Fig. 3.11A. Translation rates for the GC50% hairpin remain essentially unchanged after introducing this modification. The curve for the GC100% hairpin shows a shallow rise at low forces, mirroring the stabilization of the *bound* state. Best fit to tweezers data is now obtained using a k_{off}^{S3} parameter value of 1.2 nt/s instead of 1.4 nt/s, but the other parameters are unchanged (Fig. 3.11B). The shallow rise disappears with higher values of the $\Delta G_{binding}$ parameter.

3.5.3. Translocation over the *proximal-open* state

Translocation over the *proximal-open* state is not considered in this work because given the stability of the other two states, this state is never present as a significant fraction unless at forces close to the critical force for the mRNA hairpin, F_c, and its inclusion is inconsequential in this case. If $\exp(m\Delta G_{binding})$ is small for a helicase, "passive" unwinding would dominate, and the *open* fraction would have to be incorporated. In that case, $k_{translocation}$ in Eq. 3.7 would contain the extra term $P_{proximal\text{-}open}(F)\ k_{translocation\text{-}open}$, where $P_{proximal\text{-}open}(F)$ is the probability for the proximal segment to be in the *open* state at force F, and $k_{translocation\text{-}open}$ is the rate of translocation in the absence of S3 binding. In our analysis of data from wild-type ribosomes (Qu et al., 2011), significantly changing the value of the latter parameter, from 0 to orders of magnitude greater than the other rates, has no effect on the overall translation rate.

3.5.4. Force-independence of the k_{on} and k_{off} rates in Eqs. 3.4-3.6

Although the equilibrium position for mRNA-S3 binding is force-dependent, the *rate constants* for binding and disruption in the sliding and bypass routes, respectively, are not. The effect of pulling forces on the rate constants of a reaction depends on the shape of the free energy landscape along the pulling coordinate and is different for different reactions. For a binding reaction that is affected by force, if the transition state is closer to the bound state (than to the unbound state) along this coordinate, the on and off rates become mostly force-dependent and force-independent respectively, and vice versa. For the sliding route in our model, one can assume that k_{on} is fully force-dependent or fully force-independent, and this would not qualitatively affect the kinetics (Fig. 3.12A). We assume force-independence, since mRNA binding to S3 *per se* in the sliding route is not accompanied by a change in mRNA end-to-end distance (although the sliding route as a whole is), and as expected, this gives a slightly better fit to the data. For k_{off}, however, force-independence is *required* to qualitatively fit the tweezers data and to show a low-force plateau (Fig. 3.12B). This indicates that the transition state for the bypass route has approximately the same end-to-end extension as the bound state; in other words, conversion to the transition state must occur at a right angle to the force vector. This is in line with the binding cooperativity described in section 3.5.1 and the orthogonality of the S3 binding interface with respect to the pulling direction (Fig. 3.8): Before bypass, the mRNA lies along the binding interface, normal to the pulling force; commitment to bypass is made in an all-or-none fashion once the salt bridges are disrupted near the distal active site, only after which the mRNA is released to enter the tunnel and increase the end-to-end extension. This means that the transition state is close to the bound state.

3.5.5. Formulae used in the kinetic scheme

All the equations used for the kinetic scheme of our model are summarized in this section.

(Parameters: $\Delta G_{binding}$ =5.2 k_BT, k_{dwell} =1.29 nt/s, k_{off}^{S3}=1.42 nt/s, $\Delta G_{bpGC50\%}$=3.7 k_BT, $\Delta G_{bpGC100\%}$=5.1 k_BT)

Overall translation rate:

$$k_{overall} = (k_{dwell}\, k_{translocation}) / (k_{dwell} + k_{translocation}) \tag{3.8}$$

Net translocation rate:

$$k_{translocation} = P_{proximal\text{-}bound}(F)\ (k_{slide}(F) + k_{bypass}) \tag{3.7}$$

Net rate of the sliding route:

$$k_{slide}(F) \approx k_{bind}(F) = P_{distal\text{-}open}(F)\, k_{on}^{S3} \tag{3.4}$$

$$k_{on}^{S3} = k_{off}^{S3} \exp(\Delta G_{binding}) \tag{3.5}$$

Net rate of the bypass route:

$$k_{bypass} = k_{off}^{S3} \tag{3.6}$$

Probabilities and the partition function for the proximal segment:

$$P_{proximal\text{-}open}(F) = \exp(m[FX_F - \Delta G_{stretch}])\ /\ Z(F) \tag{3.9.1}$$

$$P_{proximal\text{-}closed}(F) = \exp(m\Delta G_{bp})\ /\ Z(F) \tag{3.9.2}$$

$$P_{proximal\text{-}bound}(F) = \exp(m\Delta G_{binding})\ /\ Z(F) \tag{3.9.3}$$

$m = 3$

$$Z\,(F) = \exp(m\Delta G_{binding}) + \exp(m\Delta G_{bp}) + \exp(m[FX_F - \Delta G_{stretch}]) \qquad (3.9.4)$$

Probabilities and the partition function for the distal segment:

$$P_{distal\text{-}open}(F) = \exp(s[FX_F - \Delta G_{stretch}])\ /\ Z'(F) \qquad (3.10.1)$$

$$P_{distal\text{-}closed}(F) = \exp(s\Delta G_{bp})\ /\ Z'(F) \qquad (3.10.2)$$

$s = 3$

$$Z'\,(F) = \exp(s\Delta G_{bp}) + \exp(s[FX_F - \Delta G_{stretch}]) \qquad (3.10.3)$$

Force-extension relations for the WLC model:

$$X_F \approx 2L \bullet \left(\frac{4}{3} - \frac{4}{3\sqrt{f+1}} - \frac{10\exp(\sqrt[4]{\frac{900}{f}})}{\sqrt{f}\left(\exp(\sqrt[4]{\frac{900}{f}}) - 1\right)^2} + \frac{f^{1.62}}{3.55 + 3.8f^{2.2}} \right)$$

(Petrosyan, 2017)

$$f = \frac{FP}{k_BT}, \qquad k_BT = 4.11 \text{ pN.nm}, \qquad P = 1 \text{ nm}, \qquad L = 0.59 \text{ nm/nt} \qquad (3.11)$$

$$\Delta G_{stretch}\,(F) = \int_0^{X_F} F.dx_{SS} \approx \frac{L}{P} \cdot \frac{3\left(X_F/2L\right)^2 - 2\left(X_F/2L\right)^3}{4\left(1 - X_F/2L\right)}$$

(Tinoco and Bustamante, 2002) (3.12)

The following formulae were used to replicate the model from Qu et. al., 2011:

(Parameters: $\Delta G_d = 1.5\ k_BT$, k_{ss}=1.29 nt/s, $k_{dsGC50\%}$=0.69 nt/s, $k_{dsGC100\%}$=0.48 nt/s,

$\Delta G_{bpGC50\%}$=3.7 k_BT, $\Delta G_{bpGC100\%}$=5.1 k_BT)

Overall rates:

$$v_{ds(\mathrm{GC50\%})} = P_{open}(F)\ k_{ss} + P_{closed}(F)\ k_{ds(\mathrm{GC50\%})} \tag{3.13}$$

$$v_{ds(\mathrm{GC100\%})} = P_{open}(F)\ k_{ss} + P_{closed}(F)\ k_{ds(\mathrm{GC100\%})} \tag{3.14}$$

Probabilities and the partition function:

$$P_{open}\ (F) = 1\ /\ Z''(F) \tag{3.15.1}$$

$$P_{closed}\ (F) = \exp(\delta[\Delta G_{bp} - \Delta G_d - (FX_F - \Delta G_{stretch})])\ \ /\ Z''(F) \tag{3.15.2}$$

$\delta = 3$

$$Z''(F) = 1 + \exp(\delta[\Delta G_{bp} - \Delta G_d - (FX_F - \Delta G_{stretch})]) \tag{3.15.3}$$

Force-extension relations for the WLC model: same as above.

Table 3.1. Parameters of the kinetic scheme after fitting to optical tweezers data

Parameter	Description	Value	
$\Delta G_{binding}$	mRNA-S3 binding stability	5.2 k_BT/nt	(3 kcal/mol.nt)
k_{off}^{S3}	mRNA-S3 dissociation rate constant	1.42 nt/s	(0.47 codons/s)
k_{dwell}	Overall rate of unhindered translation	1.29 nt/s	(0.43 codons/s)

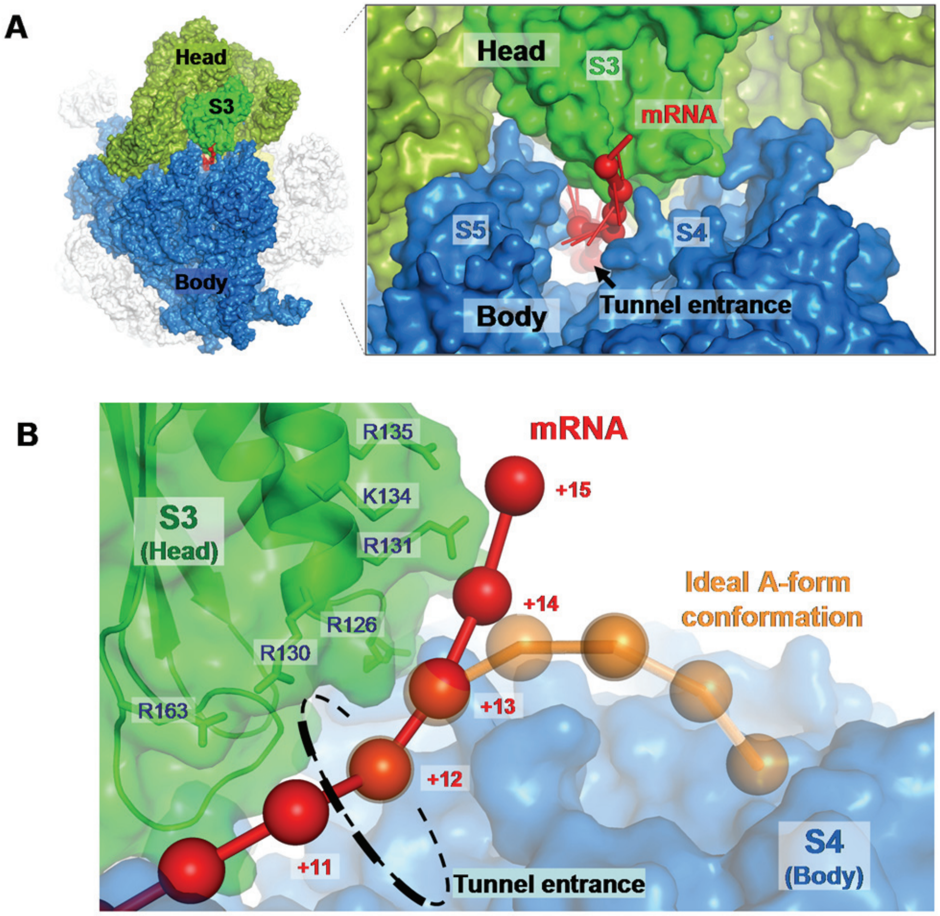

Figure 3.1. Binding of single-stranded mRNA to ribosomal protein S3 outside of the mRNA tunnel entrance. *A*. The 3’ end of the mRNA (red) emerges at the tunnel entrance between the head domain (olive green) and the body domain (blue) of the small ribosomal subunit, and interacts with protein S3 (green) outside of the tunnel. *B*. The path of the S3-bound single-stranded mRNA (*red*) outside of the tunnel deviates from that of an ideal A-form conformation (orange). The phosphorus atom of each nucleotide is represented by a sphere. Note that despite binding to S3 via its 5’ phosphate, the +15 nucleotide is not limited in its base-pairing because its 3’ phosphate (not shown) is unrestrained.

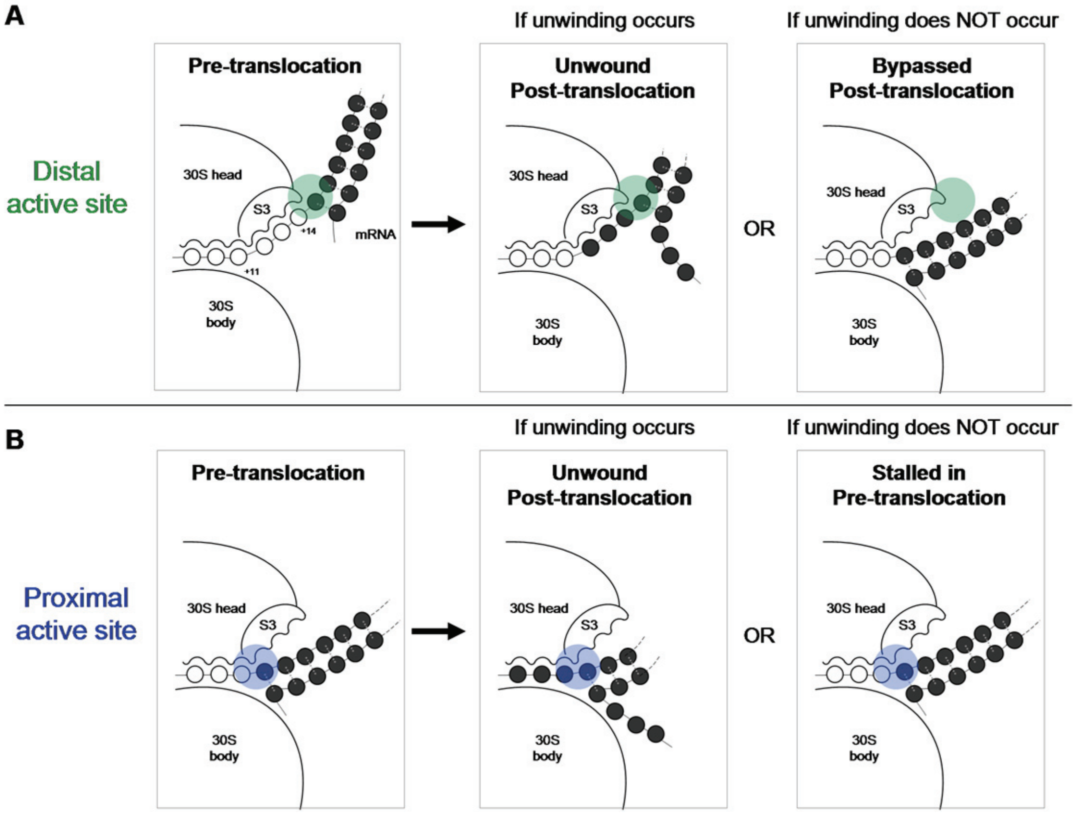

Figure 3.2. The tandem active site model for the ribosomal helicase. *A and B.* Cartoons showing encounters between downstream helical mRNA elements and the distal active site (green circle in *A*) and proximal active site (blue circle in *B*). For each active site, the pre-translocation state (left panel), and the outcome with and without unwinding (middle and right panels, respectively) are shown. *A.* At the distal active site (at +14), if unwinding occurs, S3 can slide over the unwound segment. If no unwinding occurs, the structure can "bypass" this active site. Either of these scenarios allows mRNA translocation by 3 nucleotides. *B.* At the proximal active site (at +11), translocation can proceed only if unwinding occurs. If unwinding does not occur, the ribosome will remain stalled in the pre-translocation state.

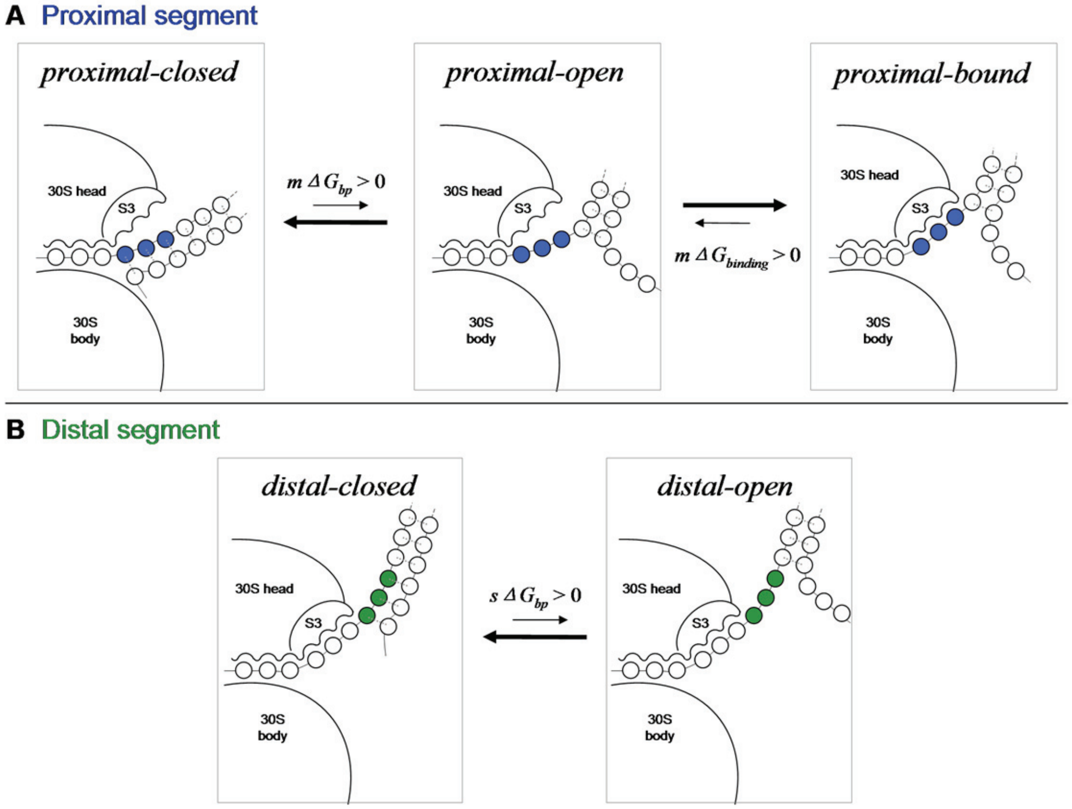

Figure 3.3. mRNA states in the tandem active site model. The microstates of (*A*) the proximal segment, and (*B*) the distal segment of the mRNA outside of the tunnel entrance. Stabilities of the states in the absence of any external force are inicated. *A*. The proximal segment (blue) can be in one of three states (*closed*, *open*, or *bound*). *B*. The distal segment (green) can be in one of two states (*closed* or *open*).

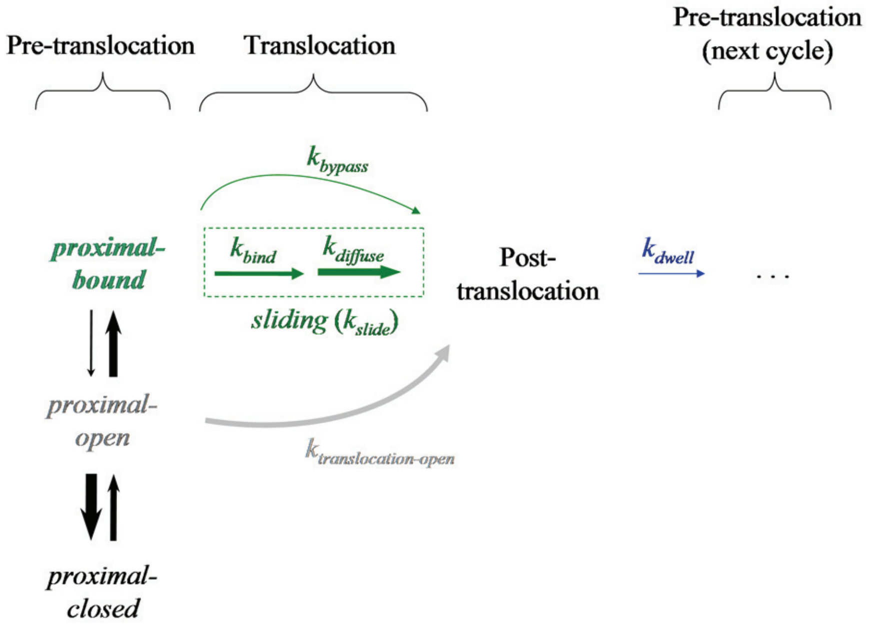

Figure 3.4. The kinetic scheme for the tandem active site model. The pre-translocation equilibrium in the proximal segment is indicated on the left. To be able to translocate, the system has to be in the *bound* or *open* state of this segment. The rate of translocation depends on mRNA duplex stability in the proximal segment (affecting the probability of the *bound* state), and on mRNA duplex stability in the distal segment (affecting k_{bind} in the sliding route). After translocation and during the time controlled by k_{dwell}, the new proximal segment can approach equilibrium between its three states prior to the next translocation step. Qualitative differences in the rate constants are indicated by arrow width, but the length of each arrow is arbitrary.

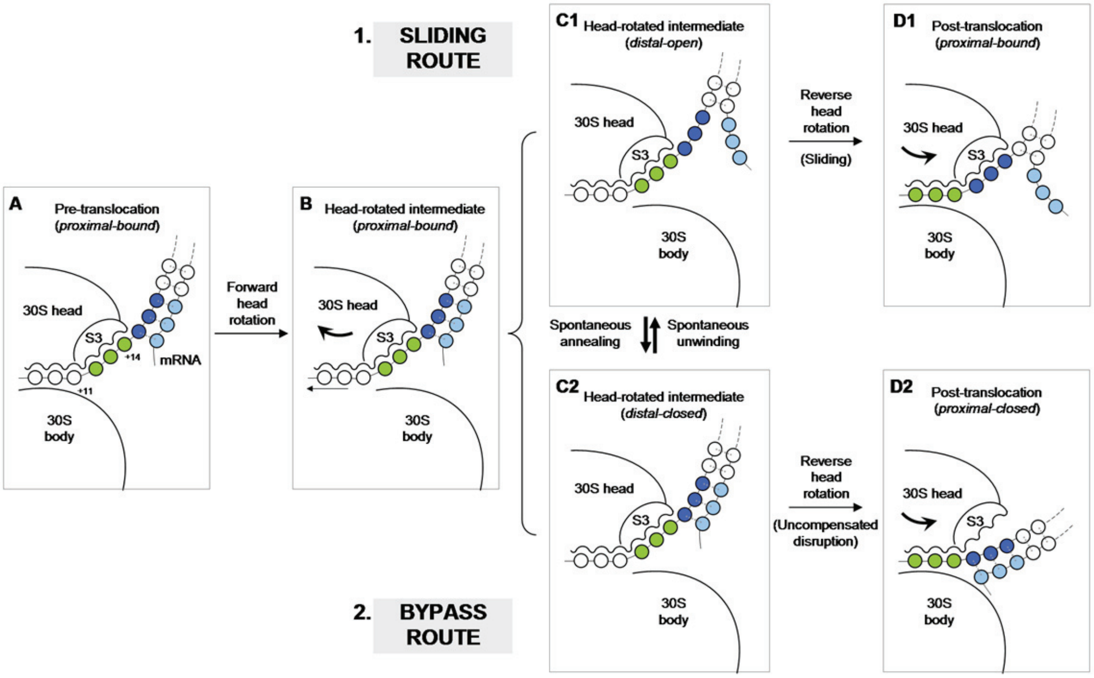

Figure 3.5. Translocation over an mRNA hairpin encountered at the distal active site. The proximal segment in the pre-translocation mRNA is in green. The distal segment and its complement are indicated in dark blue and light blue, respectively. *A*. Before translocation starts, the proximal mRNA segment is in the *bound* state and interacts with S3 between the proximal and distal active sites, at positions +12 to +14. *B*. Forward head rotation moves S3 (part of the head domain) along with its bound mRNA as a rigid body relative to the body domain. No unwinding has to occur at this step at the distal active site. *C1 and C2*. The head-rotated intermediate in panel *B* is in fact composed of two different states of the *distal* segment, namely (*C1*) the *distal-open* state, and (*C2*) the *distal-closed* state, which are in equilibrium. The same equilibrium exists in the pre-translocation state (panel A), but not shown for simplicity. *D1 and D2*. During reverse head rotation, the head domain moves back toward its classical state, whereas the mRNA remains in place, forcing S3 to move relative to the mRNA. If the distal segment is open, S3 either can slide along the mRNA, resulting in a post-translocation state in which the now-proximal segment is in the *bound* state (*D1*). If the distal segment is closed, S3 loses its bound mRNA

without acquiring compensatory binding, resulting in a *proximal-closed* post-translocation state (*D2*). The latter has to spontaneously convert to *proximal-bound* state before the next translocation step can take place. The sliding route proceeds through *C1* and *D1* at net rate k_{slide}, and the bypass route proceeds through *C2* and *D2* at net rate k_{bypass}. Note that according to the kinetic scheme, the *distal-open* state (panel *C1*) can also undergo uncompensated disruption to yield a *proximal-open* post-translocation product (not shown), but this occurs relatively rarely for this state, and ommittd here for simplicity.

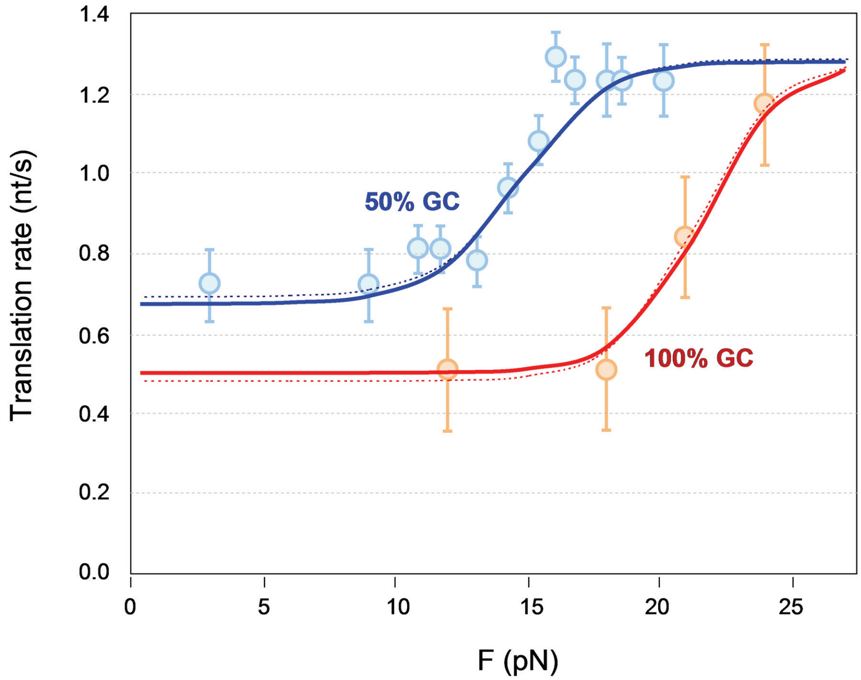

Figure 3.6. Agreement of optical tweezers data with the tandem active site model. The translation rates predicted by the kinetic scheme for the tandem active site model are in close agreement with the measured translation rates under different optical tweezers pulling forces (Qu et al., 2011), for unwinding of hairpins with 50% and 100% GC content (blue and red curves, respectively). Each data point shows the mean measured rate and the standard error of the mean. The dotted curves are reproduced from the fitting curves in Ref. (Qu et al., 2011) to show the near-perfect overlay. The complete set of parameter values used are listed in section 3.5.5.

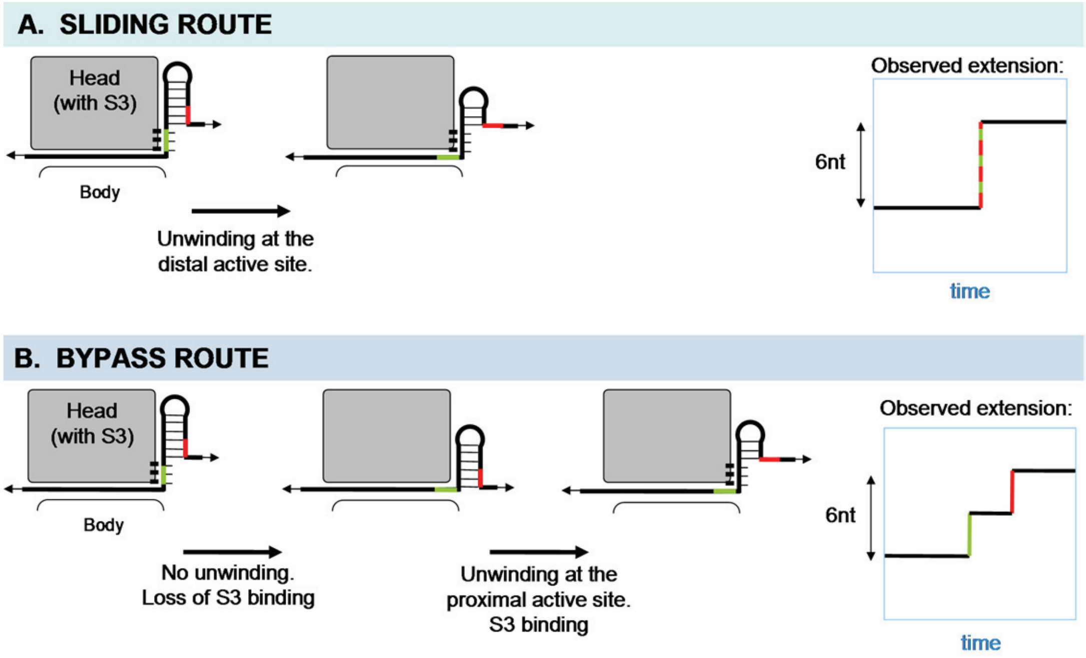

Figure 3.7. End-to-end extension change in the sliding and bypass routes. Prediction of end-to-end mRNA extension in tweezers experiments based on the tandem active site model is shown for the sliding and bypass routes. The head domain of the small subunit is shown in gray, and the interaction between the mRNA proximal segment and S3 is indicated. *A.* The sliding route generates a major 6-nt step due to unwinding of the distal segment during translocation. *B*. The bypass route can generate two distinct 3-nt steps, the first of which is due to bypass itself during translocation, and the second of which is due to unwinding and equilibrium binding of the new proximal segment after translocation. Note that the segment indicated by green does not have to become horizontally oriented for the first substep to be observed; as long as it is internalized, three nucleotides from the other end of the head domain are released and become horizontal.

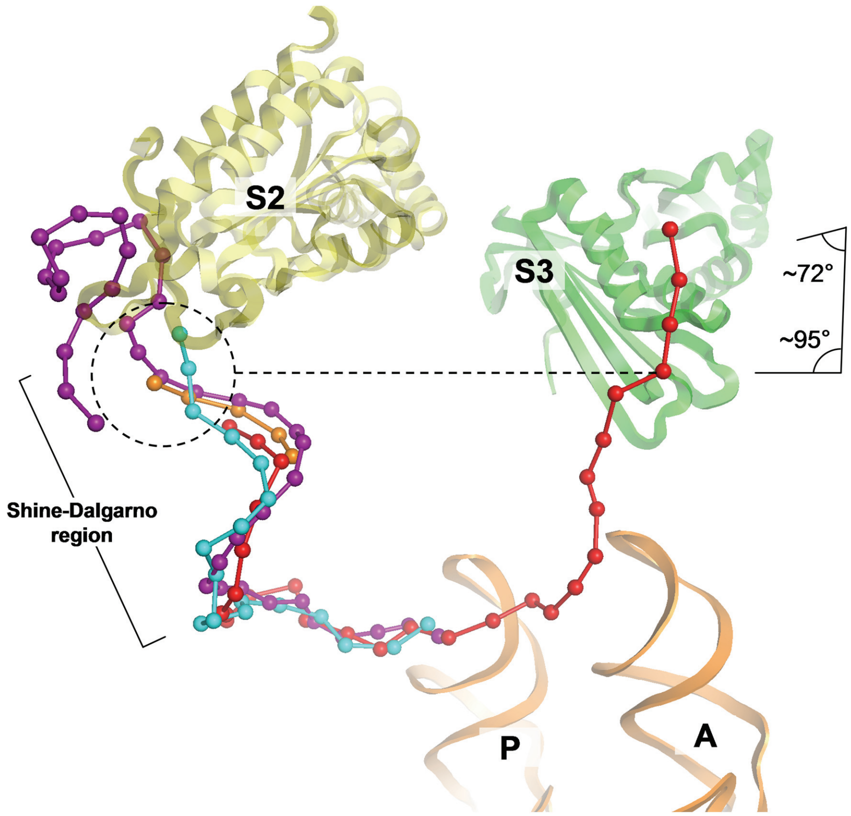

Figure 3.8. Orthogonality of the S3 binding interface relative to pulling direction. The path of the mRNA around the neck of the small ribosomal subunit, viewed from body domain of the subunit. A and P denote A- and P-site tRNAs. The paths of the mRNA are taken from our crystal structure (Chapter 2, red), and from PDB IDs 4w29 (cyan), 4v4y (purple), and 2e5l (orange) (Kaminishi et al., 2007; Yusupova et al., 2006; Zhou et al., 2014), after alignment of the structures on the body of the 30S subunit. For clarity, only the red mRNA is shown in full length. Assuming that the furthest mRNA-ribosome interaction in the 5' side of the mRNA occurs at the end of the Shine-Dalgarno helix near protein S2 (highlighted by a dashed circle) in an elongating ribosome, the mRNA-S3 binding interface makes a roughly right angle to the direction of the pulling force, which would pass through the first and last point of mRNA-ribosome interaction.

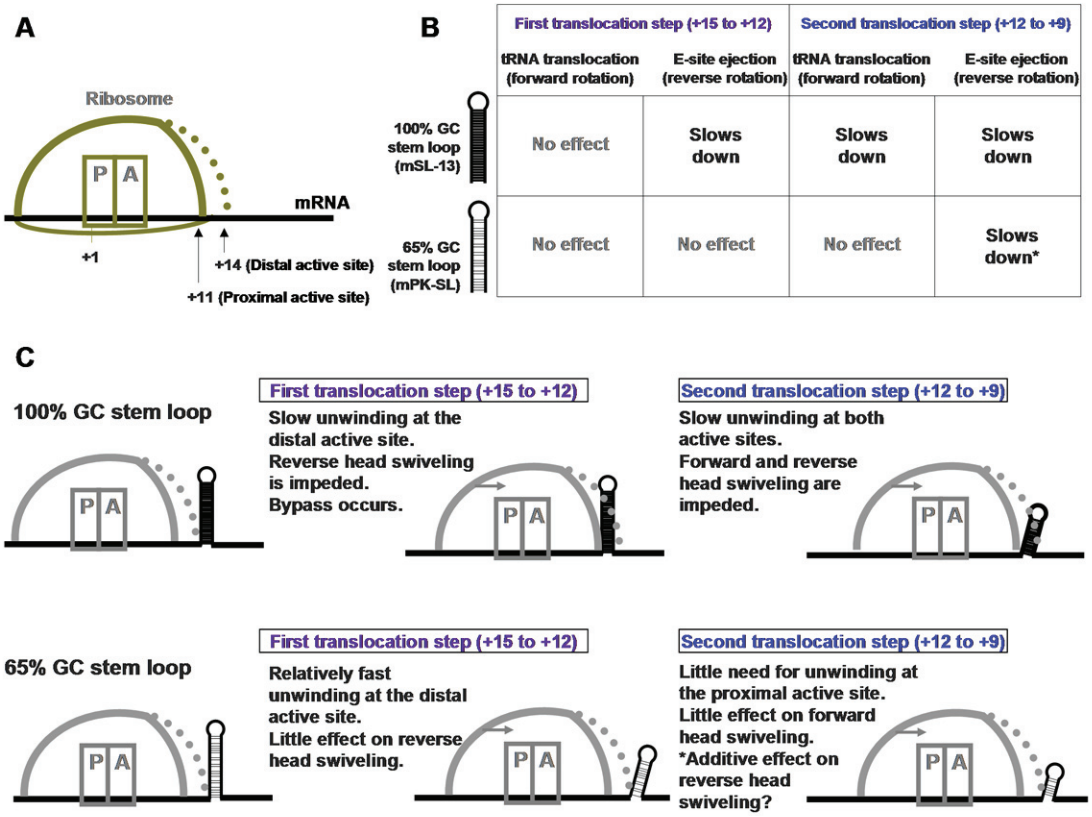

Figure 3.9. Agreement of smFRET data with the tandem active site model. Explaining the effect of mRNA secondary structures on translation rates, as measured by smFRET (Chen et al., 2013), using the tandem active site model. *A*. Cartoon representing the ribosome and its proximal and distal helicase active sites. *B*. Summary of experimental data on the effect of two stem-loop structures (100% and 65% GC content) on the rates of forward and reverse rotation of the 30S head in two consecutive translocation steps (adapted from from Table S2 in the published study (Chen et al., 2013). *C*. Predictions of the tandem active site model for the rates of the steps outlined in panel *B*.

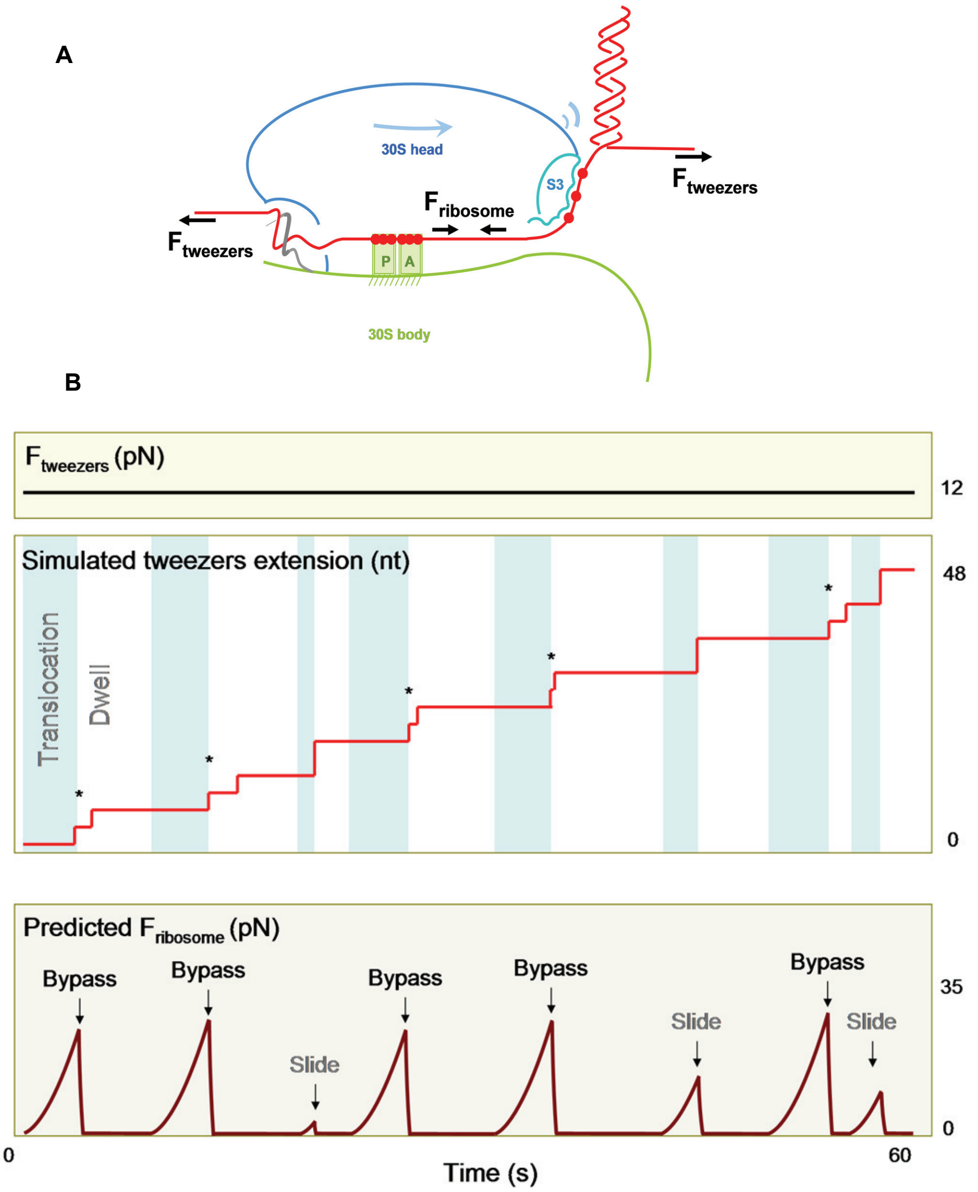

Figure 3.10. Stick-slip prediction for the ribosomal helicase. *A.* Schematic diagram of the portions of mRNA (red) that are expected to be under tension from the experimental pulling force ($F_{tweezers}$) or the ribosomal pulling force ($F_{ribosome}$) during reverse head rotation starting from the *bound* state. In this state, the mRNA is anchored to the tRNAs (A and P) which can be considered to be fixed on the body domain (green), whereas the head domain (blue) is attached to the downstream end of

the mRNA via S3 and starts moving to the right. If the distal hairpin does not open, head movement would create tension in the intervening mRNA, and the tension increases as the head continues to move, resisting the movement. In this model, the upstream part of the mRNA exits the ribosome on the opposite side of the head domain (left) after sliding over the anti-Shine-Dalgarno sequence of the 16S rRNA (gray). *B*. Under a constant tweezers pulling force of ~12 pN (top graph), a simplified simulation of the mRNA end-to-end extension is shown (middle graph) during translocation over 8 codons in a 50% GC hairpin mRNA, with a qualitative prediction for $F_{ribosome}$ (bottom graph) if it could be measured experimentally at the same time. Each translocation cycle is composed of a translocation time (controlled by $k_{translocation}$) and a dwell time (controlled by k_{dwell}), indicated by light blue and white stripes, respectively. $F_{ribosome}$ increases in each translocation step due to the hairpin resisting the sliding route at the distal active site, and eventually drops to zero if either the hairpin yields (slide) or the S3-mRNA binding yields (bypass) whichever happens sooner. This creates a sawtooth pattern (stick-slip behavior). The slips that occur by bypass correspond to the appearance of substeps in the extension profile (asterisks). Under the given tweezers force and hairpin stability, roughly one out of four translocation steps occur by sliding, and dwell times take up more than half of the total (~1min) translation time. An estimate of 35 pN for the $F_{ribosome}$ near the bypass peaks in the bottom graph is based on the reversible work needed to overcome mRNA-S3 binding energy, ($m\Delta G_{binding}$) = 15.6 k_BT = 64 pN.nm, divided by the contour length of three nucleotides, ~1.8 nm.

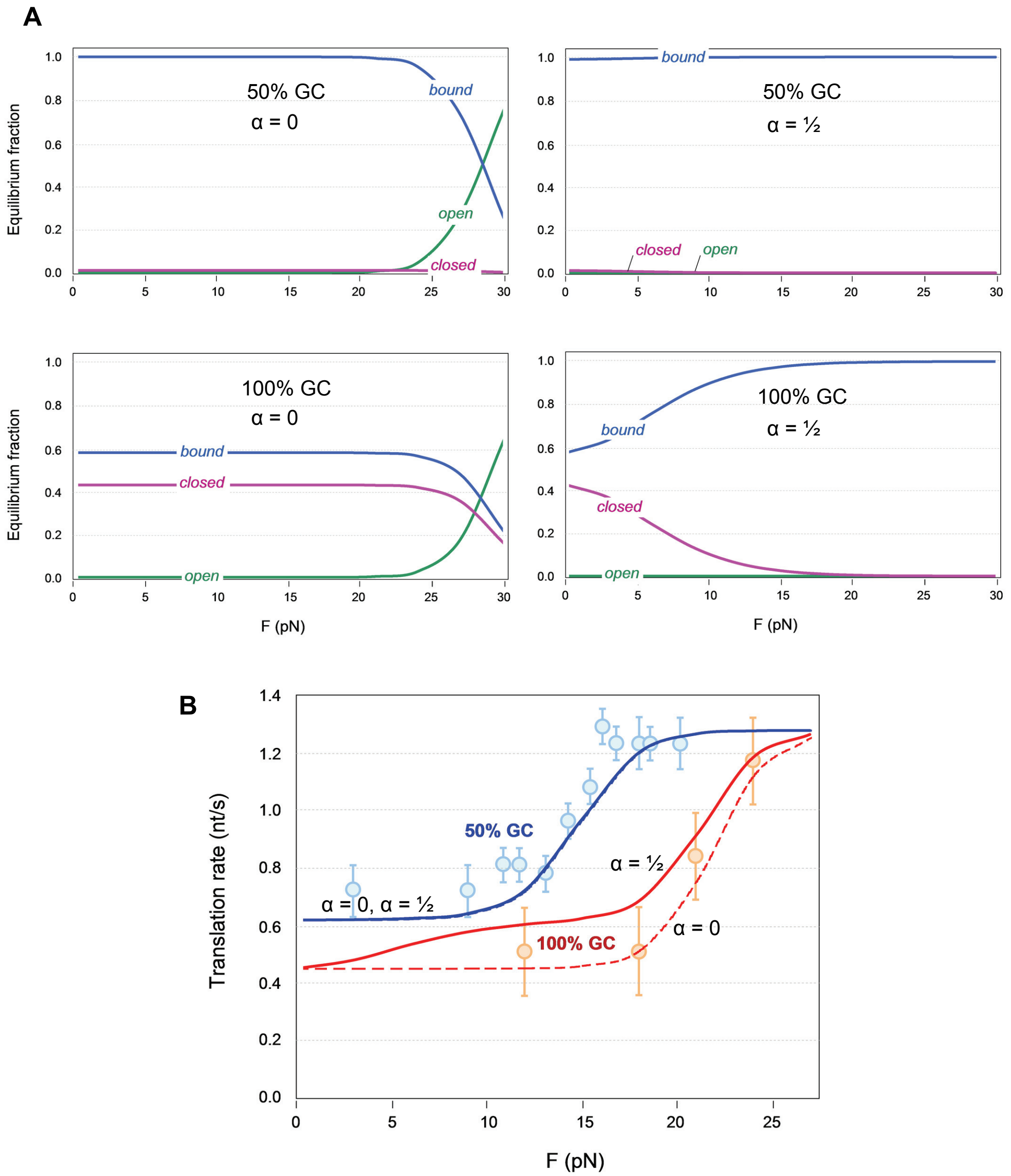

Figure 3.11. Position of the *proximal-bound* state along the extension coordinate. *A*. Effect of changing the position of the *bound* state of the proximal segment along the *closed*-*open* coordinate, denoted as α, from 0 (left graphs) to 0.5 (right graphs), on the probabilities of the *open*, *closed*, and *bound* states (green, purple, and blue curves, respectively) using the parameters of Fig. 3.6 for the 50% GC hairpin (top two graphs) and the 100% GC hairpin (bottom two graphs). *B*. Translation rates for 50% and

100% GC hairpins (blue and red curves, respectively) when the position of the *bound* state of the proximal segment along the *closed-open* coordinate, denoted as α, is 0 (dashed curves) or 0.5 (solid curves). The dashed and solid curves for the 50% GC hairpin overlap. The parameters are as in Fig. 3.6 except that k_{off}^{S3} is set to 1.2 nt/s for a better fit. Data points adapted from optical tweezers experiments (Qu et al., 2011) are shown.

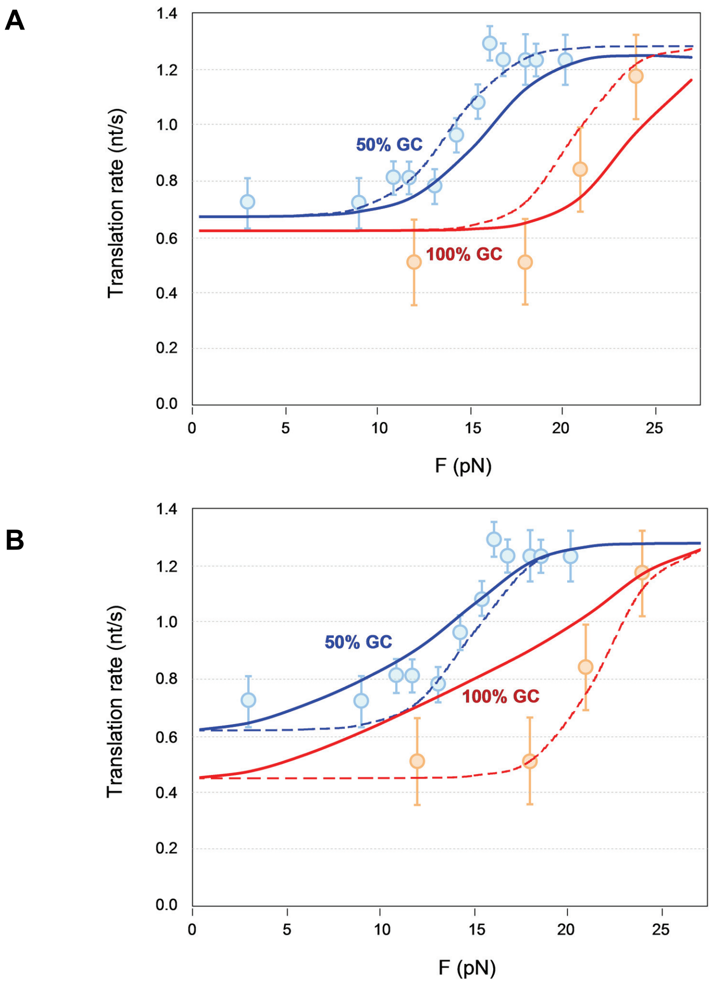

Figure 3.12. Force dependence of rate constants k_{on}^{S3} and k_{off}^{S3}. Effect of changing the force-dependence of k_{on}^{S3} and k_{off}^{S3} on the predicted translation rates for 50% GC hairpins (blue curves) and 100% GC hairpins (red curves). Solid and dashed curves correspond to force-dependence and force-independence assumptions, respectively. *A*. Setting k_{on}^{S3} to be force-dependent, i.e. $k_{on}^{S3}(F) = k_{off}^{S3}\exp(\Delta G_{binding} - \frac{1}{2}[FX_F - \Delta G_{stretch}])$, shifts the curves to the right, with no qualitative change. The parameters used are the same as those in Fig. 3.6, except that a $\Delta G_{binding}$ value of 5.7 k_BT is chosen for a better fit. *B*. Setting k_{off}^{S3} to be force-dependent, i.e. $k_{off}^{S3}(F) = k_{off}^{S3}(F=0)\cdot\exp(\frac{1}{2}[FX_F - \Delta G_{stretch}])$, qualitatively changes the curves. The parameters used are the same as those in Fig. 3.6, except that a k_{off}^{S3} value of 1.2 nt/s is chosen.

List of Supplementary Files

Supplementary File 1 – PDB format (atomic coordinates)

Crystal Structure of the *E. coli* 70S Ribosome in Complex with a Haripin-containing mRNA

The file includes the atomic coordinates and ADP parameters of non-hydrogen atoms and heteroatoms. It contains 109 polymer chains.

Supplementary File 2 – MTZ format (structure factors)

Diffraction Data for Crystal Structure of the *E. coli* 70S Ribosome in Complex with a Haripin-containing mRNA

This file lists scaled structure factor amplitudes used for structure determination. The resolution cutoff for the data is 3.2Å resolution. The free set (2%) is labeled.

Supplementary File 3 – MP4 format (video)

Schematic animation of the sliding and bypass routes

In this schematic animation, the sliding and bypass routes at the distal active site are shown to give an intuitive mechanical picture of these routes. The rates (fast and slow) in the animation are not to scale, and are meant for qualitative comparison only.

Supplementary File 4 – XLS format (spreadsheet)

Kinetic simulation spreadsheet

An electronic spreadsheet is provided containing two worksheets, one with the tandem active site model (Amiri), and the other with the model reproduced from Qu et al., 2011. Each worksheet contains a list of parameters highlighted in *green*, which can be modified to alter the force-dependence curves. A least squares sum is included for minimization purposes.

Bibliography

Adams, P.D., Afonine, P.V., Bunkóczi, G., Chen, V.B., Davis, I.W., Echols, N., Headd, J.J., Hung, L.-W., Kapral, G.J., Grosse-Kunstleve, R.W., et al. (2010). PHENIX: a comprehensive Python-based system for macromolecular structure solution. Acta Crystallogr. D Biol. Crystallogr. *66*, 213–221.

Agrawal, R.K., Heagle, A.B., Penczek, P., Grassucci, R.A., and Frank, J. (1999). EF-G-dependent GTP hydrolysis induces translocation accompanied by large conformational changes in the 70S ribosome. Nat. Struct. Biol. *6*, 643–647.

Agrawal, R.K., Sharma, M.R., Kiel, M.C., Hirokawa, G., Booth, T.M., Spahn, C.M.T., Grassucci, R.A., Kaji, A., and Frank, J. (2004). Visualization of ribosome-recycling factor on the Escherichia coli 70S ribosome: functional implications. Proc. Natl. Acad. Sci. U. S. A. *101*, 8900–8905.

Anderson, D.E., Becktel, W.J., and Dahlquist, F.W. (1990). pH-induced denaturation of proteins: a single salt bridge contributes 3-5 kcal/mol to the free energy of folding of T4 lysozyme. Biochemistry (Mosc.) *29*, 2403–2408.

Andreou, A.Z., and Klostermeier, D. (2013). The DEAD-box helicase eIF4A: paradigm or the odd one out? RNA Biol. *10*, 19–32.

Andronescu, M., Condon, A., Turner, D.H., and Mathews, D.H. (2014). The determination of RNA folding nearest neighbor parameters. Methods Mol. Biol. Clifton NJ *1097*, 45–70.

Ban, N., Nissen, P., Hansen, J., Moore, P.B., and Steitz, T.A. (2000). The complete atomic structure of the large ribosomal subunit at 2.4 A resolution. Science *289*, 905–920.

Ban, N., Beckmann, R., Cate, J.H.D., Dinman, J.D., Dragon, F., Ellis, S.R., Lafontaine, D.L.J., Lindahl, L., Liljas, A., Lipton, J.M., et al. (2014). A new system for naming ribosomal proteins. Curr. Opin. Struct. Biol. *24*, 165–169.

Baranov, P.V., Gesteland, R.F., and Atkins, J.F. (2002). Recoding: translational bifurcations in gene expression. Gene *286*, 187–201.

Barsky, D., Laurence, T.A., and Venclovas, Č. (2010). How Proteins Slide on DNA. In Biophysics of DNA-Protein Interactions, M.C. Williams, and L.J.M. III, eds. (Springer New York), pp. 39–68.

Belardinelli, R., Sharma, H., Caliskan, N., Cunha, C.E., Peske, F., Wintermeyer, W., and Rodnina, M.V. (2016). Choreography of molecular movements during ribosome progression along mRNA. Nat. Struct. Mol. Biol. *23*, 342–348.

Belitsina, N.V., Tnalina, G.Z., and Spirin, A.S. (1981). Template-free ribosomal synthesis of polylysine from lysyl-tRNA. FEBS Lett. *131*, 289–292.

Ben-Shem, A., Garreau de Loubresse, N., Melnikov, S., Jenner, L., Yusupova, G., and Yusupov, M. (2011). The structure of the eukaryotic ribosome at 3.0 Å resolution. Science *334*, 1524–1529.

Beran, R.K.F., Bruno, M.M., Bowers, H.A., Jankowsky, E., and Pyle, A.M. (2006). Robust translocation along a molecular monorail: the NS3 helicase from hepatitis C virus traverses unusually large disruptions in its track. J. Mol. Biol. *358*, 974–982.

Betterton, M.D., and Jülicher, F. (2005). Opening of nucleic-acid double strands by helicases: active versus passive opening. Phys. Rev. E Stat. Nonlin. Soft Matter Phys. *71*, 011904.

Beuth, B., Pennell, S., Arnvig, K.B., Martin, S.R., and Taylor, I.A. (2005). Structure of a Mycobacterium tuberculosis NusA-RNA complex. EMBO J. *24*, 3576–3587.

Beyer, D., Skripkin, E., Wadzack, J., and Nierhaus, K.H. (1994). How the ribosome moves along the mRNA during protein synthesis. J. Biol. Chem. *269*, 30713–30717.

Binshtein, E., and Ohi, M.D. (2015). Cryo-electron microscopy and the amazing race to atomic resolution. Biochemistry (Mosc.) *54*, 3133–3141.

Bockelmann, U., Essevaz-Roulet, B., and Heslot, F. (1997). Molecular Stick-Slip Motion Revealed by Opening DNA with Piconewton Forces. Phys. Rev. Lett. *79*, 4489–4492.

Bourgeois, C.F., Mortreux, F., and Auboeuf, D. (2016). The multiple functions of RNA helicases as drivers and regulators of gene expression. Nat. Rev. Mol. Cell Biol. *17*, 426–438.

Bowden, F.P., and Leben, L. (1939). The Nature of Sliding and the Analysis of Friction. Proc. R. Soc. Lond. Math. Phys. Eng. Sci. *169*, 371–391.

Brace, W.F., and Byerlee, J.D. (1966). Stick-slip as a mechanism for earthquakes. Science *153*, 990–992.

Brandt, F., Etchells, S.A., Ortiz, J.O., Elcock, A.H., Hartl, F.U., and Baumeister, W. (2009). The native 3D organization of bacterial polysomes. Cell *136*, 261–271.

Brennan, C.A., Dombroski, A.J., and Platt, T. (1987). Transcription termination factor rho is an RNA-DNA helicase. Cell *48*, 945–952.

Brierley, I. (1995). Ribosomal frameshifting viral RNAs. J. Gen. Virol. *76 (Pt 8)*, 1885–1892.

Caruthers, J.M., and McKay, D.B. (2002). Helicase structure and mechanism. Curr. Opin. Struct. Biol. *12*, 123–133.

Cech, T.R. (2000). The ribosome is a ribozyme. Science *289*, 878–879.

Chen, C., Zhang, H., Broitman, S.L., Reiche, M., Farrell, I., Cooperman, B.S., and Goldman, Y.E. (2013). Dynamics of translation by single ribosomes through mRNA secondary structures. Nat. Struct. Mol. Biol. *20*, 582–588.

Chen, C., Cui, X., Beausang, J.F., Zhang, H., Farrell, I., Cooperman, B.S., and Goldman, Y.E. (2016). Elongation factor G initiates translocation through a power stroke. Proc. Natl. Acad. Sci. U. S. A. *113*, 7515–7520.

Christensen, A.K., and Bourne, C.M. (1999). Shape of large bound polysomes in cultured fibroblasts and thyroid epithelial cells. Anat. Rec. *255*, 116–129.

Claude, A. (1943). THE CONSTITUTION OF PROTOPLASM. Science *97*, 451–456.

Cordin, O., Banroques, J., Tanner, N.K., and Linder, P. (2006). The DEAD-box protein family of RNA helicases. Gene *367*, 17–37.

Cornish, P.V., Ermolenko, D.N., Staple, D.W., Hoang, L., Hickerson, R.P., Noller, H.F., and Ha, T. (2009). Following movement of the L1 stalk between three functional states in single ribosomes. Proc. Natl. Acad. Sci. U. S. A. *106*, 2571–2576.

Crick, F. (1970). Central dogma of molecular biology. Nature *227*, 561–563.

Culver, G.M., and Noller, H.F. (2000). In vitro reconstitution of 30S ribosomal subunits using complete set of recombinant proteins. Methods Enzymol. *318*, 446–460.

Diaconu, M., Kothe, U., Schlünzen, F., Fischer, N., Harms, J.M., Tonevitsky, A.G., Stark, H., Rodnina, M.V., and Wahl, M.C. (2005). Structural basis for the function of the ribosomal L7/12 stalk in factor binding and GTPase activation. Cell *121*, 991–1004.

DiCarlo, J.E., Norville, J.E., Mali, P., Rios, X., Aach, J., and Church, G.M. (2013). Genome engineering in Saccharomyces cerevisiae using CRISPR-Cas systems. Nucleic Acids Res. *41*, 4336–4343.

Dong, J., Aitken, C.E., Thakur, A., Shin, B.-S., Lorsch, J.R., and Hinnebusch, A.G. (2017). Rps3/uS3 promotes mRNA binding at the 40S ribosome entry channel and stabilizes preinitiation complexes at start codons. Proc. Natl. Acad. Sci. U. S. A. *114*, E2126–E2135.

Doty, P., Boedtker, H., Fresco, J.R., Haselkorn, R., and Litt, M. (1959). SECONDARY STRUCTURE IN RIBONUCLEIC ACIDS. Proc. Natl. Acad. Sci. U. S. A. *45*, 482–499.

Duncan, R., and Hershey, J.W. (1983). Identification and quantitation of levels of protein synthesis initiation factors in crude HeLa cell lysates by two-dimensional polyacrylamide gel electrophoresis. J. Biol. Chem. *258*, 7228–7235.

Dunkle, J.A., and Cate, J.H.D. (2011). The packing of ribosomes in crystals and polysomes. In Ribosomes, M.V. Rodnina, W. Wintermeyer, and R. Green, eds. (Springer Vienna), pp. 65–73.

Dunkle, J.A., Wang, L., Feldman, M.B., Pulk, A., Chen, V.B., Kapral, G.J., Noeske, J., Richardson, J.S., Blanchard, S.C., and Cate, J.H.D. (2011). Structures of the bacterial ribosome in classical and hybrid states of tRNA binding. Science *332*, 981–984.

Emsley, P., Lohkamp, B., Scott, W.G., and Cowtan, K. (2010). Features and development of Coot. Acta Crystallogr. D Biol. Crystallogr. *66*, 486–501.

Ermolenko, D.N., and Noller, H.F. (2011). mRNA translocation occurs during the second step of ribosomal intersubunit rotation. Nat. Struct. Mol. Biol. *18*, 457–462.

Fagan, C.E., Dunkle, J.A., Maehigashi, T., Dang, M.N., Devaraj, A., Miles, S.J., Qin, D., Fredrick, K., and Dunham, C.M. (2013). Reorganization of an intersubunit bridge induced by disparate 16S ribosomal ambiguity mutations mimics an EF-Tu-bound state. Proc. Natl. Acad. Sci. U. S. A. *110*, 9716–9721.

Fierro-Monti, I., and Mathews, M.B. (2000). Proteins binding to duplexed RNA: one motif, multiple functions. Trends Biochem. Sci. *25*, 241–246.

Finer-Moore, J.S., Fauman, E.B., Morse, R.J., Santi, D.V., and Stroud, R.M. (1996). Contribution of a salt bridge to binding affinity and dUMP orientation to catalytic rate: mutation of a substrate-binding arginine in thymidylate synthase. Protein Eng. *9*, 69–75.

Fischer, N., Konevega, A.L., Wintermeyer, W., Rodnina, M.V., and Stark, H. (2010). Ribosome dynamics and tRNA movement by time-resolved electron cryomicroscopy. Nature *466*, 329–333.

Fischer, N., Neumann, P., Bock, L.V., Maracci, C., Wang, Z., Paleskava, A., Konevega, A.L., Schröder, G.F., Grubmüller, H., Ficner, R., et al. (2016). The pathway to GTPase activation of elongation factor SelB on the ribosome. Nature *540*, 80–85.

Fox, G.E., and Woese, C.R. (1975). 5S RNA secondary structure. Nature *256*, 505–507.

Frank, J., and Agrawal, R.K. (2000). A ratchet-like inter-subunit reorganization of the ribosome during translocation. Nature *406*, 318–322.

Frank, J., Zhu, J., Penczek, P., Li, Y., Srivastava, S., Verschoor, A., Radermacher, M., Grassucci, R., Lata, R.K., and Agrawal, R.K. (1995). A model of protein synthesis based on cryo-electron microscopy of the E. coli ribosome. Nature *376*, 441–444.

Fredrick, K., and Noller, H.F. (2003). Catalysis of ribosomal translocation by sparsomycin. Science *300*, 1159–1162.

Freistroffer, D.V., Pavlov, M.Y., MacDougall, J., Buckingham, R.H., and Ehrenberg, M. (1997). Release factor RF3 in E.coli accelerates the dissociation of release factors RF1 and RF2 from the ribosome in a GTP-dependent manner. EMBO J. *16*, 4126–4133.

Gamow, G. (1954). Possible Relation between Deoxyribonucleic Acid and Protein Structures. Nature *173*, 318–318.

Gao, Y.-G., Selmer, M., Dunham, C.M., Weixlbaumer, A., Kelley, A.C., and Ramakrishnan, V. (2009). The Structure of the Ribosome with Elongation Factor G Trapped in the Posttranslocational State. Science *326*, 694–699.

Gavrilova, L.P., Kostiashkina, O.E., Koteliansky, V.E., Rutkevitch, N.M., and Spirin, A.S. (1976). Factor-free ("non-enzymic") and factor-dependent systems of translation of polyuridylic acid by Escherichia coli ribosomes. J. Mol. Biol. *101*, 537–552.

Giedroc, D.P., and Cornish, P.V. (2009). Frameshifting RNA pseudoknots: structure and mechanism. Virus Res. *139*, 193–208.

Gilbert, W. (1986). Origin of life: The RNA world. Nature *319*, 618–618.

Gorochowski, T.E., Ignatova, Z., Bovenberg, R.A.L., and Roubos, J.A. (2015). Trade-offs between tRNA abundance and mRNA secondary structure support smoothing of translation elongation rate. Nucleic Acids Res. *43*, 3022–3032.

Grishin, N.V. (2001). KH domain: one motif, two folds. Nucleic Acids Res. *29*, 638–643.

Gualerzi, C.O., Brandi, L., Caserta, E., Garofalo, C., Lammi, M., La Teana, A., Petrelli, D., Spurio, R., Tomsic, J., and Pon, C.L. (2001). Initiation factors in the early events of mRNA translation in bacteria. Cold Spring Harb. Symp. Quant. Biol. *66*, 363–376.

Guo, Z., and Noller, H.F. (2012). Rotation of the head of the 30S ribosomal subunit during mRNA translocation. Proc. Natl. Acad. Sci. U. S. A. *109*, 20391–20394.

Hartz, D., McPheeters, D.S., Traut, R., and Gold, L. (1988). Extension inhibition analysis of translation initiation complexes. Methods Enzymol. *164*, 419–425.

Herr, A.J., Nelson, C.C., Wills, N.M., Gesteland, R.F., and Atkins, J.F. (2001). Analysis of the roles of tRNA structure, ribosomal protein L9, and the bacteriophage T4 gene 60 bypassing signals during ribosome slippage on mRNA. J. Mol. Biol. *309*, 1029–1048.

von Hippel, P.H., and Berg, O.G. (1989). Facilitated target location in biological systems. J. Biol. Chem. *264*, 675–678.

Hirokawa, G., Kiel, M.C., Muto, A., Selmer, M., Raj, V.S., Liljas, A., Igarashi, K., Kaji, H., and Kaji, A. (2002). Post-termination complex disassembly by ribosome recycling factor, a functional tRNA mimic. EMBO J. *21*, 2272–2281.

Holder, J.W., and Lingrel, J.B. (1975). Determination of secondary structure in rabbit globin messenger RNA by thermal denaturation. Biochemistry (Mosc.) *14*, 4209–4215.

Hopfield, J.J. (1974). Kinetic proofreading: a new mechanism for reducing errors in biosynthetic processes requiring high specificity. Proc. Natl. Acad. Sci. U. S. A. *71*, 4135–4139.

Horan, L.H., and Noller, H.F. (2007). Intersubunit movement is required for ribosomal translocation. Proc. Natl. Acad. Sci. U. S. A. *104*, 4881–4885.

Hüttenhofer, A., and Noller, H.F. (1994). Footprinting mRNA-ribosome complexes with chemical probes. EMBO J. *13*, 3892–3901.

Inoue-Yokosawa, N., Ishikawa, C., and Kaziro, Y. (1974). The role of guanosine triphosphate in translocation reaction catalyzed by elongation factor G. J. Biol. Chem. *249*, 4321–4323.

Jackson, R.J., Hellen, C.U.T., and Pestova, T.V. (2010). The mechanism of eukaryotic translation initiation and principles of its regulation. Nat. Rev. Mol. Cell Biol. *11*, 113–127.

Jankowsky, E. (2011). RNA helicases at work: binding and rearranging. Trends Biochem. Sci. *36*, 19–29.

Jarmoskaite, I., and Russell, R. (2011). DEAD-box proteins as RNA helicases and chaperones. Wiley Interdiscip. Rev. RNA *2*, 135–152.

Jayachandran, U., Grey, H., and Cook, A.G. (2016). Nuclear factor 90 uses an ADAR2-like binding mode to recognize specific bases in dsRNA. Nucleic Acids Res. *44*, 1924–1936.

Jeltsch, A., and Urbanke, C. (2004). Sliding or Hopping? How Restriction Enzymes Find Their Way on DNA. In Restriction Endonucleases, P.D.A.M. Pingoud, ed. (Springer Berlin Heidelberg), pp. 95–110.

Jenner, L.B., Demeshkina, N., Yusupova, G., and Yusupov, M. (2010). Structural aspects of messenger RNA reading frame maintenance by the ribosome. Nat. Struct. Mol. Biol. *17*, 555–560.

Jin, H., Kelley, A.C., and Ramakrishnan, V. (2011). Crystal structure of the hybrid state of ribosome in complex with the guanosine triphosphatase release factor 3. Proc. Natl. Acad. Sci. U. S. A. *108*, 15798–15803.

Joseph, S., and Noller, H.F. (1998). EF-G-catalyzed translocation of anticodon stem-loop analogs of transfer RNA in the ribosome. EMBO J. *17*, 3478–3483.

Kabsch, W. (2010). XDS. Acta Crystallogr. D Biol. Crystallogr. *66*, 125–132.

Kafri, M., Metzl-Raz, E., Jona, G., and Barkai, N. (2016). The Cost of Protein Production. Cell Rep. *14*, 22–31.

Kaminishi, T., Wilson, D.N., Takemoto, C., Harms, J.M., Kawazoe, M., Schluenzen, F., Hanawa-Suetsugu, K., Shirouzu, M., Fucini, P., and Yokoyama, S. (2007). A Snapshot of the 30S Ribosomal Subunit Capturing mRNA via the Shine-Dalgarno Interaction. Structure *15*, 289–297.

Katunin, V.I., Savelsbergh, A., Rodnina, M.V., and Wintermeyer, W. (2002). Coupling of GTP hydrolysis by elongation factor G to translocation and factor recycling on the ribosome. Biochemistry (Mosc.) *41*, 12806–12812.

Kertesz, M., Wan, Y., Mazor, E., Rinn, J.L., Nutter, R.C., Chang, H.Y., and Segal, E. (2010). Genome-wide measurement of RNA secondary structure in yeast. Nature *467*, 103–107.

Korostelev, A., Ermolenko, D.N., and Noller, H.F. (2008). Structural dynamics of the ribosome. Curr. Opin. Chem. Biol. *12*, 674–683.

Kozak, M. (1983). Comparison of initiation of protein synthesis in procaryotes, eucaryotes, and organelles. Microbiol. Rev. *47*, 1–45.

Krylov, S.Y., and Frenken, J.W.M. (2014). The physics of atomic-scale friction: Basic considerations and open questions. Phys. Status Solidi B *251*, 711–736.

Kunkel, T.A., Roberts, J.D., and Zakour, R.A. (1987). Rapid and efficient site-specific mutagenesis without phenotypic selection. Methods Enzymol. *154*, 367–382.

Laurberg, M., Asahara, H., Korostelev, A., Zhu, J., Trakhanov, S., and Noller, H.F. (2008). Structural basis for translation termination on the 70S ribosome. Nature *454*, 852–857.

Laursen, B.S., Sørensen, H.P., Mortensen, K.K., and Sperling-Petersen, H.U. (2005). Initiation of protein synthesis in bacteria. Microbiol. Mol. Biol. Rev. MMBR *69*, 101–123.

Lim, V., Venclovas, C., Spirin, A., Brimacombe, R., Mitchell, P., and Müller, F. (1992). How are tRNAs and mRNA arranged in the ribosome? An attempt to correlate the stereochemistry of the tRNA-mRNA interaction with constraints imposed by the ribosomal topography. Nucleic Acids Res. *20*, 2627–2637.

Linder, P., and Jankowsky, E. (2011). From unwinding to clamping — the DEAD box RNA helicase family. Nat. Rev. Mol. Cell Biol. *12*, 505–516.

Linder, P., Lasko, P.F., Ashburner, M., Leroy, P., Nielsen, P.J., Nishi, K., Schnier, J., and Slonimski, P.P. (1989). Birth of the D-E-A-D box. Nature *337*, 121–122.

Lingelbach, K., and Dobberstein, B. (1988). An extended RNA/RNA duplex structure within the coding region of mRNA does not block translational elongation. Nucleic Acids Res. *16*, 3405–3414.

Liu, Q., and Fredrick, K. (2016). Intersubunit Bridges of the Bacterial Ribosome. J. Mol. Biol. *428*, 2146–2164.

Liu, G., Song, G., Zhang, D., Zhang, D., Li, Z., Lyu, Z., Dong, J., Achenbach, J., Gong, W., Zhao, X.S., et al. (2014a). EF-G catalyzes tRNA translocation by disrupting interactions between decoding center and codon-anticodon duplex. Nat. Struct. Mol. Biol. *21*, 817–824.

Liu, T., Kaplan, A., Alexander, L., Yan, S., Wen, J.-D., Lancaster, L., Wickersham, C.E., Fredrick, K., Fredrik, K., Noller, H., et al. (2014b). Direct measurement of the mechanical work during translocation by the ribosome. eLife *3*, e03406.

Lohman, T.M., and Bjornson, K.P. (1996). Mechanisms of helicase-catalyzed DNA unwinding. Annu. Rev. Biochem. *65*, 169–214.

Mahen, E.M., Watson, P.Y., Cottrell, J.W., and Fedor, M.J. (2010). mRNA secondary structures fold sequentially but exchange rapidly in vivo. PLoS Biol. *8*, e1000307.

Manosas, M., Xi, X.G., Bensimon, D., and Croquette, V. (2010). Active and passive mechanisms of helicases. Nucleic Acids Res. *38*, 5518–5526.

Maracci, C., and Rodnina, M.V. (2016). Review: Translational GTPases. Biopolymers *105*, 463–475.

Martin, R., Straub, A.U., Doebele, C., and Bohnsack, M.T. (2013). DExD/H-box RNA helicases in ribosome biogenesis. RNA Biol. *10*, 4–18.

McMullen, D.W., Jaskunas, S.R., and Tinoco, I. (1967). Application of matrix rank analysis to the optical rotatory dispersion of TMV RNA. Biopolymers *5*, 589–613.

Milo, R., and Phillips, R. (2016). Cell biology by the numbers.

Min Jou, W., Haegeman, G., Ysebaert, M., and Fiers, W. (1972). Nucleotide sequence of the gene coding for the bacteriophage MS2 coat protein. Nature *237*, 82–88.

Moazed, D., and Noller, H.F. (1989a). Interaction of tRNA with 23S rRNA in the ribosomal A, P, and E sites. Cell *57*, 585–597.

Moazed, D., and Noller, H.F. (1989b). Intermediate states in the movement of transfer RNA in the ribosome. Nature *342*, 142–148.

Moazed, D., and Noller, H.F. (1990). Binding of tRNA to the ribosomal A and P sites protects two distinct sets of nucleotides in 16 S rRNA. J. Mol. Biol. *211*, 135–145.

Mohammad, F., Woolstenhulme, C.J., Green, R., and Buskirk, A.R. (2016). Clarifying the translational pausing landscape in bacteria by ribosome profiling. Cell Rep. *14*, 686–694.

Mohan, S., and Noller, H.F. (2017). Recurring RNA structural motifs underlie the mechanics of L1 stalk movement. Nat. Commun. *8*, 14285.

Mohan, S., Donohue, J.P., and Noller, H.F. (2014). Molecular mechanics of 30S subunit head rotation. Proc. Natl. Acad. Sci. *111*, 13325–13330.

Morozova, N., Allers, J., Myers, J., and Shamoo, Y. (2006). Protein–RNA interactions: exploring binding patterns with a three-dimensional superposition analysis of high resolution structures. Bioinformatics *22*, 2746–2752.

Murshudov, G.N., Vagin, A.A., and Dodson, E.J. (1997). Refinement of macromolecular structures by the maximum-likelihood method. Acta Crystallogr. D Biol. Crystallogr. *53*, 240–255.

Namy, O., Rousset, J.-P., Napthine, S., and Brierley, I. (2004). Reprogrammed genetic decoding in cellular gene expression. Mol. Cell *13*, 157–168.

Nelson, E.M., Li, H., and Timp, G. (2014). Direct, concurrent measurements of the forces and currents affecting DNA in a nanopore with comparable topography. ACS Nano *8*, 5484–5493.

Nirenberg, M.W., and Matthaei, J.H. (1961). The dependence of cell-free protein synthesis in E. coli upon naturally occurring or synthetic polyribonucleotides. Proc. Natl. Acad. Sci. U. S. A. *47*, 1588–1602.

Noeske, J., Wasserman, M.R., Terry, D.S., Altman, R.B., Blanchard, S.C., and Cate, J.H.D. (2015). High-resolution structure of the Escherichia coli ribosome. Nat. Struct. Mol. Biol. *22*, 336–341.

Noller, H.F. (2012). Evolution of Protein Synthesis from an RNA World. Cold Spring Harb. Perspect. Biol. *4*.

Noller, H.F. (2017). The parable of the caveman and the Ferrari: protein synthesis and the RNA world. Philos. Trans. R. Soc. Lond. B. Biol. Sci. *372*.

Noller, H.F., and Woese, C.R. (1981). Secondary structure of 16S ribosomal RNA. Science *212*, 403–411.

Noller, H.F., Kop, J., Wheaton, V., Brosius, J., Gutell, R.R., Kopylov, A.M., Dohme, F., Herr, W., Stahl, D.A., Gupta, R., et al. (1981). Secondary structure model for 23S ribosomal RNA. Nucleic Acids Res. *9*, 6167–6189.

Ogle, J.M., Brodersen, D.E., Clemons, W.M., Tarry, M.J., Carter, A.P., and Ramakrishnan, V. (2001). Recognition of cognate transfer RNA by the 30S ribosomal subunit. Science *292*, 897–902.

Ogle, J.M., Murphy, F.V., Tarry, M.J., and Ramakrishnan, V. (2002). Selection of tRNA by the ribosome requires a transition from an open to a closed form. Cell *111*, 721–732.

Parsyan, A., Svitkin, Y., Shahbazian, D., Gkogkas, C., Lasko, P., Merrick, W.C., and Sonenberg, N. (2011). mRNA helicases: the tacticians of translational control. Nat. Rev. Mol. Cell Biol. *12*, 235–245.

Patel, S.S., and Donmez, I. (2006). Mechanisms of Helicases. J. Biol. Chem. *281*, 18265–18268.

Peske, F., Rodnina, M.V., and Wintermeyer, W. (2005). Sequence of steps in ribosome recycling as defined by kinetic analysis. Mol. Cell *18*, 403–412.

Pestka, S. (1969). Studies on the formation of transfer ribonucleic acid-ribosome complexes. VI. Oligopeptide synthesis and translocation on ribosomes in the presence and absence of soluble transfer factors. J. Biol. Chem. *244*, 1533–1539.

Petrosyan, R. (2017). Improved approximations for some polymer extension models. Rheol. Acta *56*, 21–26.

Phelps, S.S., Gaudin, C., Yoshizawa, S., Benitez, C., Fourmy, D., and Joseph, S. (2006). Translocation of a tRNA with an extended anticodon through the ribosome. J. Mol. Biol. *360*, 610–622.

Popov, V.L., and Gray, J. a. T. (2014). Prandtl-Tomlinson Model: A Simple Model Which Made History. In The History of Theoretical, Material and Computational Mechanics - Mathematics Meets Mechanics and Engineering, E. Stein, ed. (Springer Berlin Heidelberg), pp. 153–168.

Pyle, A.M. (2008). Translocation and unwinding mechanisms of RNA and DNA helicases. Annu. Rev. Biophys. *37*, 317–336.

Qin, P., Yu, D., Zuo, X., and Cornish, P.V. (2014). Structured mRNA induces the ribosome into a hyper-rotated state. EMBO Rep. *15*, 185–190.

Qu, X., Wen, J.-D., Lancaster, L., Noller, H.F., Bustamante, C., and Tinoco, I. (2011). The ribosome uses two active mechanisms to unwind messenger RNA during translation. Nature *475*, 118–121.

Qu, X., Lancaster, L., Noller, H.F., Bustamante, C., and Tinoco, I. (2012). Ribosomal protein S1 unwinds double-stranded RNA in multiple steps. Proc. Natl. Acad. Sci. U. S. A. *109*, 14458–14463.

Rabl, J., Leibundgut, M., Ataide, S.F., Haag, A., and Ban, N. (2011). Crystal structure of the eukaryotic 40S ribosomal subunit in complex with initiation factor 1. Science *331*, 730–736.

Ramrath, D.J.F., Lancaster, L., Sprink, T., Mielke, T., Loerke, J., Noller, H.F., and Spahn, C.M.T. (2013). Visualization of two transfer RNAs trapped in transit during elongation factor G-mediated translocation. Proc. Natl. Acad. Sci. U. S. A. *110*, 20964–20969.

Ratje, A.H., Loerke, J., Mikolajka, A., Brünner, M., Hildebrand, P.W., Starosta, A.L., Dönhöfer, A., Connell, S.R., Fucini, P., Mielke, T., et al. (2010). Head swivel on the ribosome facilitates translocation by means of intra-subunit tRNA hybrid sites. Nature *468*, 713–716.

Riddle, D.L., and Carbon, J. (1973). Frameshift suppression: a nucleotide addition in the anticodon of a glycine transfer RNA. Nature. New Biol. *242*, 230–234.

Roberts, R.B. (Richard B. (1958). Microsomal particles and protein synthesis; papers presented at the First Symposium of the Biophysical Society, at the Massachusetts Institute of Technology, Cambridge, February 5, 6, and 8, 1958 (New York, Published on behalf of the Washington Academy of Sciences, Washington, D.C., by Pergamon Press).

Rocak, S., and Linder, P. (2004). DEAD-box proteins: the driving forces behind RNA metabolism. Nat. Rev. Mol. Cell Biol. *5*, 232–241.

Rodnina, M.V., Savelsbergh, A., Katunin, V.I., and Wintermeyer, W. (1997). Hydrolysis of GTP by elongation factor G drives tRNA movement on the ribosome. Nature *385*, 37–41.

Rouskin, S., Zubradt, M., Washietl, S., Kellis, M., and Weissman, J.S. (2014). Genome-wide probing of RNA structure reveals active unfolding of mRNA structures in vivo. Nature *505*, 701–705.

Rozov, A., Demeshkina, N., Westhof, E., Yusupov, M., and Yusupova, G. (2015). Structural insights into the translational infidelity mechanism. Nat. Commun. *6*, 7251.

Rozov, A., Demeshkina, N., Khusainov, I., Westhof, E., Yusupov, M., and Yusupova, G. (2016a). Novel base-pairing interactions at the tRNA wobble position crucial for accurate reading of the genetic code. Nat. Commun. *7*, 10457.

Rozov, A., Westhof, E., Yusupov, M., and Yusupova, G. (2016b). The ribosome prohibits the G•U wobble geometry at the first position of the codon-anticodon helix. Nucleic Acids Res. *44*, 6434–6441.

Sahu, B., Khade, P.K., and Joseph, S. (2013). Highly conserved base A55 of 16S ribosomal RNA is important for the elongation cycle of protein synthesis. Biochemistry (Mosc.) *52*, 6695–6701.

Savelsbergh, A., Katunin, V.I., Mohr, D., Peske, F., Rodnina, M.V., and Wintermeyer, W. (2003). An elongation factor G-induced ribosome rearrangement precedes tRNA-mRNA translocation. Mol. Cell *11*, 1517–1523.

Schuette, J.-C., Murphy, F.V., Kelley, A.C., Weir, J.R., Giesebrecht, J., Connell, S.R., Loerke, J., Mielke, T., Zhang, W., Penczek, P.A., et al. (2009). GTPase activation of elongation factor EF-Tu by the ribosome during decoding. EMBO J. *28*, 755–765.

Schuwirth, B.S., Borovinskaya, M.A., Hau, C.W., Zhang, W., Vila-Sanjurjo, A., Holton, J.M., and Cate, J.H.D. (2005). Structures of the bacterial ribosome at 3.5 A resolution. Science *310*, 827–834.

Schuwirth, B.S., Day, J.M., Hau, C.W., Janssen, G.R., Dahlberg, A.E., Cate, J.H.D., and Vila-Sanjurjo, A. (2006). Structural analysis of kasugamycin inhibition of translation. Nat. Struct. Mol. Biol. *13*, 879–886.

Selmer, M., Dunham, C.M., Murphy, F.V., Weixlbaumer, A., Petry, S., Kelley, A.C., Weir, J.R., and Ramakrishnan, V. (2006). Structure of the 70S ribosome complexed with mRNA and tRNA. Science *313*, 1935–1942.

Sengoku, T., Nureki, O., Nakamura, A., Kobayashi, S., and Yokoyama, S. (2006). Structural basis for RNA unwinding by the DEAD-box protein Drosophila Vasa. Cell *125*, 287–300.

Shine, J., and Dalgarno, L. (1974). The 3'-terminal sequence of Escherichia coli 16S ribosomal RNA: complementarity to nonsense triplets and ribosome binding sites. Proc. Natl. Acad. Sci. U. S. A. *71*, 1342–1346.

Shoji, S., Dambacher, C.M., Shajani, Z., Williamson, J.R., and Schultz, P.G. (2011). Systematic chromosomal deletion of bacterial ribosomal protein genes. J. Mol. Biol. *413*, 751–761.

Sievers, A., Beringer, M., Rodnina, M.V., and Wolfenden, R. (2004). The ribosome as an entropy trap. Proc. Natl. Acad. Sci. U. S. A. *101*, 7897–7901.

Singleton, M.R., Dillingham, M.S., and Wigley, D.B. (2007). Structure and Mechanism of Helicases and Nucleic Acid Translocases. Annu. Rev. Biochem. *76*, 23–50.

Sørensen, M.A., Kurland, C.G., and Pedersen, S. (1989). Codon usage determines translation rate in Escherichia coli. J. Mol. Biol. *207*, 365–377.

Spiegel, P.C., Ermolenko, D.N., and Noller, H.F. (2007). Elongation factor G stabilizes the hybrid-state conformation of the 70S ribosome. RNA N. Y. N *13*, 1473–1482.

Spirin, A.S. (2009). The Ribosome as a Conveying Thermal Ratchet Machine. J. Biol. Chem. *284*, 21103–21119.

Spitale, R.C., Flynn, R.A., Zhang, Q.C., Crisalli, P., Lee, B., Jung, J.-W., Kuchelmeister, H.Y., Batista, P.J., Torre, E.A., Kool, E.T., et al. (2015). Structural imprints in vivo decode RNA regulatory mechanisms. Nature *519*, 486–490.

Stanley, R.E., Blaha, G., Grodzicki, R.L., Strickler, M.D., and Steitz, T.A. (2010). The structures of the anti-tuberculosis antibiotics viomycin and capreomycin bound to the 70S ribosome. Nat. Struct. Mol. Biol. *17*, 289–293.

Steitz, J.A. (1969). Polypeptide chain initiation: nucleotide sequences of the three ribosomal binding sites in bacteriophage R17 RNA. Nature *224*, 957–964.

Studer, S.M., Feinberg, J.S., and Joseph, S. (2003). Rapid kinetic analysis of EF-G-dependent mRNA translocation in the ribosome. J. Mol. Biol. *327*, 369–381.

Takyar, S., Hickerson, R.P., and Noller, H.F. (2005). mRNA helicase activity of the ribosome. Cell *120*, 49–58.

Tholstrup, J., Oddershede, L.B., and Sørensen, M.A. (2012). mRNA pseudoknot structures can act as ribosomal roadblocks. Nucleic Acids Res. *40*, 303–313.

Tinoco, I. (2004). Force as a Useful Variable in Reactions: Unfolding RNA. Annu. Rev. Biophys. Biomol. Struct. *33*, 363–385.

Tinoco, I., and Bustamante, C. (2002). The effect of force on thermodynamics and kinetics of single molecule reactions. Biophys. Chem. *101–102*, 513–533.

Tinoco, I., Borer, P.N., Dengler, B., Levine, M.D., Uhlenbeck, O.C., Crothers, D.M., and Gralla, J. (1973). Improved Estimation of Secondary Structure in Ribonucleic Acids. Nature *246*, 40–41.

Tissières, A., Watson, J.D., Schlessinger, D., and Hollingworth, B.R. (1959). Ribonucleoprotein particles from Escherichia coli. J. Mol. Biol. *1*, 221–233.

Trabuco, L.G., Schreiner, E., Eargle, J., Cornish, P., Ha, T., Luthey-Schulten, Z., and Schulten, K. (2010). The role of L1 stalk-tRNA interaction in the ribosome elongation cycle. J. Mol. Biol. *402*, 741–760.

Valle, M., Zavialov, A., Sengupta, J., Rawat, U., Ehrenberg, M., and Frank, J. (2003). Locking and unlocking of ribosomal motions. Cell *114*, 123–134.

Valverde, R., Edwards, L., and Regan, L. (2008). Structure and function of KH domains. FEBS J. *275*, 2712–2726.

Voorhees, R.M., Weixlbaumer, A., Loakes, D., Kelley, A.C., and Ramakrishnan, V. (2009). Insights into substrate stabilization from snapshots of the peptidyl transferase center of the intact 70S ribosome. Nat. Struct. Mol. Biol. *16*, 528–533.

Warner, J.R. (1999). The economics of ribosome biosynthesis in yeast. Trends Biochem. Sci. *24*, 437–440.

Watts, J.M., Dang, K.K., Gorelick, R.J., Leonard, C.W., Bess, J.W., Swanstrom, R., Burch, C.L., and Weeks, K.M. (2009). Architecture and secondary structure of an entire HIV-1 RNA genome. Nature *460*, 711–716.

Wen, J.-D., Lancaster, L., Hodges, C., Zeri, A.-C., Yoshimura, S.H., Noller, H.F., Bustamante, C., and Tinoco, I. (2008). Following translation by single ribosomes one codon at a time. Nature *452*, 598–603.

Wilson, D.N. (2014). Ribosome-targeting antibiotics and mechanisms of bacterial resistance. Nat. Rev. Microbiol. *12*, 35–48.

Wilson, D.N., and Doudna Cate, J.H. (2012). The structure and function of the eukaryotic ribosome. Cold Spring Harb. Perspect. Biol. *4*.

Wimberly, B.T., Brodersen, D.E., Clemons, W.M., Morgan-Warren, R.J., Carter, A.P., Vonrhein, C., Hartsch, T., and Ramakrishnan, V. (2000). Structure of the 30S ribosomal subunit. Nature *407*, 327–339.

Winn, M.D., Ballard, C.C., Cowtan, K.D., Dodson, E.J., Emsley, P., Evans, P.R., Keegan, R.M., Krissinel, E.B., Leslie, A.G.W., McCoy, A., et al. (2011). Overview of the CCP4 suite and current developments. Acta Crystallogr. D Biol. Crystallogr. *67*, 235–242.

Woese, C.R. (1967). The genetic code: the molecular basis for genetic expression (New York: Harper & Row).

Woese, C.R., Kandler, O., and Wheelis, M.L. (1990). Towards a natural system of organisms: proposal for the domains Archaea, Bacteria, and Eucarya. Proc. Natl. Acad. Sci. U. S. A. *87*, 4576–4579.

Wohlgemuth, I., Pohl, C., Mittelstaet, J., Konevega, A.L., and Rodnina, M.V. (2011). Evolutionary optimization of speed and accuracy of decoding on the ribosome. Philos. Trans. R. Soc. B Biol. Sci. *366*, 2979–2986.

Wohlgemuth, S.E., Gorochowski, T.E., and Roubos, J.A. (2013). Translational sensitivity of the Escherichia coli genome to fluctuating tRNA availability. Nucleic Acids Res. *41*, 8021–8033.

Wool, I.G. (1996). Extraribosomal functions of ribosomal proteins. Trends Biochem. Sci. *21*, 164–165.

Wool, I.G., Chan, Y.L., and Glück, A. (1995). Structure and evolution of mammalian ribosomal proteins. Biochem. Cell Biol. Biochim. Biol. Cell. *73*, 933–947.

Xia, T., SantaLucia, J., Burkard, M.E., Kierzek, R., Schroeder, S.J., Jiao, X., Cox, C., and Turner, D.H. (1998). Thermodynamic parameters for an expanded nearest-neighbor model for formation of RNA duplexes with Watson-Crick base pairs. Biochemistry (Mosc.) *37*, 14719–14735.

Yan, S., Wen, J.-D., Bustamante, C., and Tinoco, I. (2015). Ribosome excursions during mRNA translocation mediate broad branching of frameshift pathways. Cell *160*, 870–881.

Yusupova, G., Jenner, L., Rees, B., Moras, D., and Yusupov, M. (2006). Structural basis for messenger RNA movement on the ribosome. Nature *444*, 391–394.

Yusupova, G.Z., Yusupov, M.M., Cate, J.H., and Noller, H.F. (2001). The path of messenger RNA through the ribosome. Cell *106*, 233–241.

Zhang, X., Lai, M., Chang, W., Yu, I., Ding, K., Mrazek, J., Ng, H.L., Yang, O.O., Maslov, D.A., and Zhou, Z.H. (2016). Structures and stabilization of kinetoplastid-specific split rRNAs revealed by comparing leishmanial and human ribosomes. Nat. Commun. *7*, 13223.

Zhou, J., Lancaster, L., Trakhanov, S., and Noller, H.F. (2012). Crystal structure of release factor RF3 trapped in the GTP state on a rotated conformation of the ribosome. RNA N. Y. N *18*, 230–240.

Zhou, J., Lancaster, L., Donohue, J.P., and Noller, H.F. (2013). Crystal Structures of EF-G-Ribosome Complexes Trapped in Intermediate States of Translocation. Science *340*, 1236086.

Zhou, J., Lancaster, L., Donohue, J.P., and Noller, H.F. (2014). How the ribosome hands the A-site tRNA to the P site during EF-G-catalyzed translocation. Science *345*, 1188–1191.